UNIVERSITY OF CALIFORNIA SAN DIEGO

Electrophysiological characterization of neurons in primary auditory cortex of the awake mouse

A dissertation submitted in partial satisfaction of the requirements for the degree Doctor of Philosophy

in

Neurosciences

by

Samuel Asinof

Committee in charge:

Professor Jeffry Isaacson, Chair
Professor Brenda Bloodgood
Professor Edward Callaway
Professor Timothy Gentner
Professor Roberto Malinow

2020

The Dissertation of Samuel Asinof is approved, and it is acceptable in quality and form for publication on microfilm and electronically:

_____

_____

_____

_____

_____

Chair

University of California San Diego

2020

DEDICATION

I wouldn't have been able to complete this without an incredible amount of support from my family and my friends. Thank you Wayne, Becky, Tracie, Diane, Jeff, and all of the other scientific mentors I've learned so much from. Thank you to my committee for all of their help. Thank you to the rest of the Isaacson Lab, especially to everyone who I collaborated with directly: Hiroyuki, Nick, Pei, and BJ. Thank you to the rest of the doctoral and postdoctoral trainees in CNCB, especially Sage who was the one who convinced me to come out to San Diego in the first place. Thank you to all of my friends in the UCSD Neurosciences Graduate Program, especially my classmates. And thank you to the friends who I've lived with in my first few years as a San Diegan: Chris, Neeraj and especially my cats' "padrino," Javier.

Thank you to my parents, who have always loved and supported me. And a special thank you to my partner Caroline, who is the most fiercely loyal, caring, and supportive person I know.

TABLE OF CONTENTS

LIST OF FIGURES

ACKNOWLEDGEMENTS

Chapter 1, in part, contains material published in *Neuron*: Kato, Hiroyuki; Asinof, Samuel; Isaacson, Jeffry, 2017. The dissertation author was a coauthor on this paper.

Chapter 2, in part, contains material published in the *Proceedings of the National Academy of Sciences*. Lin, Pei-Ann; Asinof, Samuel; Edwards, Nicholas; Isaacson, Jeffry, 2019. The dissertation author was a coauthor on this paper.

Chapter 3 contains material which is being prepared for submission for publication. The dissertation author will be a coauthor on this paper with Drs. Bernard Slater and Jeffry Isaacson.

VITA

2012 Bachelor of Arts, Oberlin College

2012-2015 Research Assistant, The Jackson Laboratory

2020 Doctor of Philosophy, University of California San Diego

PUBLICATIONS

Lin PA, *Asinof SK*, Edwards NJ, Isaacson JS. Arousal regulates frequency tuning in primary auditory cortex. *PNAS*, 2019.

Kato HK, *Asinof SK*, Isaacson JS, Network-level control of frequency tuning in auditory cortex. *Neuron*, 2017.

Asinof SK, Mahaffey CL, Beyer BJ, Letts VA, Frankel WN, Boumil RM. Dynamin 1 isoform roles in a mouse model of severe childhood epileptic encephalopathy. *Neurobiology of Disease*, 2016.

Asinof SK, Sukoff Rizzo SJ, Buckley AR, Beyer BJ, Letts VA, Frankel WN, Boumil RM. Independent Neuronal Origin of Seizures and Behavioral Comorbidities in an Animal Model of a Severe Childhood Genetic Epileptic Encephalopathy. *PLoS Genetics*, 2015.

Leung W., et al. Drosophila Muller F elements maintain a distinct set of genomic properties over 40 million years of evolution. *G3: Genes, Genomes, Genetics*, 2015.

Asinof SK and Paine TA. The 5-Choice Serial Reaction Time Task: A Task of Attention and Impulse Control for Rodents. *Journal of Visualized Experiments*, 2014.

Asinof SK and Paine TA. Inhibition of GABA synthesis in the prefrontal cortex increases locomotor activity but does not affect attention in the 5- choice serial reaction time task. *Neuropharmacology*, 2013.

Paine TA, *Asinof SK,* Diehl GW, Frackman A, Leffler J. Medial prefrontal cortex lesions impair decision-making on a rodent gambling task: Reversal by D1 receptor antagonist administration. *Behavioral Brain Research*, 2013.

ABSTRACT OF THE DISSERTATION

Electrophysiological characterization of neurons
in primary auditory cortex of the awake mouse

by

Samuel Asinof

Doctor of Philosophy in Neurosciences

University of California San Diego, 2020

Professor Jeffry Isaacson, Chair

The cerebral cortex is a laminar neural structure which serves as a critical substrate for higher cognitive abilities in humans and other mammals. Here, I use single-neuron recordings to investigate primary auditory cortex, the first cortical area to process aural information, in the brains of awake mice. Neurons in primary auditory cortex are sensitive to sounds of certain frequencies and intensities. I explore the synaptic bases for those preferences and demonstrate that they can be modulated on a moment-by-moment basis by changes in brain state.

INTRODUCTION

For my dissertation work in the Isaacson Lab, I used single-neuron recordings in the awake mouse in order to interpret the structure and functional properties of primary auditory cortex (A1). Normal A1 function is crucial to proper audition; it is therefore important to understand its broad contributions to the auditory system. A1 may also serve as a gateway to interpreting the function of other cortical sensory processing areas that employ similar components, have related hodology, and perform analogous computations using information from other sensory modalities.

In this preface, I will discuss the manner in which neurons in A1 integrate tuned excitatory and inhibitory currents to compute coherent representations of sound stimuli. I will also describe the functional architecture of the neocortex. Finally, I will review literature showing that cortical computations are labile, and can be modulated alongside changes in brain state.

Integration of Excitatory and Inhibitory Inputs

Neurons are specialized to integrate rapid electrical signals. Because they maintain large differences in the concentrations of charged ions (as well as other sources of negative charge) across their lipid bilayers, these charged particles are subject to steep electrochemical gradients driving their flux across the membrane. Ion-permeable channels in the membrane flexibly gate the flow of ions such as calcium, potassium, sodium, and chloride. Signals from other neurons cause these channels to open, producing strong currents that change the neuron's membrane potential and will trigger action potentials or "spikes" if the neuron is sufficiently depolarized.

The two primary currents which influence a neuron's membrane potential in the cerebral cortex are chloride currents, via GABA-sensitive channels called $GABA_A$ receptors, and depolarizing cation currents, which flux through glutamate-binding channels known as AMPA receptors. These currents, referred to in this dissertation as synaptic inhibition and synaptic excitation, respectively, can be studied by pharmacologically blocking other conductances (such as K+ channels) and injecting current to "clamp" the cell at the reversal potential for the ions flowing through each kind of channel such that the driving force for those ions is negligible. Provided that the neuron is small enough, the amount of injected current required to keep the cell at the specified holding potential should be equivalent to the total amount of ionic current flowing across the membrane of the cell. For example, one could measure synaptic excitation by clamping the cell at the chloride reversal potential near -70 mV.

Sensory receptive fields and response tuning

Cortical principal neurons (also referred to as “pyramidal cells” because of their morphology) are the staples of the cortical microcircuit. They are excitatory cells that project to diverse targets within their cortical area and throughout the brain.

In all mammalian sensory cortical areas, pyramidal cells are tuned to respond selectively to particular features of the animal's sensory landscape. In many cases, these neurons are organized on a smooth axis corresponding to different representations of one or more of these features. In primary visual cortex (V1), for example, principal cells increase their activity in response to stimuli of a particular

orientation or size found in a defined segment of visual space; neurons responsible for responding to input from the same retinotopic area are clustered together.

A1, the first cortical area to process incoming auditory stimuli, is organized in a similar manner. Pyramidal cells in A1 are tuned to features of sounds including intensity, frequency, or duration and are organized in a tonotopic manner (from lowest to highest frequency on a caudo-rostral axis). Tonal receptive fields (TRFs) of principal neurons in A1 are often described based on their shapes in frequency-intensity space. For example, in a cell with a V-shaped TRF, a single frequency (the neuron's "characteristic frequency," or CF) would induce an increase in spiking at very low sound intensities. As the intensity of the stimulus increases, stimuli from frequencies flanking the CF would also induce sound responses. This TRF could then be described based on the bandwidth of responsive frequencies at any given intensity.

Response amplitudes and receptive fields in auditory cortex are not merely inherited from lower-order auditory processing centers; they are further shaped by intracortical excitation and inhibition. A1 neurons are tuned far more narrowly in frequency-intensity space than their thalamic afferents (Liu et al. 2007). Even in the thalamorecipient layer 4 (L4) of V1 and A1, corticothalamic synapses only represent a minority of each cortical pyramidal cells' total synaptic input. The vast majority of this input comes from recurrent excitatory connections and local interneurons (Lien and Scanziani 2013; Reinhold et al. 2015; Li et al. 2013a; Li et al. 2013b; Liu et al. 2007). This cortical shaping of sensory tuning is not a rote or invariant process; recent evidence has demonstrated that that stimulus-evoked synaptic currents are modulated on a moment-by-moment basis as an animal experiences changes in arousal level.

One mechanism by which the cortex shapes its sensory responses is stimulus-evoked inhibition (Isaacson and Scanziani 2011). Inhibition in the cerebral cortex is generated by interneurons, cells local to the cortex which have a diversity of morphologies, laminar locations, tuning properties, synaptic specificity, and electrophysiological properties. This diversity confers each group of interneurons with exquisite control over the synaptic integration and firing activity of pyramidal cells.

Several models have been proposed for how cortical inhibition might instruct the tuning of pyramidal cells. In many sensory systems, tuning is shaped by patterns of synaptic excitation and inhibition which are distinct from one another (Poo and Isaacson 2009; Liu et al. 2011; Adesnik et al. 2012). Nonpreferred stimuli would evoke more inhibition than excitation, hyperpolarizing the cell and sharpening its tuning curve. This motif, known broadly as lateral inhibition, was originally described in the eye of the horseshoe crab by Haldan Hartline (Hartline et al. 1956).

However, there is little evidence that frequency tuning in A1 is shaped by lateral inhibition. Voltage-clamp recordings of pure tone-evoked synaptic excitation and inhibition in anesthetized animals demonstrate that the two currents are largely tuned to the same frequencies (Wehr and Zador 2003). These experiments suggest an alternate model in which the primary role of cortical inhibition is to counteract co-tuned excitation, reducing its impact such that it would fail to evoke a large enough depolarization to induce action potential firing, save for at the cells' preferred frequencies where excitation is strongest. Since the stimuli which evoke spikes are merely at the tip of the "iceberg" of the stimuli which evoke synaptic excitation, buried under an “ocean” of

synaptic inhibition, this model is often referred to as the "iceberg effect" (Wehr and Zador 2003; Carandini and Ferster 2000).

Some evidence indicates that synaptic inhibition is tuned to a slightly larger range of stimuli than excitation in A1. First, studies which recorded synaptic currents from L2/3 cells in whole-cell voltage clamp configuration have claimed that inhibitory inputs have a larger bandwidth (~0.5 octaves larger with 60 dB pure tone stimuli, Li et al. 2014) than their excitatory counterparts (Wu et al. 2008; Li et al. 2014; but see Wehr and Zador 2003). Second, experiments in which two tones are presented in rapid succession have revealed a "suppressive surround:" the presentation of a tone just outside of the cells' receptive field will suppress subsequent responses to a more preferred stimulus (Li et al. 2014). A common explanation for this phenomenon is that these "lateral" frequencies engage more inhibition than excitation, and this net inhibition will suppress spiking in response to the second tone.

While approximately co-tuned excitation and inhibition might produce this suppressive surround so long as inhibition is tuned slightly more broadly, some studies in awake animals have demonstrated slow suppressive responses tuned ≥1 octave from the preferred frequency (Sadagopan and Wang 2010). These findings are difficult to reconcile with the published observations of inhibitory tuning and the timing of interneuron firing and suggest that other mechanisms might be at play. In Chapter 1 of this dissertation, I will describe one such mechanism, a form of lateral inhibition which relies on network-level mechanisms and is only present in awake mice.

Anatomy of the neocortex

The cerebral cortex is comprised of a number of nested, inter-related neural circuits which iterate across different cortical columns in different functional areas (Harris and Shepherd 2015). These circuits generally contain two coarsely-defined cell classes: excitatory principal cells and inhibitory local interneurons. One of the defining characteristics of the cortex is its high degree of recurrent connectivity within and between each of these groups (Harris and Mrsic-Flogel 2013). Principal cells are bidirectionally connected with one another at far higher rates than expected by chance and connectivity is especially high for excitatory cells which have common afferent inputs or similar feature tuning (Markram and Sakmann 1997; Song et al. 2005; Yoshimura et al. 2005; Ko et al. 2011; Cossell et al. 2015). In sensory cortices, this recurrent excitatory connectivity outweighs afferent excitatory input and serves a role in amplifying responses to highly specific features (Lien and Scanziani 2013; Li et al. 2013a, Li et al 2013b; Liu et al. 2007; Harris and Mrsic-Flogel 2013).

Excitatory cells also have strong synaptic inputs onto local inhibitory cells, which pool synaptic input from neighboring excitatory cells irrespective of sensory tuning (Bock et al. 2011; Hofer et al. 2011), though sensory mapping does instill some feature selectivity. These interneurons then inhibit the majority of pyramidal cells less than 200 microns away (Packer and Yuste 2011; Fino and Yuste 2011). This connection motif results in the rapid recruitment of local feedback inhibition whenever a large quantity of pyramidal cells fire. Afferent excitatory input also contacts inhibitory cells in tandem with co-tuned pyramidal cells, driving interneurons to fire first and providing strong feedforward inhibitory input (Cruikshank et al. 2007; Li et al. 2014; Li et al. 2015).

All sensory cortices have many common elements, including a laminar structure. In the evolutionarily novel neocortex (which includes A1, V1, and S1), anatomists have defined six distinct layers, each of which contains a mixture of principal cells and interneurons which can be further subdivided based on connectivity, gene expression, and electrophysiological properties. Within the cortex, these cells interact with each other both vertically (with nearby similarly-tuned neurons in other layers) and horizontally (with distal, dissimilarly-tuned neurons within the same layer).

In primary sensory cortices, information flows into layers 4 and 5 from lower-order thalamic projections, which contact both principal cells and interneurons and engage co-tuned feedforward inhibition from the latter onto the former (Cruikshank et al. 2007; Li et al. 2014). Thalamorecipient L4 cells project recurrently onto their co-tuned neighbors, amplifying the tuned excitatory input, as well as onto principal cells and interneurons in other layers (Lien and Scanziani 2013, Li et al. 2013a, Li et al. 2013b, Harris and Shepherd 2015).

In L2 and 3, inputs from L4 cells arrive and depolarize both principal cells and parvalbumin-positive (PV) interneurons, which provide another round of co-tuned feedforward inhibition, further sharpening tuning and spike timing (Li et al. 2014). L2 and 3 neurons integrate information from many other cortical areas, including horizontal input from other superficial pyramidal cells and descending input from higher-order sensory processing centers (Petreanu et al. 2007). They project recurrently and horizontally to other L2/3 cells, to other pyramidal cells in higher order cortices, to the contralateral A1, and to pyramidal cells in deeper layers which serve as the main output of the cortex.

Pyramidal cells in L5 and L6 project to distinct subsets of distal targets, including other cortical areas, the striatum, the colliculi, and the thalamus (Han et al., 2018; Kim et al. 2016; Petrof et al. 2011; Games and Winer 1988; Joshi et al. 2015; Slater et al. 2019). In L5, these cells are divided into telencephalically-projecting cells and subcortically-projecting cells (Joshi et al. 2015; Harris and Shepherd 2015). Thalamically-projecting L6 cells send modulatory excitatory feedback projections to modality-matched relay cells (Sherman 2017), but also synapse onto other cortical cells. These include local interneurons that exert strong control over activity throughout the cortical column (Sherman 2017; Olsen et al. 2012; Bortone et al. 2014; Guo et al. 2017).

The Inhibition-Stabilized Network

I have discussed the abundance of recurrent connections in the neocortex. Afferent excitatory inputs are dwarfed by recurrent synapses, and excitatory activity recruits both feedback and feedforward inhibition. What are the consequences of this unique architecture?

This has been examined using simplified models in which the activity of excitatory and inhibitory populations are represented as the proportion of active cells within each population at any given time point (Tsodyks et al. 1997). Simply by changing the magnitude of the recurrent excitatory input onto the inhibitory population, one can also change how the two populations respond to an external modulation (Tsodyks et al. 1997; Ozeki et al. 2009). In a model in which principal cells make strong synapses onto both other principal cells and their inhibitory neighbors, the activity of the excitatory and inhibitory populations become inextricably linked. Excitatory activity

quickly becomes unstable without inhibitory input that scales flexibly to the demands placed upon it by principal cells; thus, the parameters in which this occurs are described as “inhibition-stabilized networks” (ISNs).

These models predict, paradoxically, that any external drive onto interneurons would produce the opposing effect at steady state (Tsodyks et al. 1997). Why does this occur? If interneuron activity increases, the activity of the excitatory cells that they synapse onto would diminish. This, in turn, would diminish the recurrent excitation which provides depolarizing drive onto interneurons, causing the activity of the interneuron population to decrease. The opposite effect should occur as well: if interneuron activity is disrupted, excitatory activity would increase rapidly, driving the interneuron population to higher firing rates. In the last decade, these results have been validated using more sophisticated models which better represent the architecture of sensory neocortex, including variants that incorporate multiple interneuron subtypes or multiple distinctly-tuned excitatory and inhibitory populations (Litwin-Kumar et al. 2012; Ozeki et al. 2009).

Recently many of these predictions have been further validated using experiments in awake animals (Sanzeni et al. 2019; Li et al. 2019; Moore et al. 2018; Kato et al. 2017). Optogenetic actuators make it possible to effectively and efficiently manipulate the activity of large classes of neurons with high temporal precision, and excitatory and inhibitory activity can either be measured as the firing rate of principal neurons and interneurons or, using whole-cell voltage clamp recordings, as the total amount of excitatory and inhibitory input that cortical pyramidal cells receive. In Chapters 1 and 2, I will describe evidence which suggests that A1 behaves as an ISN.

ISN-like behavior isn't merely a curiosity which is unmasked by drastic non-physiological manipulations. Models of recurrently-connected excitatory and inhibitory populations suggest that ISN-like behavior could be crucial to cortical sensory processing and phenomena such as visual surround suppression (Ozeki et al. 2009; Adesnik 2017).

Interneuron subtypes

There are many different kinds of cortical interneurons, distinguished from one another by gene expression patterns, physiological characteristics, laminar distributions, and connectivity. The three largest groupings have been established based on all of these criteria but named strictly for the molecular markers unique to them: Parvalbumin-positive (PV) cells, somatostatin-positive (SOM) cells and 5HT3-positive (5HT) cells account for ~80-90% of all cortical interneurons (depending on which cortical region is being assayed) (Rudy et al. 2010; Xu et al. 2010).

PV cells consist of soma-targeting basket cells and axon initial segment-targeting chandelier cells. The former are the dominant form of synaptic inhibition in the cortex. Basket cells in V1 pool excitatory input from the majority of pyramidal cells nearby and, as a consequence, share their average tuning (Hofer et al. 2011). Because they synapse directly on the soma, they have powerful inhibitory control of activity in these same pyramidal cells. Basket PV cells also receive afferent excitatory input and provide co-tuned feedforward input onto pyramidal cells (Li et al. 2015). They are designed to be recruited rapidly and precisely; they have low input resistance and rapid action potentials with strong after-hyperpolarizations; these unique "fast spikes" can be

distinguished from “regular-spiking” neurons by their unique waveforms (Kawaguchi and Kubota 1997). In A1, PV cells have frequency tuning which is similar to or perhaps slightly broader than pyramidal cells (Moore et al. 2013; Li et al. 2015).

SOM cells are a more diverse population. While all cells in this group express the peptide somatostatin, many subgroupings of SOM cells have been delineated based on gene expression patterns, connectivity, morphology, and responses to changes in brain state (Naka et al. 2019; Reimer et al. 2014; Muñoz et al. 2017; He et al. 2016). In V1, SOM cells in superficial layers have very few vertical inputs from thalamorecipient cells, but pool excitatory input from a wide range of horizontal excitatory inputs, making them adept for integrating large swaths of tuned sensory information (Adesnik et al. 2012). Martinotti cells, a group of SOM cells labeled by GFP in the GIN mouse line, are one of the largest subpopulations of SOM cells, and the most prevalent in superficial layers of the cortex (Rudy et al. 2010). These neurons are primarily dendrite-targeting, meaning that they exert exquisite control over somatic integration of dendritic inputs (Silberberg and Markram 2007). Local excitatory inputs onto this group are facilitating, meaning that repetitive inputs are likely to drive feedback inhibition (Silberberg and Markram 2007). One study reports that, in A1, SOM cells have a long latency to fire in response to short pure tone stimuli, and these onset responses are actually tuned less broadly than PV cells and pyramidal cells (Li et al. 2015).

The 5HT group is the most multifarious of these interneuron supergroups. This population includes a variety of serotonin- and acetylcholine-sensitive interneurons (Rudy et al. 2010). As a result, many of these cells are highly sensitive to neuromodulators which fluctuate alongside changes in brain state. While many of these

neurons are found in layer 1, the most numerous subgrouping of 5HT cells is the vasoactive intestinal polypeptide (VIP)-positive cells, which are mostly found in L2/3 (Rudy et al. 2010). VIP neurons have been shown to selectively target interneurons, especially SOM cells, in A1, V1, S1, and motor cortex, opening “holes” in a blanket of dendritic inhibition (Karnani et al. 2016a; Karnani et al. 2016b; Pi et al. 2013; Lee et al. 2013; Pfeffer et al. 2013). In A1 VIP cells have highly intensity-tuned sound onset responses (Mesik et al. 2015).

Arousal-dependent fluctuations in sensory response magnitude

Recent evidence suggests that sensory responses in the cerebral cortex are not context-invariant. Moment-to-moment fluctuations in an animal's arousal level modulate both spontaneous and sensory-evoked activity.

How are these changes in arousal level quantified? One popular technique for measuring changes in brain state is to sort neural data into “quiescent” and “active” epochs using binarized metrics of exploratory behaviors, such as running or whisking. While mice are running, the gain of visually-evoked V1 responses increases and the gain of sound-evoked A1 responses decreases (Niell and Stryker 2010; Zhou et al. 2014; Schneider et al. 2014; Schneider et al. 2018). Spontaneous activity in specific inhibitory cell types in V1 and S1 can have either positive or negative relationships with these behavior-indexed changes in arousal (Reimer et al. 2014; Muñoz et al. 2017). At low levels of arousal, pyramidal cells in A1, V1, and S1 have synchronous 2-10 Hz membrane potential oscillations driving spontaneous spiking at the same frequency (Poulet and Petersen 2008). During exploration, the cells desynchronize and

spontaneous firing diminishes not due to an increase in mean membrane potential, but because the cell spends less total time close to spike threshold (Bennett et al. 2013). This decrease in spiking leads to an increase in signal-to-noise ratio throughout the cortex during exploration.

Arousal levels can also be indexed using more graded measures, such as pupil diameter (Hess and Polt 1964; Kahneman and Beatty 1966; McGinley et al. 2015b). Large pupil diameters indicate a high level of arousal, and tend to be associated with exploratory behaviors (though the two measures are not entirely overlapping). Low levels of arousal correspond to smaller pupil diameters. Recent evidence suggests that many of the arousal-dependent changes in spontaneous and evoked cortical activity can actually be predicted better using pupillometry measures than by exploratory behaviors. For example, Vinck et al. demonstrated that, in V1, locomotor activity and pupil dilation actually have opposing effects on the spontaneous firing rates of presumptive principal cells (Vinck et al. 2015). Schneider et al. have posited that movement-associated suppression of spiking activity in A1 is actually a corollary discharge signal originating in secondary motor cortex, suggesting that locomotion-induced changes in firing rates might have little to do with arousal changes per se (Schneider et al. 2014). McGinley and colleagues described a “inverted U” relationship between pupil diameter and various response metrics, including AP firing rate, EPSP magnitude, and response reliability, in deeper layers of auditory cortex (McGinley et al. 2015a). This latter finding suggests that relating response measurements to binarized metrics (including exploratory behavior) or assuming linear relationships between arousal and a given metric would likely mask a great deal of arousal-dependent

response variability. Finally, it should be pointed out that pupil diameter in animals such as mice varies more continuously than the initiation of exploratory behaviors; there are many epochs in which arousal is high (as indexed by pupil diameter) and the animal is not running or whisking (Vinck et al. 2015; Lin et al. 2019).

What mechanisms underlie these diverse arousal-dependent changes in spontaneous and evoked activity across different cortical areas? Large changes in pupil diameter are thought to reflect swings in neuromodulatory tone; indeed, “high arousal states” have been associated with increases in norepinephrine and acetylcholine release (Reimer et al. 2016, Polack et al. 2013). Arousal-dependent changes in V1 such as the reduction in Vm variance or the gain change in visual responses require cholinergic signaling (Fu et al. 2014; Polack et al. 2013). In S1, whisking bouts have been linked to the lamina-specific modulation of firing rate in interneurons; for some of these cell types, whisking modulation requires cholinergic neurotransmission (Muñoz et al., 2017; Gentet et al. 2012; Gentet et al. 2010). In A1, the activity of neurons in layer 1 (which consists largely of neuromodulator-sensitive interneurons) is necessary for locomotion-dependent scaling down of tone-evoked excitation and inhibition in L2/3 (Zhou et al. 2014).

What are the effects of changes in brain state on spontaneous and evoked activity in A1? McGinley et al. examined the influence of arousal, as indexed by pupil diameter, on auditory responses to complex tones (McGinley et al. 2015a). However, that study did not specifically target A1, did not evaluate the effects of arousal on responses to simpler pure-tone stimuli, only reported measurements in deeper-layer cells, and did not measure the impact of changes in arousal on frequency tuning. Zhou

et al. and Schneider et al. evaluated the impact of locomotion on synaptic responses in layers 2, 3, and 4, but did not measure pupil diameters, leaving room to debate whether the effects they observed reflected a response to arousal-dependent modulation or (as suggested by the work of Schneider and Mooney) a corollary discharge signal designed to cancel out self-generated noise. In chapter 2, I will describe work from our lab which relates changes in arousal (as indexed by changes in pupil diameter) to changes in the receptive fields of A1 pyramidal cells. I will then demonstrate the synaptic mechanisms underlying this moment-by-moment modulation of response tuning.

Cross-callosal intra-A1 projections

All primary sensory cortices are hemispherically mirrored structures; each part represents sensory information from the contralateral side. Each of these cortices sends and receives information to the other cortex through projections that travel via the corpus callosum; in the case of V1 and S1, these cortico-cortical projections provide information useful for midline fusion.

In both V1 and S1, the primary sensory cortex is only several synapses removed from the peripheral sensory organ; this callosal projection is one of the first occasions for the interchange of hemispherically-localized information. In contrast, in the auditory system, information from both cochlear nerves are comparatively processed in multiple subcortical nuclei prior to arriving in A1. Since the auditory cortex is not the initial stage where mice make these comparisons of lateralized information, it is unclear why each A1 sends a robust excitatory projection to its contrahemispherical counterpart. In

Chapter 3, I will describe preliminary findings which explore the functions of this projection using unilateral optogenetic inactivation of A1.

References

Adesnik H (2017). Synaptic Mechanisms of Feature Coding in the Visual Cortex of Awake Mice. Neuron; 95(5):1147-1159.

Adesnik H, Bruns W, Taniguchi H, Huang ZJ, Scanziani M (2012). A neural circuit for spatial summation in visual cortex. Nature; 490(7419):226-31.

Anderson JS, Carandini M, Ferster D (2000). Orientation tuning of input conductance, excitation, and inhibition in cat primary visual cortex. J Neurophysiol; 84(2):909-26.

Bennett C, Arroyo S, Hestrin S (2013). Subthreshold mechanisms underlying state-dependent modulation of visual responses. Neuron; 80(2):350-7.

Bock DD, Lee WC, Kerlin AM, Andermann ML, Hood G, Wetzel AW, Yurgenson S, Soucy ER, Kim HS, Reid RC (2011). Network anatomy and in vivo physiology of visual cortical neurons. Nature; 471(7337):177-82.

Bortone DS, Olsen SR, Scanziani M (2014). Translaminar inhibitory cells recruited by layer 6 corticothalamic neurons suppress visual cortex. Neuron; 82(2):474-85.

Cossell L, Iacaruso MF, Muir DR, Houlton R, Sader EN, Ko H, Hofer SB, Mrsic-Flogel TD (2015). Functional organization of excitatory synaptic strength in primary visual cortex. Nature; 518(7539):399-403.

Cruikshank SJ, Lewis TJ, Connors BW (2007). Synaptic basis for intense thalamocortical activation of feedforward inhibitory cells in neocortex. Nat Neurosci.;10(4):462-8.

Fino E, Yuste R (2011). Dense inhibitory connectivity in neocortex. Neuron; 69(6):1188-203.

Fu Y, Tucciarone JM, Espinosa JS, Sheng N, Darcy DP, Nicoll RA, Huang ZJ, Stryker MP (2014). A cortical circuit for gain control by behavioral state. Cell;156(6):1139-1152.

Games KD, Winer JA (1988). Layer V in rat auditory cortex: projections to the inferior colliculus and contralateral cortex. Hear Res.; 34(1):1-25.

Gentet LJ, Avermann M, Matyas F, Staiger JF, Petersen CC (2010). Membrane potential dynamics of GABAergic neurons in the barrel cortex of behaving mice.Neuron; 65(3):422-35.

Gentet LJ, Kremer Y, Taniguchi H, Huang ZJ, Staiger JF, Petersen CC (2012). Unique functional properties of somatostatin-expressing GABAergic neurons in mouse barrel cortex. Nat Neurosci.;15(4):607-12.

Guo W, Clause AR, Barth-Maron A, Polley DB. A Corticothalamic Circuit for Dynamic Switching between Feature Detection and Discrimination (2017). Neuron; 95(1):180-194.

Han Y, Kebschull JM, Campbell RAA, Cowan D, Imhof F, Zador AM, Mrsic-Flogel TD. The logic of single-cell projections from visual cortex. Nature; 556(7699):51-56.

Harris KD, Mrsic-Flogel TD (2013). Cortical connectivity and sensory coding. Nature. 2013 Nov 7;503(7474):51-8.

Harris KD, Shepherd GM (2015). The neocortical circuit: themes and variations. Nat Neurosci.;18(2):170-81.

Hartline HK, Wagner HG, Ratliff F (1956). Inhibition in the eye of Limulus. J. Gen. Physiol.;39(5):651-73.

He M, Tucciarone J, Lee S, Nigro MJ, Kim Y, Levine JM, Kelly SM, Krugikov I, Wu P, Chen Y, Gong L, Hou Y, Osten P, Rudy B, Huang ZJ (2016). Strategies and Tools for Combinatorial Targeting of GABAergic Neurons in Mouse Cerebral Cortex. Neuron; 91(6):1228-1243.

Hess EH, Polt JM (1964). Pupil Size in Relation to Mental Activity during Simple Problem-Solving. Science;143(3611):1190-2.

Hofer SB, Ko H, Pichler B, Vogelstein J, Ros H, Zeng H, Lein E, Lesica NA, Mrsic-Flogel TD (2011). Differential connectivity and response dynamics of excitatory and inhibitory neurons in visual cortex. Nat Neurosci.; 14(8):1045-52.

Joshi A, Middleton JW, Anderson CT, Borges K, Suter BA, Shepherd GM, Tzounopoulos T (2015).Cell-specific activity-dependent fractionation of layer 2/3→5B excitatory signaling in mouse auditory cortex.J Neurosci.;35(7):3112-23.

Kahneman D, Beatty J (1966). Pupil diameter and load on memory. Science;154(3756):1583-5.

Karnani MM, Jackson J, Ayzenshtat I, Tucciarone J, Manoocheri K, Snider WG, Yuste R (2016). Cooperative Subnetworks of Molecularly Similar Interneurons in Mouse Neocortex. Neuron; 90(1):86-100.

Karnani MM, Jackson J, Ayzenshtat I, Hamzehei Sichani A, Manoocheri K, Kim S, Yuste R (2016). Opening Holes in the Blanket of Inhibition: Localized Lateral Disinhibition by VIP Interneurons. J Neurosci.;36(12):3471-80.

Kato HK, Asinof SK, Isaacson JS (2017). Network-Level Control of Frequency Tuning in Auditory Cortex. Neuron;95(2):412-423.

Kawaguchi Y, Kubota Y (1997). GABAergic cell subtypes and their synaptic connections in rat frontal cortex. Cereb Cortex;7(6):476-86.

Kim EJ, Juavinett AL, Kyubwa EM, Jacobs MW, Callaway EM (2015). Three Types of Cortical Layer 5 Neurons That Differ in Brain-wide Connectivity and Function. Neuron; 88(6):1253-1267.

Isaacson JS and Scanziani M (2011). How inhibition shapes cortical activity. Neuron;72(2):231-43.

Lee S, Kruglikov I, Huang ZJ, Fishell G, Rudy B (2013). A disinhibitory circuit mediates motor integration in the somatosensory cortex. Nat Neurosci;16(11):1662-70.

Li L-Y, Li YT, Zhou M, Tao HW, Zhang LI (2013). Intracortical multiplication of thalamocortical signals in mouse auditory cortex. Nat Neurosci;16(9):1179-81.

Li L-Y, Ji XY, Liang F, Li YT, Xiao Z, Tao HW, Zhang LI (2014). A feedforward inhibitory circuit mediates lateral refinement of sensory representation in upper layer 2/3 of mouse primary auditory cortex. J Neurosci.;34(41):13670-83.

Li L-Y, Xiong WR, Ibrahim LA, Yuan W, Tao HW, Zhang LI (2015). Differential Receptive Field Properties of parvalbumin and somatostatin inhibitory neurons in mouse auditory cortex. Cerebral Cortex 25:1782-1791.

Li N, Chen S, Guo ZV, Chen H, Huo Y, Inagaki HK, Chen G, Davis C, Hansel D, Guo C, Svoboda K (2019). Spatiotemporal constraints on optogenetic inactivation in cortical circuits. Elife; 8.

Li YT, Ibrahim LA, Liu BH, Zhang LI, Tao HW (2013). Linear transformation of thalamocortical input by intracortical excitation. Nat Neurosci;16(9):1324-30.

Lien AD, Scanziani M (2013). Tuned thalamic excitation is amplified by visual cortical circuits. Nat Neurosci.;16(9):1315-23.

Lin PA, Asinof SK, Edwards NJ, Isaacson JS (2019). Arousal regulates frequency tuning in primary auditory cortex. Proc Natl Acad Sci U S A.;116(50):25304-25310

Litwin-Kumar A, Rosenbaum R, Doiron B (2016). Inhibitory stabilization and visual coding in cortical circuits with multiple interneuron subtypes. J Neurophysiol; 115(3):1399-409.

Liu BH, Wu GK, Arbuckle R, Tao HW, Zhang LI (2007). Defining cortical frequency tuning with recurrent excitatory circuitry. Nat Neurosci.;10(12):1594-600.

Liu BH, Li YT, Ma WP, Pan CJ, Zhang LI, Tao HW (2011). Broad inhibition sharpens orientation selectivity by expanding input dynamic range in mouse simple cells. Neuron; 71(3):542-54.

Markram H, Lübke J, Frotscher M, Roth A, Sakmann B (1997). Physiology and anatomy of synaptic connections between thick tufted pyramidal neurones in the developing rat neocortex. J Physiol.; 500:409-40.

McGinley MJ, David SV, McCormick DA (2015). Cortical Membrane Potential Signature of Optimal States for Sensory Signal Detection. Neuron; 87(1):179-92.

McGinley MJ, Vinck M, Reimer J, Batista-Brito R, Zagha E, Cadwell CR, Tolias AS, Cardin JA, McCormick DA (2015). Waking State: Rapid Variations Modulate Neural and Behavioral Responses. Neuron; 87(6):1143-1161.

Mesik L, Ma WP, Li LY, Ibrahim LA, Huang ZJ, Zhang LI, Tao HW (2015). Functional response properties of VIP-expressing inhibitory neurons in mouse visual and auditory cortex. Front. Neural Circuits; 9:22.

Moore AK and Wehr M. (2013). Parvalbumin-expressing inhibitory interneurons in auditory cortex are well-tuned for frequency. J. Neurosci. 33, 13713–13723.

Moore AK, Weible AP, Balmer TS, Trussell LO, Wehr M (2018). Rapid Rebalancing of Excitation and Inhibition by Cortical Circuitry. Neuron; 97(6):1341-1355.

Muñoz W, Tremblay R, Levenstein D, Rudy B (2017). Layer-specific modulation of neocortical dendritic inhibition during active wakefulness. Science; 355(6328):954-959.

Naka A, Veit J, Shababo B, Chance RK, Risso D, Stafford D, Snyder B, Egladyous A, Chu D, Sridharan S, Mossing DP, Paninski L, Ngai J, Adesnik H (2019). Complementary networks of cortical somatostatin interneurons enforce layer specific control. Elife; 18(8).

Niell CM, Stryker MP (2010). Modulation of visual responses by behavioral state in mouse visual cortex. Neuron; 65(4):472-9.

Nienborg H, Hasenstaub A, Nauhaus I, Taniguchi H, Huang ZJ, Callaway EM (2013). Contrast dependence and differential contributions from somatostatin- and parvalbumin-expressing neurons to spatial integration in mouse V1. J Neurosci; 33(27):11145-54.

Olsen SR, Bortone DS, Adesnik H, Scanziani M (2012). Gain control by layer six in cortical circuits of vision. Nature;483(7387):47-52.

Ozeki H, Finn IM, Schaffer ES, Miller KD, Ferster D (2009). Inhibitory stabilization of the cortical network underlies visual surround suppression. Neuron; 62(4):578-92.

Packer AM, Yuste R (2011). Dense, unspecific connectivity of neocortical parvalbumin-positive interneurons: a canonical microcircuit for inhibition? J Neurosci.; 31(37):13260-71.

Petreanu L, Mao T, Sternson SM, Svoboda K (2009). The subcellular organization of neocortical excitatory connections. Nature; 457(7233):1142-5.

Pfeffer CK, Xue M, He M, Huang ZJ, Scanziani M (2013). Inhibition of inhibition in visual cortex: the logic of connections between molecularly distinct interneurons. Nat Neurosci.; 16(8):1068-76.

Pi HJ, Hangya B, Kvitsiani D, Sanders JI, Huang ZJ, Kepecs A (2013). Cortical interneurons that specialize in disinhibitory control. Nature; 503(7477):521-4.

Polack PO, Friedman J, Golshani P (2013). Cellular mechanisms of brain state-dependent gain modulation in visual cortex. Nat Neurosci.; 16(9):1331-9.

Poo C, Isaacson JS (2009). Odor representations in olfactory cortex: "sparse" coding, global inhibition, and oscillations. Neuron; 62(6):850-61.

Poulet JF, Petersen CC (2008). Internal brain state regulates membrane potential synchrony in barrel cortex of behaving mice. Nature; 454(7206):881-5.

Reimer J, Froudarakis E, Cadwell CR, Yatsenko D, Denfield GH, Tolias AS (2014). Pupil fluctuations track fast switching of cortical states during quiet wakefulness. Neuron; 84(2):355-62.

Reimer J, McGinley MJ, Liu Y, Rodenkirch C, Wang Q, McCormick DA, Tolias AS (2016). Pupil fluctuations track rapid changes in adrenergic and cholinergic activity in cortex. Nat Commun.; 7:13289

Reinhold K, Lien AD, Scanziani M (2015). Distinct recurrent versus afferent dynamics in cortical visual processing. Nat Neurosci.; 18(12):1789-97.

Rudy B, Fishell G, Lee S, Hjerling-Leffler (2010). Three groups of interneurons account for nearly 100% of neocortical GABAergic neurons. Developmental Neurobiology; 71(1):45-61.

Sadagopan S, Wang X (2010). Contribution of inhibition to stimulus selectivity in primary auditory cortex of awake primates. J Neurosci.; 30(21):7314-25.

Sanzeni A, Akitake B, Goldbach HC, Leedy CE, Brunel N, Histed MH. Inhibition stabilization is a widespread property of cortical networks. bioRxiv preprint published online Jan 3, 2020.

Schneider DM, Nelson A, Mooney R (2014). A synaptic and circuit basis for corollary discharge in the auditory cortex. Nature; 513(7517):189-94.

Schneider DM, Sundararajan J, Mooney R (2018). A cortical filter that learns to suppress the acoustic consequences of movement. Nature; 561(7723):391-395.

Sherman, S.M. (2017) Functioning of circuits connecting thalamus and cortex. Comprehensive Physiology, 7: 713-739.

Silberberg G, Markram H (2007). Disynaptic inhibition between neocortical pyramidal cells mediated by Martinotti cells. Neuron. 2007; 53(5):735-46.

Song S, Sjöström PJ, Reigl M, Nelson S, Chklovskii DB (2005). Highly nonrandom features of synaptic connectivity in local cortical circuits. PLoS Biol.;3(3):e68.

Tsodyks MV, Skaggs WE, Sejnowski TJ, McNaughton BL (1997). Paradoxical effects of external modulation of inhibitory interneurons. J Neurosci.;17(11):4382-8.

Vinck M, Batista-Brito R, Knoblich U, Cardin JA (2015). Arousal and locomotion make distinct contributions to cortical activity patterns and visual encoding. Neuron; 86(3):740-54.

Wehr M, Zador AM (2003). Balanced inhibition underlies tuning and sharpens spike timing in auditory cortex. Nature; 426(6965):442-6.

Wu GK, Arbuckle R, Liu BH, Tao HW, Zhang LI (2008). Lateral sharpening of cortical frequency tuning by approximately balanced inhibition. Neuron; 58(1):132-43.

Xu X, Roby KD, Callaway EM (2010). Immunochemical characterization of inhibitory mouse cortical neurons: three chemically distinct classes of inhibitory cells. J Comp Neurol.; 518(3):389-404.

Yoshimura Y, Dantzker JL, Callaway EM (2005). Excitatory cortical neurons form fine-scale functional networks. Nature; 433(7028):868-73.

Zhou M, Liang F, Xiong XR, Li L, Li H, Xiao Z, Tao HW, Zhang LI (2014). Scaling down of balanced excitation and inhibition by active behavioral states in auditory cortex. Nat Neurosci.; 17(6):841-50.

CHAPTER 1

Abstract

Lateral inhibition is a fundamental circuit operation that sharpens the tuning properties of cortical neurons. This operation is classically attributed to an increase in GABAergic synaptic input triggered by non-preferred stimuli. Here we use *in vivo* whole-cell recording and two-photon Ca2+ imaging in awake mice to show that lateral inhibition shapes frequency tuning in primary auditory cortex via an unconventional mechanism: non-preferred tones suppress both excitatory and inhibitory synaptic inputs onto layer 2/3 cells (“network suppression”). Moreover, optogenetic inactivation of inhibitory interneurons elicits a paradoxical increase in inhibitory synaptic input. These results indicate that GABAergic interneurons regulate cortical activity indirectly via the suppression of recurrent excitation. Furthermore, the network suppression underlying lateral inhibition was blocked by inactivation of somatostatin-expressing interneurons (SOM cells), but not parvalbumin-expressing interneurons (PV cells). Together, these findings reveal that SOM cells govern lateral inhibition and control cortical frequency tuning through the regulation of reverberating recurrent circuits.

Introduction

In sensory cortical areas, neurons sharply tuned to particular features of sensory stimuli underlie precise representations of the external world. For example, pyramidal cells in visual cortex respond selectively to visual stimuli with a certain orientation or size, those in rodent somatosensory cortex prefer particular directions of whisker deflection, and neurons in auditory cortex fire selectively to certain sound frequencies.

Revealing the factors governing cortical tuning properties is fundamental for understanding how sensory information is encoded in the brain.

The excitatory synaptic input driving tuned pyramidal cell activity comes from two main sources: afferent thalamic inputs and recurrent synapses between pyramidal cells themselves that amplify thalamic input (Li et al. 2013; Lien and Scanziani 2013). While excitation broadly defines the tuning of pyramidal cell spike output, stimulus selectivity can be further refined by inhibitory synaptic input (Isaacson and Scanziani 2011; Priebe and Ferster 2008). Cortical inhibition is mediated by a variety of local GABAergic interneurons that are highly interconnected with pyramidal cells as well as each other (Pfeffer et al. 2013; Tremblay et al. 2016). However, the precise synaptic mechanisms by which interconnected excitatory and inhibitory circuits generate pyramidal cell tuning properties are not established.

Lateral inhibition, first described in photoreceptors (Hartline et al. 1956), is a basic circuit operation that can sharpen cortical tuning properties (Isaacson and Scanziani 2011; Priebe and Ferster 2008). In this operation, pyramidal cells firing in response to stimuli in their receptive fields recruit local interneurons, which in turn suppress firing of other neurons with different receptive fields. In a classical model, lateral inhibition narrows tuning of individual neurons when non-preferred stimuli recruit inhibitory synaptic input more strongly than excitation. In other words, lateral inhibition occurs when synaptic inhibition is more broadly tuned than excitation. Indeed, differences in the tuning broadness of excitation and inhibition have been proposed to enforce odor selectivity in olfactory cortex (Poo and Isaacson 2009) as well as

selectivity for the size (Adesnik et al. 2012) and orientation (Liu et al. 2011; but see Tan et al. 2011) of visual stimuli in visual cortex.

Interestingly, in primary auditory cortex the extent to which lateral inhibition contributes to frequency tuning as well as the synaptic mechanisms underlying suppressive effects of non-preferred stimuli are a matter of debate. For example, studies in primates, cats, and rodents using two-tone protocols have found that firing to preferred frequencies can be suppressed when preceded by tones that are octaves different (Calford and Semple 1995; Li et al. 2014; Phillips and Cynader 1985; Sadagopan and Wang 2010; Sutter et al. 1999). Although two-tone suppression is typically attributed to GABAergic inhibition produced by the first sound, synaptic depression of excitatory input has also been shown to contribute to suppressed activity in this paradigm (Wehr and Zador 2005). More typical of classic lateral inhibition, single tones at non-preferred frequencies have also been found to cause suppression of spontaneous neuronal firing in awake primates (O'Connell et al. 2011; Sadagopan and Wang 2010). However, these reports of response suppression are difficult to reconcile with intracellular recordings of sound-evoked synaptic responses in rodent auditory cortex. For instance, studies have found completely balanced excitation and inhibition in layer 2/3 (L2/3) and layer 4 (Wehr and Zador 2003; Zhang et al. 2003; Zhou et al. 2014) or inhibition tuned only slightly broader than excitation (Li et al. 2014; Wu et al. 2008). In this "co-tuning" scenario, inhibition would contribute to frequency tuning by ensuring that only the strongest excitatory input depolarizes cells to spike threshold, a mechanism known as the "iceberg effect" (Carandini and Ferster 2000). Since this effect regulates

tuning only in a rather narrow range around the preferred frequency, the synaptic mechanisms underlying broad side-band suppression remain unknown.

We used a genetically-encoded fluorescent calcium sensor to assay the tuning properties of neurons in A1 L2/3 of awake head-fixed mice. In these experiments, we observe that frequencies higher than the preferred frequency induced a suppression of spontaneous spiking, irrespective of the cells' characteristic frequency or receptive field shape. We then elucidate a novel mechanism for this lateral inhibition: non-preferred sounds do not increase inhibitory inputs onto individual neurons, but rather suppress both excitatory and inhibitory inputs (network suppression).

In follow-up experiments we probe the importance of distinct interneuron classes for this suppression. Transient inactivation experiments demonstrate that somatostatin-positive interneurons are essential for the initiation of network suppression, and two photon microscopy-targeted juxtacellular recordings confirm that a subset of these cells are among the most broadly-tuned neurons in superficial A1. Finally, we developed a novel slice preparation which preserves the tonotopic axis of A1 in order to assay the spatial extent of inhibition from SOM and PV cells. Using *ex vivo* recordings from this preparation, we discovered that SOM neurons send monosynaptic inhibitory projections a great distance across cortical space. These results suggest that SOM cells integrate and transmit frequency information horizontally across A1 to trigger network-level lateral inhibition.

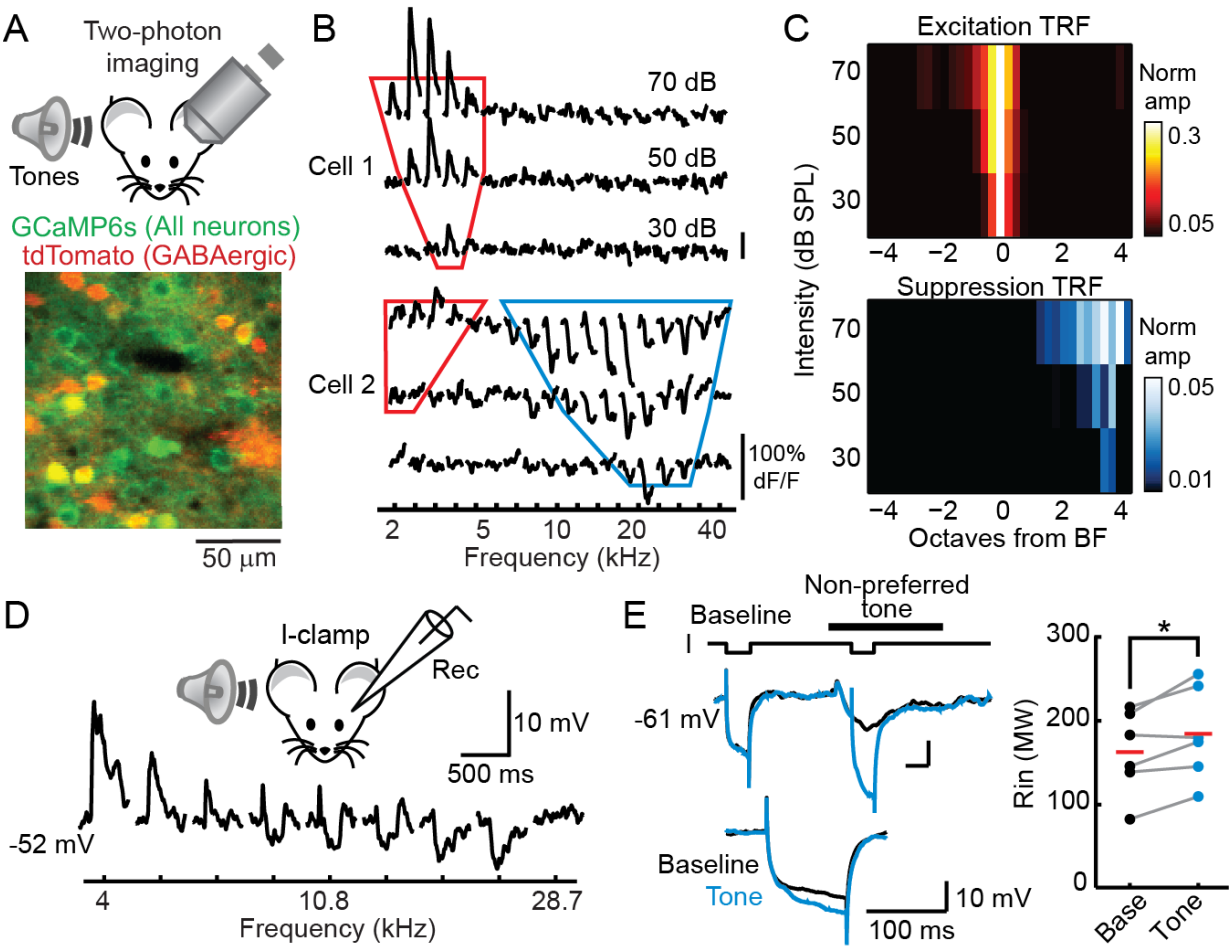

Figure 1.1 Lateral inhibition in auditory cortex of awake mice. A. Top, schematic of *in vivo* two-photon calcium imaging. Bottom, *in vivo* image of GcaMP6s-expressing (green) and tdTomato-expressing (red) cells in L2/3 of A1. **B.** Frequency tuning of two representative L2/3 pyramidal cells. Traces are average responses (from 5 trials) to tone pips of 17 frequencies (columns) at three intensities (rows). **C.** Lateral inhibition is prominent at high frequencies in the summary plot of excitatory and inhibitory TRFs averaged across all cells with excitatory responses (n=749 cells from 8 mice). Responses are centered on the best frequency for excitation and normalized to the maximum response of each neuron. **D.** Top, schematic of *in vivo* current clamp recordings. Bottom, membrane potential responses of a representative cell to tone pips (nine frequencies, all at 70 dB) show a steady shift from depolarization to hyperpolarization as frequency increases. **E.** Cell input resistance increases during inhibition at non-preferred frequencies. Top left, membrane response to current steps (I, -100 pA) in a representative cell before (Baseline) and during inhibition evoked by a non-preferred tone (indicated by the black bar). Superimposed traces are averages of interleaved trials in which the current step was applied (blue) or witheld during the tone (black). Bottom left, subtracted response to current injection (blue) overlaid on the baseline response (black), indicating increased membrane resistance. Right, summary of cell input resistance (Rin) change during inhibition elicited by non-preferred tones (n=6 cells from 4 mice).

Results

We first investigated lateral inhibition in A1 by testing the frequency tuning properties of a large population of L2/3 pyramidal cells using two-photon calcium imaging in awake head-fixed mice (Figure 1.1A-C). To isolate action potential-dependent responses of excitatory pyramidal cells, the Ca2+ indicator GCaMP6s was expressed in mice in which GABAergic inhibitory neurons were marked with tdTomato (Gad2-IRES-Cre-ROSALSL-tdTomato mice). Tonal receptive fields (TRFs) of individual L2/3 pyramidal cells were measured by presenting pure tones (1 s) across a range of frequencies (2–40 kHz) and intensities (30–70 dB). On average, 41.7% ± 8.1% of GCaMP6s-expressing pyramidal cells (n = 1,681 cells, 8 mice) increased their activity (measured as dF/F) in response to at least one frequency, and many of those cells (41.3%) displayed classical ‘‘V-shaped’’ TRFs (Figure 1.1B, top). A similar fraction of pyramidal cells (32.3% ± 7.2%) decreased their activity in response to at least one frequency, as previously reported in awake mice (Kato et al., 2015). Importantly, lateral inhibition was clearly present, since pyramidal cells could have both excitatory and suppressive responses to non-overlapping frequencies (Figure 1.1B, bottom). We determined average TRFs across all excited cells (n = 749) by centering tuning curves to their best frequencies (BF, frequency eliciting the strongest response regardless of intensity) for excitation. Interestingly, the population TRFs revealed prominent suppressive responses evoked by frequencies one to four octaves higher than the BF for excitation (Figure 1.1C). Though weaker in relative magnitude, suppressive responses were also apparent at frequencies one to four octaves lower than the excitatory BF. The wide separation between excitatory and suppressive TRFs we

observe cannot arise from approximately balanced synaptic excitation and inhibition. Rather, our results indicate that lateral inhibition biased toward frequencies higher than those driving excitation shapes frequency tuning in A1 of awake mice.

What mechanisms underlie lateral inhibition in A1 under our conditions? To address this question we used blind patch clamp recording to study sound-evoked responses of L2/3 cells in awake mice. In current clamp recordings (resting potential −62 ± 2 mV, n = 12), cells had regular action potential firing with spike widths typical of pyramidal cells (1.22 ± 0.07 ms, n = 8 cells). In addition, spikes recorded in cell-attached mode for 30/31 blind whole-cell recordings in this study had waveforms distinct from fast-spiking (FS) interneurons (data not shown). Given that pyramidal cells make up the bulk of non-FS cells in L2/3, we refer to the recorded neurons in this study as "pyramidal cells." Tones (100–200 ms duration) evoked membrane depolarization at particular (preferred) frequencies and this excitation became progressively briefer before switching to pure hyperpolarizing responses as frequencies shifted away from the preferred stimulus (Figure 1.1D). Intriguingly, we found that cell input resistance increased significantly (p = 0.03) during the hyperpolarization evoked by non-preferred frequencies (Figure 1.1E). This is puzzling since synaptic inhibition classically requires activation of a GABAergic synaptic conductance that lowers membrane resistance (Isaacson and Scanziani, 2011). Indeed, this finding indicates that an unconventional synaptic mechanism underlies lateral inhibition in auditory cortex.

Figure 1.2 Non-preferred frequencies evoke slow network suppression of spontaneous synaptic activity A. Top, schematic of *in vivo* voltage clamp recording. Bottom, a non-preferred tone suppresses both spontaneous EPSCs and IPSCs in a representative cell. Five consecutive trials are displayed in different colors. Black bar, tone. **B.** Frequency tuning of synaptic excitation (EPSC) and inhibition (IPSC) in one cell. Traces are average responses (six trials) for each frequency-intensity pair. Red lines outline region of synaptic TRF with fast, onset-locked responses ($EPSC_{ON}$ and $IPSC_{ON}$), blue lines indicate area of TRF with slow changes in current due to network suppression ($EPSC_{NS}$ and $IPSC_{NS}$). **C.** EPSC and IPSC from outlined areas in B averaged across frequency-intensity pairs with onset-locked responses (A,C, red) and network suppression (B, D, blue). Grey dotted lines mark the windows for measuring onset-locked responses ('ON') and network suppression ('NS'). **D.** TRFs for $EPSC_{ON}$, $IPSC_{ON}$, $EPSC_{NS}$, and $IPSC_{NS}$ amplitude averaged across cells (n=23 cells, 17 mice). Responses are centered at BF of $EPSC_{ON}$ for each cell. **E.** Summary of the frequency tuning of the four components, averaged from responses to 50-70 dB tones. Response amplitudes are normalized to their individual peak values. Bold line, mean; shading ±SEM.

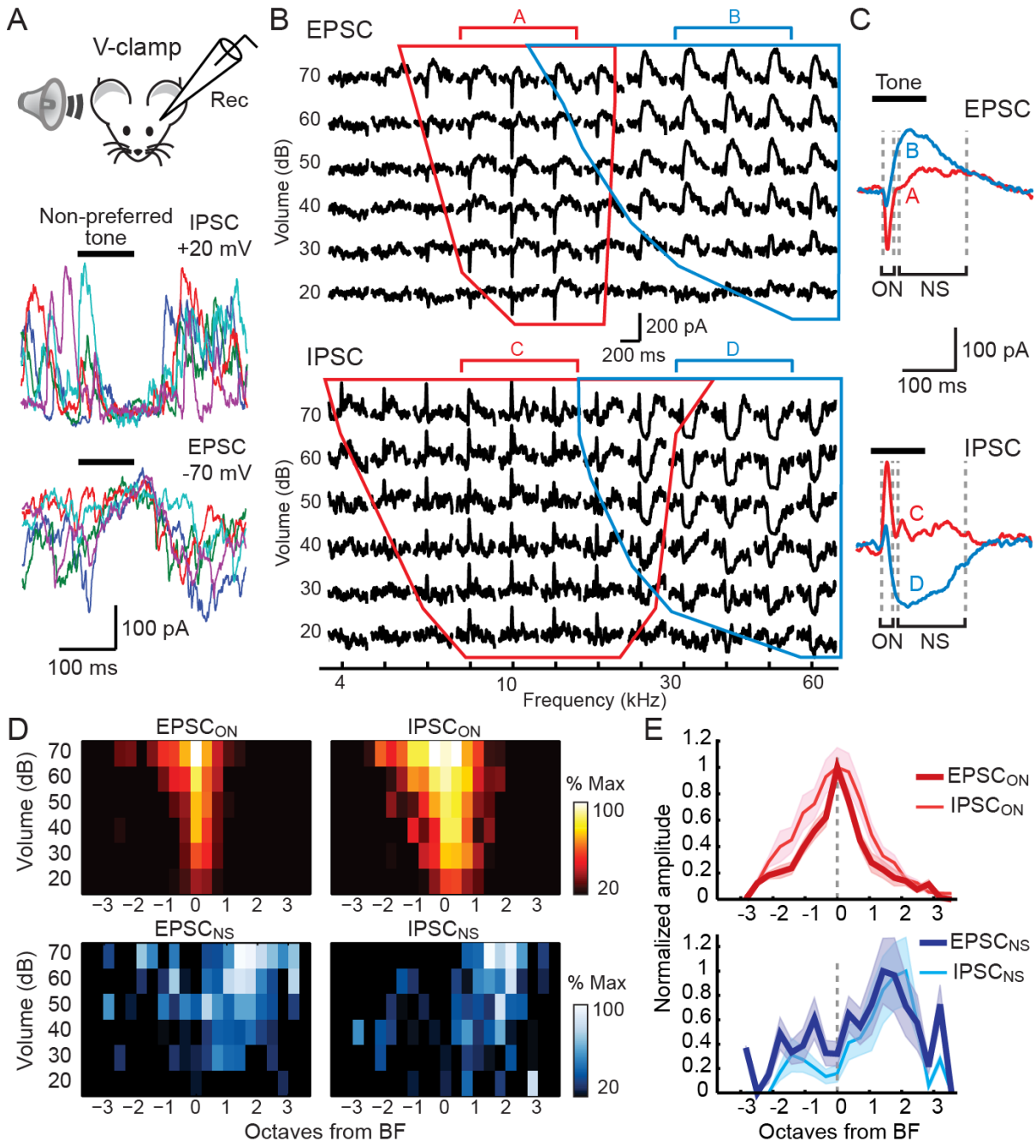
A
V-clamp
Rec
Non-preferred tone
IPSC +20 mV
EPSC -70 mV
100 pA
100 ms
B
EPSC
A
B
Volume (dB)
200 pA
200 ms
IPSC
C
D
4
10
30
60
Frequency (kHz)
C
Tone
EPSC
ON
NS
100 pA
100 ms
IPSC
D
EPSCON
IPSCON
% Max
EPSCNS
IPSCNS
Octaves from BF
E
Normalized amplitude

We next used voltage-clamp recording to directly determine the postsynaptic currents that shape frequency tuning in A1. Excitatory postsynaptic currents (EPSCs) and inhibitory postsynaptic currents (IPSCs) were recorded near the reversal potentials for synaptic inhibition and excitation, respectively. Recordings in awake mice revealed sustained, high-frequency barrages of spontaneous EPSCs and IPSCs, indicating that cortical circuits were highly active even in the absence of delivered tones (Figure 1.2A). In contrast, we observed relatively low basal activity interrupted by irregular bursts of synaptic activity if the pipette internal solution included the voltage-gated sodium channel blocker QX-314 (5 mM) or if the cortex was damaged due to poor surgical exposure of the brain surface or excessive pipette penetrations. Remarkably, under our conditions of high cortical activity, presentation of non-preferred tones suppressed both spontaneous EPSCs and IPSCs (Figure 1.2A). This suppression of ongoing network activity ("network suppression") by non-preferred stimuli is completely different from the selective increase in IPSCs expected for classical lateral inhibition. Rather, these results indicate that the membrane hyperpolarization underlying lateral inhibition in A1 is due to the withdrawal of excitatory synaptic input, which is likely driven indirectly by local interneurons.

Our results raise the possibility that preferred and non-preferred stimuli trigger distinct inhibitory circuit operations. We tested this by measuring the frequency tuning of excitatory and inhibitory synaptic currents. Indeed, averaged responses (five to ten trials per frequency-intensity pair, 100 ms tone duration) from individual neurons displayed two types of synaptic activity that differed in their kinetics and tuning (Figure 1.2B-C). We observed transient, sound onset-locked EPSCs ($EPSC_{ON}$) and IPSCs ($IPSC_{ON}$) with

overlapping TRFs similar to previous reports in A1 (Li et al. 2014; Wehr and Zador, 2003; Wu et al. 2008; Zhang et al. 2003; Zhou et al. 2014). However, higher-frequency tones evoked a slow suppression of spontaneous EPSCs and IPSCs, which on average traces appear as slow currents opposite in polarity to onset-locked responses. Interestingly, while sustained suppression of synaptic activity was also observed with longer duration (1 s) tones, brief 15 ms tone "pips" evoked predominantly transient, sound onset-locked responses (data not shown). The slow components do not reflect voltage-clamp errors that reverse $IPSC_{ON}$ and $EPSC_{ON}$ since the kinetics and tuning of the fast and slow currents are distinct, nor do they reflect shunting inhibition, since non-preferred stimuli increase input resistance (Figure 1.1E). Rather, we consider these slow components, $EPSC_{NS}$ and $IPSC_{NS}$, to be due to the withdrawal of spontaneous synaptic activity during network suppression.

The TRFs of $EPSC_{ON}$ and $IPSC_{ON}$ largely overlap (Figure 1.2D-E), with $IPSC_{ON}$ more broadly tuned, consistent with previous findings in L2/3 (Li et al. 2014; but see Zhou et al. 2014 and Wehr and Zador 2003). However, the difference in tuning broadness (half-maximal bandwidth) is only 0.4 octaves and cannot account for the suppression of spike output one to four octaves from best frequency (Figure 1.1C). Thus, a conventional model for lateral inhibition solely based on broadly tuned inhibitory synaptic input does not apply to frequency tuning in A1 of awake mice. In contrast, the tuning of $EPSC_{NS}$ and $IPSC_{NS}$ is shifted far from $EPSC_{ON}$ best frequency (distance to peak $EPSC_{NS}$ and $IPSC_{NS}$: 1.4 ± 0.2 octaves and 1.6 ± 0.1 octaves, respectively) and covers the range of frequencies for lateral inhibition observed with GCaMP6s imaging. Taken together, these results suggest that the frequency tuning properties of L2/3 cells

are regulated by inhibitory neurons acting via both direct synaptic inputs (preferred tones) and indirect decreases in network activity (non-preferred tones).

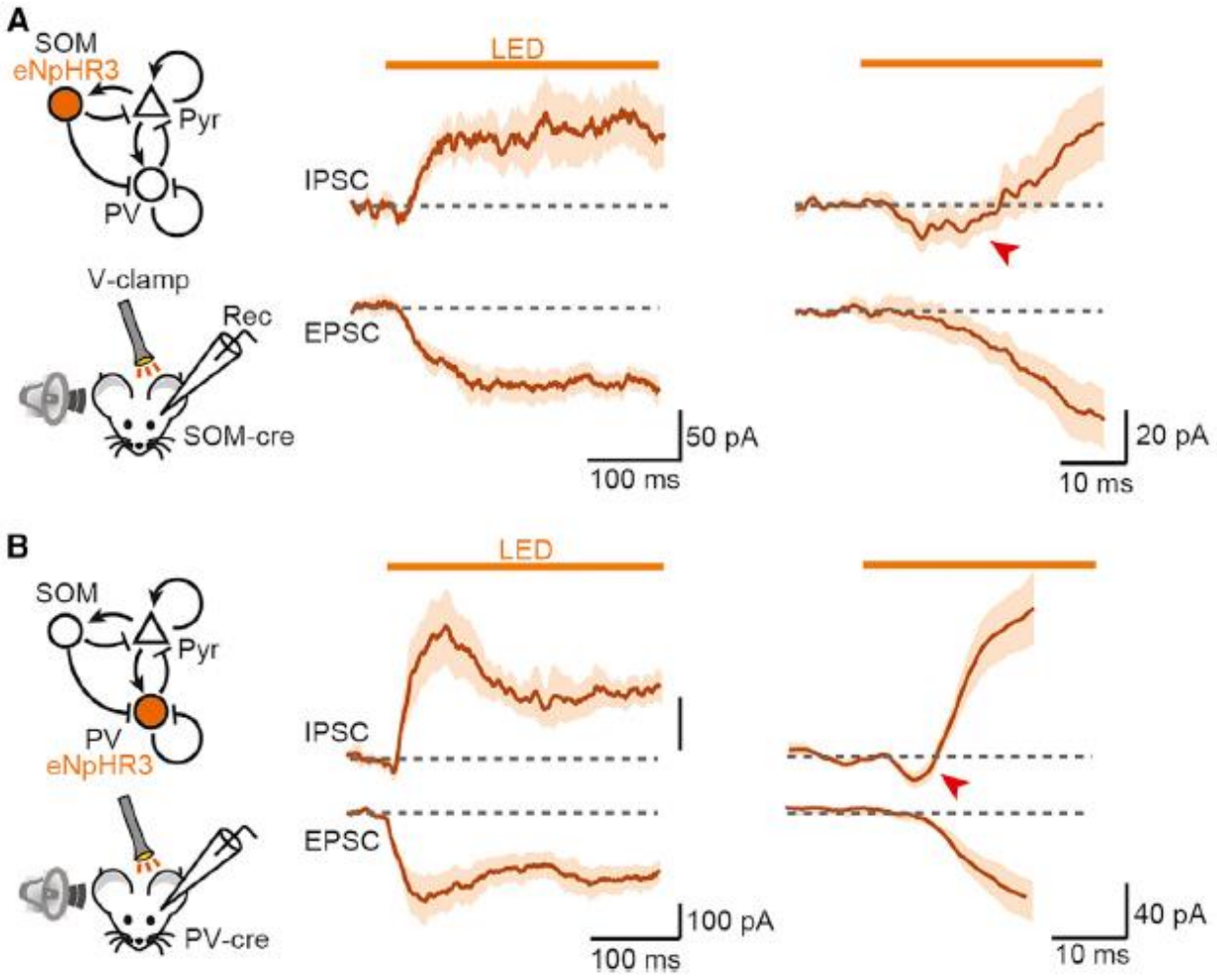

Figure 1.3 Suppression of interneurons causes a paradoxical increase in pyramidal cell-inhibitory synaptic current. A. Left, schematic of optogenetic inactivation of SOM cells during *in vivo* voltage-clamp recording. Circuit based on Pfeffer at al., 2013. Middle, photoinactivation of SOM cells increases spontaneous EPSCs and IPSCs. Traces show average responses across experiments (n=12 cells from 8 mice). Dark trace, mean across cells; shading, ±s.e.m. Orange bars, LED. Right, expansion of the traces at LED onset reveals a transient reduction in inhibition (marked by a red arrowhead) which precedes the paradoxical increase in IPSC. **B.** PV cell inactivation experiments. EPSCs and IPSCs as shown in A (n=9 cells from 5 mice).

What cortical regime can produce lateral inhibition via a decrease in excitatory synaptic input? We considered the idea that the cortex might operate as an inhibition-stabilized network (ISN), a proposed model in which recurrent excitation is strong enough to destabilize the cortical network unless it is tightly regulated by recurrent inhibition (Litwin-Kumar et al. 2016, Ozeki et al. 2009, Rubin et al. 2015, Tsodyks et al. 1997). In ISNs, lateral input onto inhibitory interneurons transiently increases inhibition and suppresses excitatory neurons. However, since strong recurrent excitation tightly regulates interneuron firing, a new steady state is reached in which both excitatory and inhibitory neuron activities are reduced.

To directly determine whether A1 acts as an ISN, we tested a central hypothesis of this network model: suppression of inhibitory neurons should cause a transient reduction of inhibitory input onto individual pyramidal cells, followed by a paradoxical increase in synaptic inhibition (Litwin-Kumar et al. 2016; Ozeki et al. 2009; Tsodyks et al. 1997). The majority of cortical inhibition is mediated by SOM-, PV-, and vasoactive intestinal peptide (VIP)-expressing interneurons (Pfeffer et al. 2013; Rudy et al. 2011; Xu et al. 2010). As a population, cortical VIP cells only weakly inhibit pyramidal cells (Pfeffer et al. 2013). Thus, we focused attention on SOM and PV cells which provide the major sources of inhibition onto pyramidal cells. We recorded EPSCs and IPSCs in L2/3 and photo-inactivated SOM (Figure 1.3A) or PV cells (Figure 1.3B), using the hyperpolarizing opsin halorhodopsin (eNpHR3). We used weak LED intensities to modulate transmission without inducing aberrant discharges. Exactly as predicted for an ISN, photoinactivation of SOM or PV cells produced a transient reduction in tonic inhibitory currents followed by a sustained increase in IPSCs (Figures 1.3A and 1.3B;

IPSC amplitude, PV = 137 ± 33 pA, p = 0.002; SOM = 61 ± 23 pA, p = 0.02, 100–200 ms following LED onset). As expected, EPSCs showed a monotonic enhancement coinciding with the IPSC increase (EPSC amplitude, PV = −88 ± 19 pA, p = 0.001; SOM = −73 ± 18 pA, p < 0.001). These results strongly support the idea that auditory cortex operates as an ISN in awake animals and reveal the foundation for the reduced excitation during lateral inhibition.

Which class of interneurons is responsible for regulating cortical network activity during lateral inhibition? To address this question, we measured the tuning properties of different interneuron types in response to prolonged (1 s long) pure tone stimuli. NS lateral inhibition is a slow sound response which emerges with relatively long latency and can match the duration of a triggering stimulus. Therefore, we reasoned that NS lateral inhibition might rely upon activity in interneurons with longer-latency sound responses which were tuned broadly (or perhaps anti-tuned), and that responses which produce NS might persist for the entire duration of a longer stimulus. Finally, the interneurons which trigger NS are unlikely to be suppressed themselves.

Imaging of calcium activity using GCaMP6 revealed that PV and SOM cells had sound responses which were coherent to the global tonotopic axis as identified by macroscopic imaging (Figure 1.4A), suggesting that neither population was “anti-tuned.” PV cells, like pyramidal cells, were inhibited by lateral frequencies (Figure 1.4B). In contrast, SOM cells rarely had suppressive TRFs and their sound responses were more broadly tuned (Figure 1.4B).

Figure 1.4 SOM cells are broadly tuned and have sustained tone responses. A. Frequency tuning of pyramidal (pyr), SOM, and PV cells cohere to the macroscopic tonotopy of A1. Top left, image of intrinsic signal showing reference points used for normalizing distance along the A1 tonotopic axis across animals. Graphs map the characteristic frequency (CF) of the three cell populations determined from two-photon Ca^{2+} imaging, indicating that all of these populations have tuning which roughly conforms to the tonotopic axis. **B.** TRFs for imaged SOM and PV cells (centered on the BF for excitation and normalized to the maximum response for each neuron) show that SOM cell excitation is more broadly tuned while PV cells receive lateral inhibition. **C.** Left, schematic of *in vivo* targeted juxtacellular recordings. Right, an image from an experiment showing a pipette filled with Alexa-488 (green) contacting a tdTomato-positive PV cell. **D.** Spiking responses from an example PV cell. **D1.** tone responses to a range of pure tone stimuli which evoke an increase in spiking (outlined in red) and/or a strong suppression of spontaneous spiking (outlined in blue). Each trace is a trial-averaged mean spiking response binned in 25 ms intervals. Grey traces, frequencies which do not evoke a response. **D2.** Trial-by-trial average of all frequency responses outlined in red in D1, demonstrating a short-latency onset response and a partial suppression of spontaneous spiking (due to overlap between the onset response TRF and the cell's suppressive TRF at high intensities). **E.** Spiking responses from an example SOM cell, presented as in D. The cell has a broadly tuned tone response which is sustained for the duration of the stimulus presentation (see E2). **F.** Z-scored spiking averaged across cells during either the first 100 ms of the tone response (red line) or the last 900 ms (black line). Responses have been averaged across intensities (10-70 dB) and plotted based on absolute distance from the BF. Left, PV cells. Right, SOM cells. Shading is ± s.e.m. **G.** Tuning broadness, quantified as the percentage of frequency-intensity pairs evoking a significant response. Response significance within each time window for each frequency-intensity pair was determined using a bootstrapping procedure (see methods).

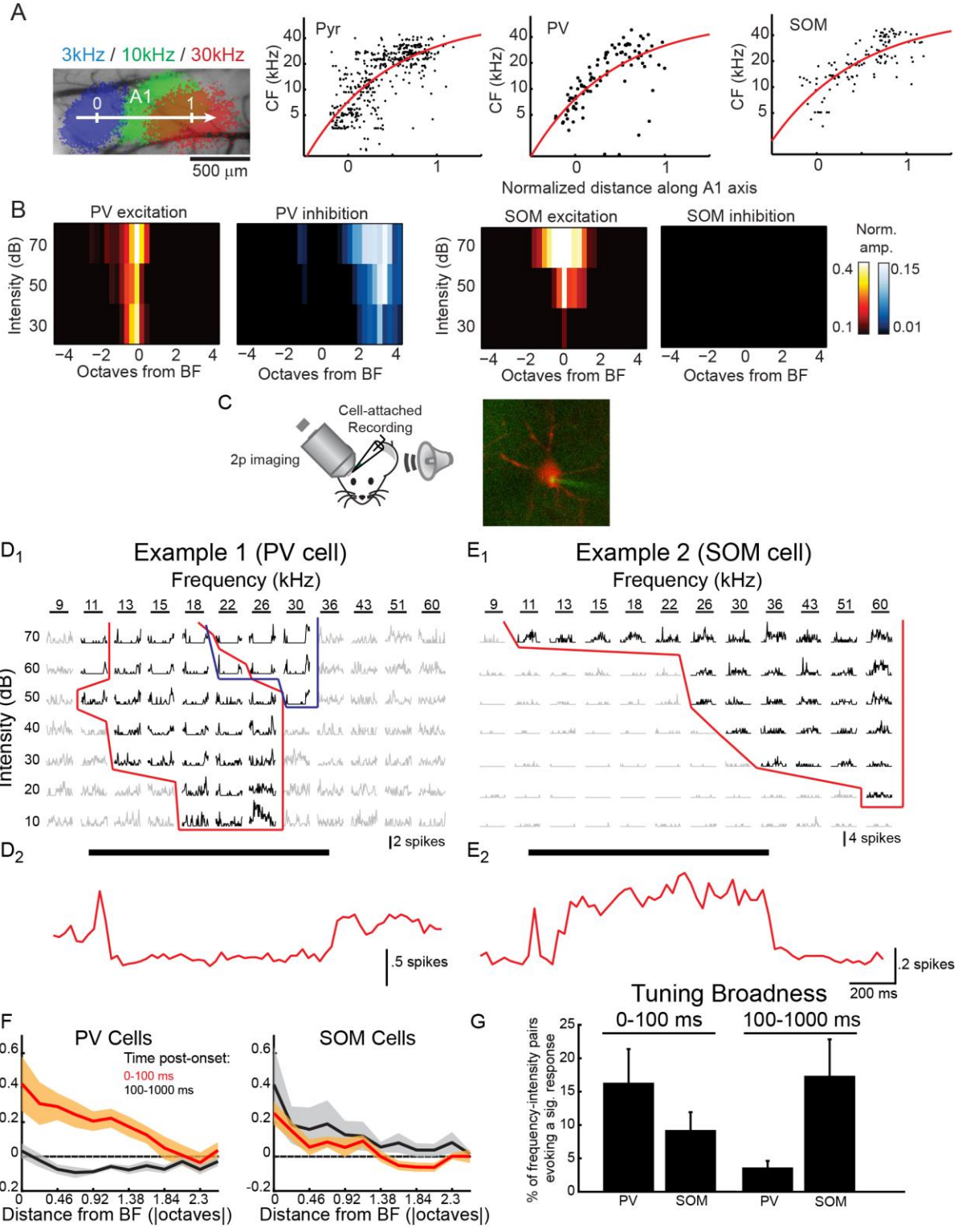
A
3kHz / 10kHz / 30kHz
A1
0
1
500 μm
Pyr
PV
SOM
CF (kHz)
Normalized distance along A1 axis
B
PV excitation
PV inhibition
SOM excitation
SOM inhibition
Intensity (dB)
Octaves from BF
Norm. amp.
C
Cell-attached Recording
2p imaging
D1
Example 1 (PV cell)
Frequency (kHz)
2 spikes
D2
.5 spikes
E1
Example 2 (SOM cell)
4 spikes
E2
.2 spikes
200 ms
F
PV Cells
SOM Cells
Time post-onset:
0-100 ms
100-1000 ms
Z-scored spiking
Distance from BF (|octaves|)
G
Tuning Broadness
0-100 ms
100-1000 ms
% of frequency-intensity pairs evoking a sig. response
PV
SOM

Next we explored spiking responses in these interneuron populations at a finer scale, using a 2-photon microscope to target juxtacellular recordings to individual identified L2/3 interneurons. We presented sustained pure tone stimuli (1 s, 4-60 kHz, 17 frequencies, 10-70 dB intensity levels) similar those used in the imaging experiments (Figure 1.4C). All recorded PV cells (n=9) fired spikes in response to the onset of some stimuli (BW70=1.64 ± 0.43, % of stimuli evoking a significant response=16.2 ± 5.13), but they rarely spiked over the last 900 ms of the sound (Figure 1.4D1-2, F,G). In the majority of these cells (6/9), some tones suppressed spiking below spontaneous rates (Figure 1.4D1, F). Importantly this inhibition had a longer latency than the onset response, its tuning did not overlap with the onset response in most cases, and it persisted for the duration of the entire tone (measured from 100-1000 ms after onset), all attributes consistent with spiking suppression via NS rather than tone-evoked IPSCs. VIP cells (n=9) also responded to tone onset. As previously reported, this spiking response was narrowly tuned across frequencies and highly intensity-tuned (data not shown; Mesik et al. 2015). The same cells often had a suppressive tonal receptive field; as in PV cells, spiking would cease for the duration of a stimulus. As described in other work (Li et al. 2015), some of the recorded SOM cells (n=8) responded weakly to the onset of a narrow range of frequencies. However, many of the recorded cells (5/8) displayed sustained spiking throughout the duration of the stimulus (measured 100-1000 ms after tone onset). Consistent with the responses we observed using calcium imaging (Figure 1.4A), this response was as or more broadly tuned as tone responses in PV cells (BW70 in 5 cells with a sustained response=2.57±.247 octaves, % of stimuli evoking a response=19.3±5.88, Figure 1.4G).

Figure 1.5. SOM Cells are necessary for suppression underlying lateral inhibition. A. SOM cell inactivation reduces tone-evoked network suppression. Top, schematic. Bottom, tone-evoked EPSCs and IPSCs from a representative cell with (brown) and without (black) SOM cell photoinactivation. Responses during photoinactivation were evoked 300 ms after LED onset and baselined to the 50 ms period before tone onset. Black bars, tones. **B.** Average magnitude of synaptic currents ($EPSC_{ON}$, $IPSC_{ON}$, $EPSC_{NS}$ and $IPSC_{NS}$) during LED on and LED off trials for responsive cell-tone pairs (n=7 cells, 5 mice). Dashed lines, unity. Black crosses, average. **C.** PV cell inactivation enhances network suppression. Top, schematic. Bottom, tone-evoked EPSCs and IPSCs of a representative cell with (brown) and without (black) PV cell photoinactivation. **D.** Average magnitude of response components during LED on and LED off trials for responsive cell-tone pairs (n=8 cells from 5 mice).

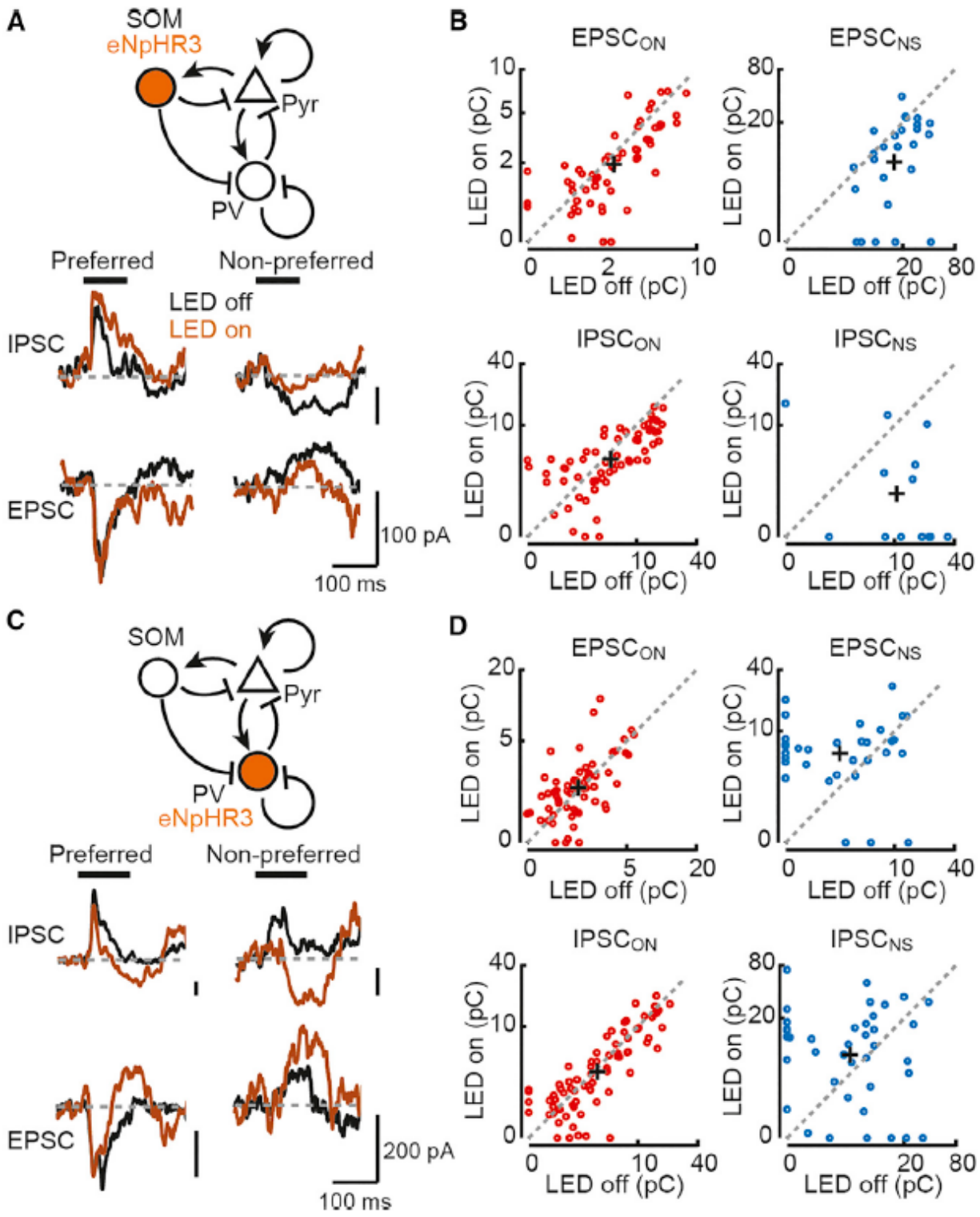
A
SOM
eNpHR3
Pyr
PV
Preferred
Non-preferred
LED off
LED on
IPSC
EPSC
100 pA
100 ms
B
EPSCON
EPSCNS
IPSCON
IPSCNS
LED on (pC)
LED off (pC)
C
SOM
Pyr
PV
eNpHR3
Preferred
Non-preferred
IPSC
EPSC
200 pA
100 ms
D
EPSCON
EPSCNS
IPSCON
IPSCNS
LED on (pC)
LED off (pC)

Based on these results, we predicted that SOM cells might be critical for triggering NS lateral inhibition. To confirm this, we tested how SOM and PV cell inactivation affected tone-evoked synaptic responses. Remarkably, levels of SOM cell photoinactivation with little effect on sound onset-locked direct responses significantly reduced slow, indirect responses to non-preferred tones (Figures 1.5A and 1.5B ; $EPSC_{NS}$ charge, $p = 0.002$; $IPSC_{NS}$ charge, $p = 0.011$; n = 7 cells, 5 mice). This shows that SOM cells provide inhibition critical for triggering network suppression. In contrast, PV cell photoinactivation that had little effect on direct responses significantly enhanced network suppression of EPSCs. The effect on network suppression of IPSCs was more variable, but had a tendency for enhancement (Figures 1.5C and 1.5D, $EPSC_{NS}$, $p = 0.004$; $IPSC_{NS}$, $p = 0.066$, n = 8 cells, 5 mice). The simplest explanation for this result is that PV cells do not underlie network suppression by non-preferred tones. Rather, PV cell inactivation increases the amount of spontaneous synaptic activity that SOM cells can suppress. Taken together, the bidirectional effects of these local interneuron populations rule out the possibility that network suppression is simply inherited from subcortical systems and reveal a necessary role for cortical SOM cells in lateral inhibition.

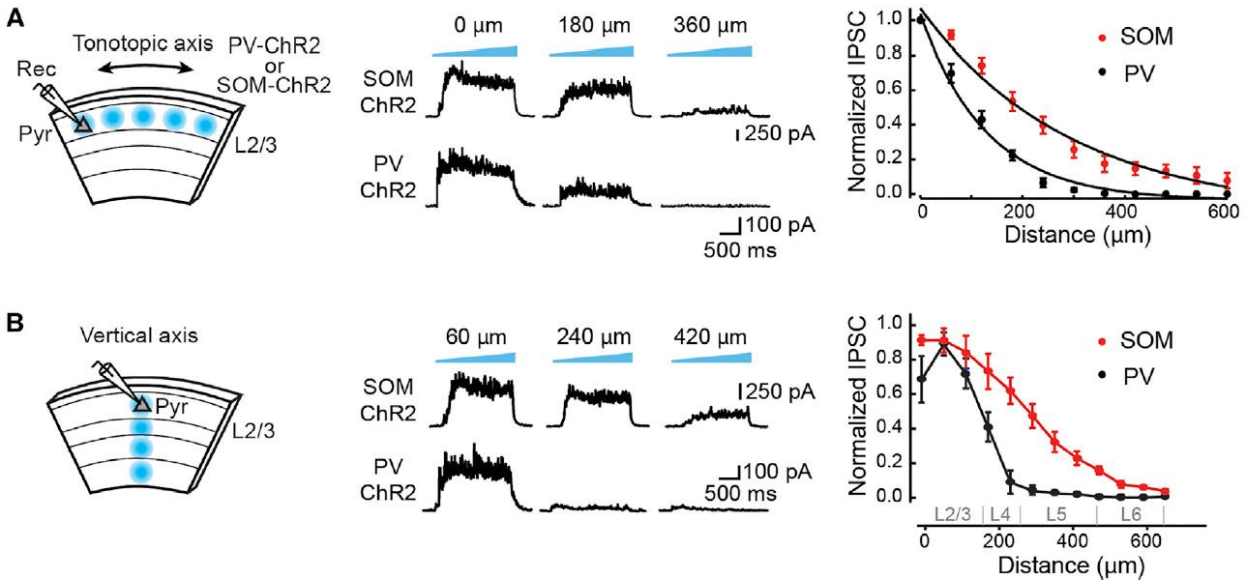

Figure 1.6. SOM cells inhibit wide regions of cortical space. A. Left, schematic of brain slice experiment using focal illumination along the tonotopic axis to test input onto L2/3 pyramidal cells from ChR2-expressing SOM and PV cells. Middle, IPSCs evoked by light ramps (blue, top) at increasing horizontal distances from the recorded cell body (0 µm) in a slice expressing ChR2 in SOM cells (upper traces) or PV cells (lower traces). Right, summary showing that SOM cells (red, n=12) provide inhibition over a greater horizontal distance than PV cells (black, n=12). Data (mean ± s.e.m.) are fit with a single exponential. Average normalized IPSC at 300 µm from the soma: PV=0.03±0.01, SOM=0.26±0.05
B. Same as in A but focal illumination is applied along a cortical column. Distance is plotted from cell body in L2/3 (0 µm) toward the white matter. Normalized IPSC at 300 um: PV=0.04±0.03, SOM=0.47±0.07, Student's t test $p<0.001$.

What mechanisms enable SOM cells to mediate lateral interactions across cortical frequency domains? One possibility is that SOM cells have preferred frequencies that are generally coherent to the A1 tonotopic axis but receive highly convergent horizontal excitatory input from across A1, similar to the proposed role for SOM cells in V1 surround suppression (Adesnik et al. 2012). Consistent with this, SOM cells have broadly tuned sensory responses (Figure 1.4B, E, F, G). However, it is unclear if SOM cells are tuned broadly enough to mediate network suppression lateral

inhibition (especially within the first 100 ms of a tone, when network suppression is initiated), which can be triggered by tones up to 3-4 octaves from a cell's preferred frequency.

We next considered whether the horizontal range of SOM cell-mediated inhibition could contribute to distant lateral interactions in A1. To test this, we used focal (60 μm diameter) photoactivation at sites along the A1 tonotopic axis in slices from mice expressing channelrhodopsin-2 (ChR2) selectively in SOM or PV cells (Figure 1.6A). Recordings were performed in the presence of glutamate and $GABA_B$ receptor blockers and ramp illumination (470 nm, 0.2–2 s) was used to activate somatodendritic compartments of PV and SOM cells within the photostimulated area rather than ChR2-expressing axons (Adesnik and Scanziani 2010). We saw no difference in recordings from the low versus high-frequency regions of slices (data not shown), and results using either direction of stimulation along the tonotopic axis were pooled. L2/3 pyramidal cell IPSCs elicited by PV cell activation diminished rapidly as the photostimulus was moved laterally from the recorded cell (Figure 1.6A). In contrast, SOM cell-evoked inhibition was sustained over a greater distance (average length constant PV cells, 129 μm; SOM cells, 295 μm). Photostimulation along cortical columns revealed that SOM cells also provide more diffuse translaminar inhibition than PV cells (Figure 1.6B). Taken together, we propose that SOM cells mediate lateral interactions between distant A1 frequency domains through both the convergence of excitatory inputs and divergence of inhibitory outputs across horizontal cortical space.

Discussion

Lateral Inhibition in the Primary Auditory Cortex

In A1 of awake mice, ensemble imaging of L2/3 pyramidal cells reveals divergent receptive fields for tone frequencies that increase and suppress firing activity. Although previous unit recording studies in anesthetized animals did not describe suppressive TRFs using single tones (Calford and Semple 1995; Li et al. 2014; Phillips and Cynader 1985; Sutter et al. 1999), this is likely because anesthesia results in low levels of spontaneous activity that preclude measurement of firing suppression. Consistent with this idea, studies in awake animals report that single tones suppress spontaneous firing and suppressive TRFs extend octaves away from the neuron's best frequency (Kato et al. 2015; O'Connell et al. 2011; Pelleg-Toiba and Wollberg 1989; Sadagopan and Wang 2010; Shamma and Symmes 1985). Interestingly, the lateral inhibition of firing activity under our conditions shows a strong bias to the high-frequency side of excitatory TRFs. A similar bias has been reported for the frequency tuning of on and off responses in auditory cortex, with off responses tuned one to two octaves above on responses (Scholl et al. 2010). However, network suppression is not an off response, since it develops well before sound offset and has an opposite polarity. The bias we describe could result from the differential tuning of excitation and suppression we find along the 2–40 kHz tonotopic axis of A1; whereas the excitatory CFs of individual neurons matched their location along the macroscopic tonotopic axis, suppressive CFs showed a relatively uniform overrepresentation of higher frequencies all along A1. This position-invariant distribution of suppressive CFs supports the idea that the tuning of inhibition is

not determined by local activity, but rather by pooling activity across wide areas of A1. However, our results do not exclude the possibility that cells in other areas representing higher ultrasonic frequencies have suppressive TRFs biased to the low-frequency side of excitatory TRFs.

We used whole-cell recording in awake mice to reveal the synaptic mechanisms underlying lateral inhibition. Consistent with our imaging results, current clamp recordings revealed that non-preferred frequencies evoke strong membrane hyperpolarization sufficient to abolish pyramidal cell spike firing. The fact that hyperpolarization was elicited by frequencies octaves away from the best frequency for depolarization appears to contradict studies that used voltage clamp to isolate tone-evoked synaptic excitation and inhibition (Li et al. 2014; Tan and Wehr 2009; Wehr and Zador 2003; Wu et al. 2008; Zhang et al. 2003; Zhou et al. 2014). Although these studies include cells in multiple layers and vary with respect to the absolute tuning broadness reported for inhibition, they all come to the conclusion that tuning curves for synaptic excitation and inhibition are largely overlapping. Importantly, using voltage-clamp recording, we show that this discrepancy can be explained by the presence of two different components underlying sound-evoked responses in A1. First, consistent with previous reports, we show that tones evoke sound onset-locked synaptic responses and that evoked IPSCs are tuned to a slightly broader range of frequencies than those that evoke EPSCs. However, the TRFs for these conventional sound-evoked IPSCs cannot account for suppression of firing activity that is octaves away from a neuron’s best frequency. Instead, we demonstrate that this lateral inhibition is caused by a second, previously undocumented component of sound-evoked responses: the

suppression of both excitatory and inhibitory synaptic inputs. The suppression of spontaneous activity has a longer latency and slower time course than onset-locked increases in synaptic activity. More importantly, the TRF of sound-evoked network suppression diverges from the tuning of onset-locked inputs and covers a frequency range that can be octaves away from the preferred frequency for onset-locked responses.

The network suppression we report provides a synaptic mechanism for broad lateral inhibition of firing activity. Interestingly, in unit recordings, the kinetics of two-tone suppression of neuronal firing differ between frequency domains that are proximal or distal to the neuron's preferred frequency (Sadagopan and Wang 2010; Sutter and Loftus 2003). One possibility is that "lateral inhibition" actually consists of multiple distinct mechanisms: in the frequency domain around the excitatory synaptic TRF, a slightly broader TRF for sound onset-locked inhibition sharpens neuronal firing via the iceberg effect. In contrast, in the frequency domain distal to the preferred frequency, lateral inhibition is enabled by the slow network suppression of ongoing recurrent synaptic activity. In primates, suppression observed at the population level has also been attributed to a combination of feedforward inhibition and a phase reset of ongoing cortical oscillations (O'Connell et al. 2011). It is likely that multiple mechanisms work together to shape cortical dynamics and generate lateral inhibition in the awake brain.

Why have prior *in vivo* whole-cell recording studies not reported the slow network suppression we observe in the majority of recorded neurons? We found that brief (15 ms) tone pips elicit very weak network suppression, thus it may simply have been

missed in previous studies that did not use stimuli of sufficient duration. We think the use of anesthetics in most previous studies is also a major factor. Anesthesia dampens activity in many neural circuits, and spontaneous activity of A1 neurons is much higher in awake animals (Gao et al. 2016; Kato et al. 2015). Indeed, the continuous high-frequency barrages of spontaneous excitatory and inhibitory inputs we observe differ from the generally “quiet” baseline activity observed in previous studies using *in vivo* voltage-clamp recording. However, even in our recordings in awake animals, we observed conditions that compromised cortical activity. Low levels of spontaneous activity and TRFs lacking slow network suppression were observed when the pipette internal solution contained QX-314, an intracellular blocker of voltage-gated Na+ and Ca2+ channels (Strichartz 1973; Talbot and Sayer 1996) often used in millimolar concentrations for recordings of synaptic transmission (Li et al. 2014; Scholl et al. 2010; Wehr and Zador 2003; Zhou et al. 2014). However, micromolar QX-314 blocks action potentials in a use-dependent manner when applied extracellularly (Hessler et al. 1993). Given the positive pipette pressure used when searching for cells with blind whole-cell recording, spill of QX-314 should cause a long-lasting reduction in network activity. Thus, factors such as stimulus duration, anesthesia, QX-314 pipette solutions, and cortical damage could have resulted in low spontaneous cortical activity in prior studies, and likely precluded the detection of network suppression. Regardless of the reasons for the difference, our intracellular results can entirely account for the lateral inhibition of firing activity we observed. Thus, we believe network suppression is likely to be a physiological phenomenon that shapes frequency tuning in the auditory cortex of awake animals.

Inhibitory Neuron Circuits in the Primary Auditory Cortex

We demonstrate that SOM cells, but not PV cells, are critical for the triggering of network suppression by non-preferred stimuli. This result suggests that SOM cells mediate lateral inhibition by linking spatially distant frequency domains of A1. Indeed, we show that SOM cells are the most broadly frequency tuned cells in L2/3 suggesting a convergence of frequency information from wide A1 areas onto individual SOM cells. In contrast, PV cells are only slightly more broadly tuned than pyramidal cells. This is consistent with a previous study reporting the similar frequency tuning of PV and pyramidal cells in A1 (Moore and Wehr 2013). These results suggest that PV cell activity arises from information sampled from local pyramidal cells. Although another study in A1 of anesthetized animals suggested that PV cells are more broadly tuned than SOM or pyramidal cells (Li et al. 2015), this may be due to the fact that anesthesia strongly attenuates SOM cell activity (Adesnik et al. 2012). Similar to our findings in A1, SOM cells in primary visual cortex are reported to integrate horizontal inputs across wide regions of cortical space, and this convergence underlies surround suppression across retinotopic domains (Adesnik et al. 2012). Therefore, lateral inhibition mediated by broadly tuned SOM cells is likely to be a general mechanism across sensory cortices.

In our study, the tuning broadness of SOM cells in A1 (BW70 from imaging experiments, 2.1 ± 0.1 octaves; BW70 of sustained responses from juxtacellular recordings 2.57±.247 octaves) is not enough to fully account for the lateral inhibition that covers up to three to four octaves away from an individual neuron's preferred frequency. This suggests the presence of an additional mechanism by which SOM cells regulate

lateral interactions. Indeed, using focal photoactivation of interneurons along the A1 tonotopic axis, we demonstrate that SOM cell-mediated inhibition extends over 500 μm, which corresponds to over two octaves along the A1 tonotopic axis (determined from intrinsic imaging). This broad inhibitory output range gives SOM cells an additional ability to link laterally distributed cortical areas. Curiously, the inhibitory range observed in our study is double the distance reported by a previous study (Li et al. 2014). This difference is possibly attributed to our use of a slow ramping photostimulus which is more effective in firing action potentials from intact cells than bypassing axons (Adesnik and Scanziani 2010). Alternatively, the difference could be explained by our use of cortical slices maintaining the A1 tonotopic axis. Taken together, our results demonstrate that lateral inhibition in A1 is mediated by both the convergence of inputs onto SOM cells and divergence of outputs from SOM cells. These results suggest that SOM cells work as a hub for the lateral flow of information in cortical circuits, and regulate the integration of information across spatially distributed auditory frequency domains.

Operating Regime of Inhibition in Cortical Networks

In highly interconnected cortical circuits, activity of one neuron affects others not just via direct synaptic input, but also via a cascade of indirect network-level effects. The suppression of both excitatory and inhibitory inputs by non-preferred tones indicates that SOM cells trigger lateral inhibition not through direct inhibitory input onto pyramidal cells, but rather through a suppression of recurrent excitation in the A1 network. This result is consistent with the operation of A1 as an ISN, a network model where strong recurrent excitation in the circuit is constantly regulated by inhibition to prevent run-

away activity (Litwin-Kumar et al. 2016; Ozeki et al. 2009; Rubin et al. 2015; Tsodyks et al. 1997). Our observation of a paradoxical increase in IPSCs during optogenetic inactivation of inhibitory neurons further supports this model (Tsodyks et al. 1997). We note that simultaneous suppression of both excitation and inhibition could also be explained by another mechanism. For example, SOM cells could suppress pyramidal cell activity via silent, shunting inhibition while at the same time inhibiting PV cells that provide the majority of conventional pyramidal cell IPSCs. However, this model fails to explain the paradoxical increase in inhibitory inputs during optogenetic inactivation of PV cells, and therefore the most parsimonious explanation is that A1 in awake brain operates as an ISN. Nevertheless, our results do not exclude the possibility that both mechanisms contribute to the ability of SOM cells to mediate network suppression during lateral inhibition.

Whether or not cortical circuits operate in a regime of strong recurrent excitation and indirect effects of inhibitory interneurons is a subject of debate. In visual cortex, while results consistent with ISN behavior have been observed (Ozeki et al. 2009; Sato et al. 2016), other studies are more consistent with weak recurrent excitation and direct inhibition of pyramidal cells (Adesnik et al. 2012; Atallah et al. 2012; Haider et al. 2010; Haider et al. 2013). It is plausible that, in the anesthetized state, where most neurons are sitting far below firing threshold, sensory stimuli fail to recruit recurrent excitation. In the awake state, in contrast, since neurons are already close to firing threshold even without sensory stimuli (Constantinople and Bruno 2011; Reinhold et al. 2015; Steriade et al. 2001), sensory inputs can recruit strong recurrent excitation from horizontally connected neurons such that the cortical circuits operate as an ISN. One intriguing

possibility is that those two circuit operation regimes are not mutually exclusive, but rather form a continuous spectrum of operation modes that is determined by the level of arousal (McGinley et al. 2015). In future, it would be of interest to investigate how lateral inhibition is affected by various brain states associated with arousal, attention (Zhang et al. 2014) or behavior (Kato et al. 2015; Schneider et al. 2014).

Implications for Auditory Processing in A1 Circuits

The unique spectro-temporal features of network suppression provide A1 neurons an expanded capacity for auditory processing. One aspect that distinctly differentiates network suppression from sound onset-locked inhibition is its shifted tuning. We find that network suppression in individual cells can be evoked by frequencies as high as four octaves away from the neurons' preferred frequency. This extended domain of inhibition not only sharpens the frequency tuning of individual A1 neurons against single tones, but it could also provide neurons with a spectral filter against sound stimuli with multiple frequencies. For example, presentation of high-frequency target sounds could trigger network suppression throughout the entire A1 tonotopic axis and thus filter out broadband background noise to enhance the saliency of the target. This idea is of special interest, considering the bias of network suppression toward high frequencies (20–40 kHz). Mice use high-frequency ultrasonic vocalizations to communicate with each other, and behaviorally are most sensitive to frequencies in this range (Mikaelian et al. 1974). This strong sensitivity to ultrasonic frequencies may be further enhanced by lateral inhibition that extends from the high-frequency to low-frequency domain of A1. It is possible that the mouse auditory system is organized to suppress responses to low-frequency sounds in the presence of high-

frequency sounds, such that behaviorally relevant ultrasonic vocalizations are preferentially processed to guide behavior.

Another important aspect that differentiates network suppression from sound onset-locked inhibition is its prolonged duration. In contrast to transient sound onset-locked inhibition that usually lasts for less than 50 ms (Wehr and Zador 2003, Wehr and Zador 2005, Zhang et al. 2003, Zhou et al. 2014), network suppression lasts considerably longer. This prolonged suppression allows individual A1 neurons to integrate information over longer time periods. For example, we find that prolonged network suppression can follow transient excitatory synaptic responses even at the preferred frequencies of neurons (Figure 1.4B). It may be the case that slow network suppression contributes to forward suppression (masking), where a preferred frequency tone can suppress responses to a subsequent tone delivered hundreds of milliseconds later (Wehr and Zador 2005). Ultimately, through the recruitment of reverberating recurrent circuits, network suppression expands the capacity for cortical integration along both the spatial and temporal domains.

Chapter 1 contains material previously published in: Kato HK, Asinof SK, Isaacson JS (2017). Network-Level Control of Frequency Tuning in Auditory Cortex. *Neuron*; 95(2):412-423. The dissertation author was a co-author of this paper.

Materials and Methods

Experimental model and subject details

Mice between 6 and 10 weeks of age were used for all experiments. Mice were acquired from Jackson Laboratories (*GAD2* –Cre, PV-Cre, SOM -Cre, *VIP-Cre*, *Rosa-LSL-ChR2(H134R)-EYFP*, and *Rosa-LSL-tdTomato*). Both female and male animals were used and maintained on a 12:12 reversed light:dark cycle. Experiments were performed during the dark period. Mice had no prior history of experimental procedures that could affect the results. All procedures were in accordance with protocols approved by the UCSD Institutional Animal Care and Use Committee and guidelines of the National Institute of Health.

Preparation for *in vivo* two-photon imaging

Glass windows for calcium imaging were implanted as described previously (Kato et al., 2015). In summary, mice were anaesthetized with isoflurane and injected with dexamethasone (2 mg/kg) intraperitoneally. A custom stainless steel head-bar was glued to the skull. Muscle overlying the right auditory cortex was removed and a craniotomy (~2 × 3 mm) was made, leaving the dura intact. Viruses (AAV2/9.syn.GCaMP6s.WPRE.SV40, AAV2/9.syn.FLEX.GCaMP6s.WPRE.SV40) were injected at 5-15 locations (250 μm deep from the pial surface, 20-30 nl/site). A glass window was placed over the craniotomy and secured with dental acrylic. Baytril (10 mg/kg) and buprenorphine (0.1 mg/kg) were injected before mice were returned to their home cages.

Preparation for *in vivo* electrophysiology

A head-bar was implanted as described for calcium imaging, and intrinsic signal imaging was performed through the intact skull. After mapping auditory cortex, the exposed skull was covered with silicone elastomer (KwikCast, WPI), and the mouse received buprenorphine (0.1 mg/kg) before returning to the home cage. 1-5 days later, mice were anaesthetized with isoflurane and the skull was exposed by removing the silicone cover. A small (< 0.3 mm diameter) craniotomy was made above A1 and a durotomy was made in some experiments. Special care was taken to reduce damage to the brain tissue during this surgery, since we observed abnormal activity from damaged tissue (see below). We found it critical to interrupt drilling every 1-2 s and cool the skull with artificial cerebrospinal fluid (aCSF, in mM: 142 NaCl, 5 KCl, 10 glucose, 10 HEPES, 3.1 $CaCl_2$, 1.3 $MgCl_2$, pH 7.4) to prevent damage from overheating. Craniotomies were covered with aCSF and mice recovered from anesthesia for > 1.5 hr before whole-cell recording.

Preparation for *in vivo* targeted juxtacellular recordings

A head-bar was implanted as described for calcium imaging, and intrinsic signal imaging was performed through the intact skull. After mapping auditory cortex, the exposed skull was covered with silicone elastomer (KwikCast, WPI), and the mouse received buprenorphine (0.1 mg/kg) before returning to the home cage. 1-5 days later, mice were anaesthetized with isoflurane and the skull was exposed by removing the silicone cover. A ~2 mm circular craniotomy was performed over right A1 and

surrounding cortex and a semicircular coverslip with half of that area was adhered to the cortical surface, covering A1. Special care was taken during drilling to prevent damage from overheating. Mice recovered for at least 2 hours prior to recording.

Sound stimulus presentation

Auditory stimuli were delivered via a free-field electrostatic speaker (ES1; Tucker-Davis Technologies). For intrinsic and calcium imaging, speakers were calibrated over a range of 2-40 kHz to give a flat response (±1 dB). For in vivo whole-cell and juxtacellular recording, speakers were calibrated over a range of 4-60 kHz. Stimuli were delivered to the ear contralateral to imaging or recording. Auditory stimulus delivery was controlled by software (BControl; http://brodylab.org) running on MATLAB (MathWorks) communicating with a real-time system (RTLinux).

Intrinsic signal imaging

Intrinsic signal images were acquired using a tandem lens macroscope and 12 bit, CCD camera (CCD-1300QF, VDS Vosskühler). Mice were isoflurane-anaesthetized and injected with chlorprothixene (1.5 mg/kg, i.p.). Images of surface vasculature were acquired using green LED illumination (530 nm) and intrinsic signals were recorded (27 Hz) using red illumination (615 nm). Each trial consisted of 1 s baseline followed by a 1 s sound stimulus (75 dB pure tone with a frequency of 3, 10, or 30 kHz, 10-20 trials for each frequency) and 30 s inter-trial interval. Images of reflectance were acquired at 1024 × 1024 pixels (covering ~2.1 × 2.1 mm) and downsampled to 512 × 512 pixels by bilinear interpolation. Images during the response period (0.5-2 s from the sound onset)

were averaged and divided by the average image during the baseline. Images were averaged across trials and Gaussian filtered.

In vivo two-photon calcium imaging

Two-photon calcium imaging was performed ~three weeks after chronic window implantation to ensure an appropriate level of GCaMP6s expression. Intrinsic signal imaging was performed through chronic windows 1-3 days before calcium imaging to locate A1. On the day of calcium imaging, mice were head-fixed under the two-photon microscope in the awake state. GCaMP6s and tdTomato were excited at 920 nm (Mai Tai, Newport), and images (512 × 512 pixels covering ~500 × 500 μm) were acquired with a commercial microscope (B-scope, Thorlabs) running Scanimage software using a 16 × objective (Nikon) at 28.4 Hz. Images were acquired from L2/3 (120-250 μm below the surface). Lateral motion was corrected by cross correlation-based image alignment.

In vivo whole-cell recording

Mice were acclimated to handling and head-fixation several days prior to recording. During recording, awake mice sat quietly (with occasional bouts of whisking and grooming) in a loosely fitted plastic tube within a sound attenuating enclosure. Whole-cell patch-clamp recordings were made with the blind technique. Most recorded cells were located in L2/3, based on the z axis readout of an MP-285 micromanipulator (Sutter; 200-300 μm from the pial surface). Voltage-clamp recordings were made with patch pipettes (3-4.5 MOhm) filled with internal solution composed of (in mM) 130 cesium gluconate, 10 HEPES, 5 TEA-Cl, 12 Na-phosphocreatine, 0.2 EGTA, 3 Mg-ATP,

and 0.2 Na-GTP (7.2 pH; 310 mOsm). EPSCs and IPSCs were recorded at −70 mV and +20 mV, near the reversal potentials for inhibition and excitation, respectively, set by our internal solution. Membrane potential values were not corrected for the ~15 mV liquid junction potential and series resistance was continuously monitored for stability (average 32.8 ± 2.1 MOhm, n = 38 cells). Current-clamp recordings were made with patch pipettes filled with internal solution composed of (in mM) 130 potassium gluconate, 5 NaCl, 10 HEPES, 12 Na-phosphocreatine, 0.2 EGTA, 3 Mg-ATP, and 0.2 Na-GTP (7.2 pH; 310 mOsm), except for input resistance measurements, in which the same internal solution as voltage-clamp recordings was used. Recordings were made with a MultiClamp 700A (Molecular Devices), digitized at 5-10 kHz (ITC-18, Instrutech), and acquired using AxographX (Axograph).

In awake mice, we observed a continuous barrage of spontaneous EPSCs and IPSCs (Figure 1.2). Although previous studies reported low basal activity with intermittent spontaneous or sound-evoked bursts (Grienberger et al., 2012, Hromádka et al., 2008), we only observed bursting synaptic activity in damaged preparations (e.g., bleeding brain tissue, tissue overheated during drilling, or too many electrode penetrations). Since detection of network suppression was critically dependent on the presence of intact spontaneous activity, recordings were not performed in mice with surgical damage. Furthermore, experiments were terminated after 5-10 pipette penetrations when bursting activity appeared in recordings of EPSCs or field EPSPs.

In vivo targeted juxtacellular recordings

Pipettes containing aCSF and 25 μm Alexa-488 were lowered into A1 (via the uncovered side of the craniotomy) under the guidance of a commercial two-photon microscope (BScope, ThorLabs). Alexa-488 and tdTomato were excited at 950 nm (Mai Tai, Newport). tdTomato-expressing cells were recorded juxtacellularly with a MultiClamp 700B (Molecular Devices) in voltage-clamp configuration, digitized at 20 kHz (ITC-18, Instrutech), and acquired using AxographX (Axograph). Traces were band-pass filtered (50-4000 Hz) to remove drifting baseline and high-frequency noise. Capacitive currents associated with recorded cells were many-fold stronger than the background noise (which was ≤25 pA), and were detected using an amplitude threshold.

In vivo optogenetic inactivation of interneurons

For inactivation of specific interneuron subtypes, AAV2/9.EF1a.DIO.eNpHR3.0.EYFP.WPRE.hGH was injected into the right auditory cortex of newborn *SOM–Cre* or *PV–Cre* mice (postnatal day 1–2). Pups were anaesthetized by hypothermia and secured in a molded platform. Virus was injected at three locations along the rostral-caudal axis of the auditory cortex. At each site, injection was performed at three depths (600, 500, and 400 μm deep from the skin surface, 23 nl/depth). Six weeks after injections, *in vivo* voltage-clamp experiments were performed as described above, except that the entire skull over A1 was thinned to improve light penetration. A fiber-coupled LED (595 nm) was positioned 1-2 mm above the thinned skull. In interleaved trials, LED illumination was delivered that lasted from 200-300 ms

before sound onset to 300 ms after sound offset. LED intensity was kept at the lowest effective intensity (~5-10 mW) to prevent aberrant sound-evoked cortical activity.

Slice electrophysiology

For expressing ChR2 in genetically-identified interneurons, the following three methods were used: 1) AAV2/9.EF1a.DIO.hChR2(H134R).EYFP.WPRE.hGH or AAV2/9.CAGS.FLEX.hChR2(H134R).tdTomato.WPRE.SV40 was injected in the right A1 of adult *SOM-Cre* or *PV-Cre* mice, 2) AAV2/9.EF1a.DIO.hChR2(H134R).EYFP.WPRE.hGH was injected into the right auditory cortex of newborn *SOM–Cre* or *PV–Cre* mice, or 3) *SOM-Cre* or *PV-Cre* mice crossed with *Rosa-LSL-ChR2(H134R)-EYFP* mice. We did not observe differences between these conditions, and results were pooled. Slice electrophysiology experiments were performed in 6-12 week old mice, at least 10 days after virus injection. To prepare cortical slices that preserved A1 along its tonotopic axis, mice were anaesthetized with isoflurane and intrinsic signal imaging was performed to map auditory areas. Small craniotomies (< 300 μm) were then made at the low- and high-frequency poles of the A1 tonotopic axis, and fluorescent beads (Lumifluor, 60-100 nl/site) were injected as landmarks. Mice were then anaesthetized with ketamine (200 mg/kg) and perfused with ice cold artificial cerebrospinal fluid (aCSF) containing (in mM) 83 NaCl, 2.5 KCl_2, 0.5 $CaCl_2$, 3.3 $MgSO_4$, 1 NaH_2PO_4, 26.2 $NaHCO_3$, 22 glucose, and 72 sucrose, equilibrated with 95% O_2 and 5% CO_2. The brain was removed and A1 cortical slices (500 μm thick) were cut perpendicular to the cortical surface at an angle such that the slice contained both bead-injection sites. Patch-clamp recordings were performed using an upright

microscope and DIC optics. Recordings were made using a Multiclamp 700A amplifier, digitized at 20 kHz, and acquired and analyzed using AxographX software. Voltage-clamp recordings were made with patch pipettes (3-4.5 MOhm) filled with internal solution composed of (in mM) 130 cesium gluconate, 10 HEPES, 5 TEA-Cl, 12 Na-phosphocreatine, 0.2 EGTA, 3 Mg-ATP, and 0.2 Na-GTP (7.2 pH; 310 mOsm). Slices were superfused with aCSF containing (in mM): 119 NaCl, 5 KCl, 2.5 $CaCl_2$, 1.3 $MgSO_4$, 1 NaH_2PO_4, 26.2 $NaHCO_3$ and 22 glucose, equilibrated with 95% O_2 and 5% CO_2. All experiments were conducted in the presence of NBQX (10 μM, Tocris) and CGP55845 (10 μM, Tocris) at 30–32°C. IPSCs were recorded at 0 mV. Membrane potential values were not corrected for the liquid junction potential. Series resistance was routinely < 20 MOhm and continuously monitored. A collimated LED light source (470 nm, Thorlabs) was directed through a diaphragm and a 60 × microscope objective and restricted to a small spot (~60 μm diameter).

Quantification and statistical analysis

All data are presented as mean ± SEM. Statistically significant differences between conditions were determined using standard parametric or nonparametric tests in MATLAB. A two-tailed paired t test was used, unless otherwise stated. A nonparametric test (Wilcoxon signed rank test) was used to confirm statistical significances reported by t tests. All “n” values refer to the number of cells except when explicitly stated that the n is referring to the number of mice. Experiments were not performed blind. Sample sizes were not predetermined by statistical methods, but were based on those commonly used in the field.

Analysis of two-photon imaging data

Regions of interest (ROIs) corresponding to visually identifiable cells were manually drawn, and pixels within each ROI were averaged to create a fluorescence time series $F_{cell\_measured}(t)$. To correct for neuropil contamination, ring-shaped background ROIs (starting at 2 pixels and ending at 8 pixels from the border of the ROI) were created around each cell ROI. From this background ROI, pixels that contained cell bodies or processes from surrounding cells were excluded. The remaining pixels were averaged to create a background fluorescence time series $F_{background}(t)$. The fluorescence signal of a cell body was estimated as $F(t) = F_{cell\_measured}(t) - 0.9 \times F_{background}(t)$. To ensure robust neuropil subtraction, only cell ROIs that were at least 3% brighter than the background ROIs were included. Sound-evoked responses were measured during one second tone presentations. Cells were judged as significantly excited (inhibited) if they fulfilled two criteria: 1) dF/F had to exceed a fixed threshold value consecutively for at least 0.5 s in more than half of trials. 2) dF/F averaged across trials had to exceed a fixed threshold value consecutively for at least 0.5 s. Threshold for excitation (1.9 × standard deviation during baseline period) was determined by receiver operator characteristic (ROC) analysis to yield a 90% true positive rate in receptive field measurements. Since inhibitory responses tend to be small in amplitude, the threshold for inhibition was set as half that for excitation (−0.95 × standard deviation) to increase detection sensitivity. Two-photon imaging fields were aligned with the intrinsic signal imaging fields by comparing blood vessel patterns. Tonotopic positions of individual neurons in A1 were determined as the normalized distances such that ‘0’ corresponds to the center of the 3 kHz-responding area, and ‘1’

corresponds to the center of the 30 kHz-responding area of intrinsic signal imaging. If the center of the 10 kHz-responding area was not aligned to the 3 kHz- and 30 kHz centers, the field was warped so that the three landmarks form a straight line. BF was calculated as the frequency with the strongest response independent of tone intensity. For CF measurements, some cells had sound intensity thresholds lower than our lowest tested sound intensity (30 dB). CFs in these cells were estimated as the average of two measurements: 1) frequency with strongest response at lowest sound intensity, and 2) mean frequency of a fitted Gaussian for the responses across frequencies at lowest sound intensity (Issa et al., 2014).

Analysis of tuning curve shapes of individual neurons

TRF shapes of individual imaged cells were classified into six categories by visual inspection of excitatory responses: V-shaped, V-unfilled, slanted, inverse-V, O-shaped, and random. TRF bandwidth of a neuron at each sound intensity was calculated as the average of the range of frequencies that evoked significant excitatory responses, and the range of frequencies in which a Gaussian fit to the peak amplitude-versus-frequency plot exceeds threshold value (1.9 × standard deviation during baseline period). Tuning broadness of each neuron was evaluated using three distinct measures: 1). Bandwidth_{20}, determined as the bandwidth of the TRF at 20 dB above threshold intensity (considering only cells with V-shaped, V-unfilled, or slanted TRFs). 2). Bandwidth at 70 dB SPL (considering only the cells with V-shaped, V-unfilled, or slanted TRFs). 3). Lifetime sparseness (Rolls and Tovee, 1995, Willmore and Tolhurst, 2001),

which was calculated as $(1-\{[\sum j=1,Nrj/N]^2/[\sum j=1,Nrj^2/N]\})/(1-1/N)$, where r_j was the response peak amplitude of the cell to tone j, and N was the total number of tones.

1 – *Sp* provides a measure of how much the response probability of a neuron was distributed equally among all tones (non-selective: 1 - *Sp* = 1) versus attributable entirely to one tone (highly selective: 1 - *Sp* = 0). Since calculation of 1 - *Sp* does not rely on the TRF shape, it can also be used for quantifying the selectivity of inhibitory responses, which often do not have clear V-shape.

Analysis of *in vivo* electrophysiology

Data were analyzed using custom programs in MATLAB. Sound-evoked responses were measured using 100 ms tone presentations, except for current-clamp recordings and input resistance measurements, where tone durations were 200 ms and 500 ms, respectively. $EPSC_{ON}$ ($IPSC_{ON}$) was measured as negative (positive)-going current 20-40 ms after tone onset, and $EPSC_{NS}$ ($IPSC_{NS}$) was measured as positive (negative)-going current 50-175 ms after tone onset. Cells were judged as responsive to specific combinations of frequency and volume if they fulfilled two criteria: (1) the traces exceed a fixed threshold value consecutively for at least half the duration of detection window (i.e., 10 ms for $EPSC_{ON}$ and $IPSC_{ON}$, and 62.5 ms for $EPSC_{NS}$ and $IPSC_{NS}$) in more than half of trials, and (2) the averaged trace across trials exceed a fixed threshold value consecutively for at least half the duration of detection window. Threshold for $EPSC_{ON}$ and $IPSC_{ON}$ was set as 0.5 × standard deviation during baseline, and threshold for $EPSC_{NS}$ and $IPSC_{NS}$ was set as 0.3 × standard deviation during baseline.

For targeted juxtacellular recordings, we examined two windows to assess response significance: 0-100 ms after tone onset (onset responses) and 100-1000 ms after tone onset (sustained responses and sustained suppression). Response significance was determined by a bootstrapping procedure. First, spike counts from all trials were binned at a 25 ms interval. All baseline periods from each trial were concatenated. Baseline spiking was randomly sampled from this distribution (10000 iterations) in either 100 or 900 ms windows to devise a distribution of baseline spiking which would be expected either in the first 100 ms of a tone or the final 900 ms. Finally, we compared mean spike counts in these two windows to the bootstrapped distributions. Responses were judged significant if they in the top (or bottom) 5^{th} percentile of the resampled baseline distribution. For comparison between cells, binned spike trains were converted to Z-score values. Tuning broadness was measured as the bandwidth of significant responses from V-shaped, V-unfulfilled, or slanted tuning curves at 70 dB (BW70) or as the percentage of all frequency-intensity pairs evoking a significant response.

References

Adesnik H and Scanziani M (2010). Lateral competition for cortical space by layer-specific horizontal circuits. Nature 464, 1155–1160.

Adesnik H, Bruns W, Taniguchi H, Huang ZJ, and Scanziani M (2012). A neural circuit for spatial summation in visual cortex. Nature 490, 226–231.

Atallah BV, Bruns W, Carandini M, and Scanziani M (2012). Parvalbumin-expressing interneurons linearly transform cortical responses to visual stimuli. Neuron 73, 159–170.

Calford MB and Semple MN (1995). Monaural inhibition in cat auditory cortex. J. Neurophysiol. 73, 1876–1891.

Carandini M and Ferster D (2000). Membrane potential and firing rate in cat primary visual cortex. J. Neurosci. 20, 470–484.

Constantinople CM, and Bruno RM (2011). Effects and mechanisms of wakefulness on local cortical networks. Neuron 69, 1061–1068.

Gao L, Kostlan K, Wang Y, and Wang X (2016). Distinct subthreshold mechanisms underlying rate-coding principles in primate auditory cortex. Neuron 91, 905–919.

Grienberger C, Adelsberger H, Stroh A, Milos R-I, Garaschuk O, Schierloh A, Nelken I, and Konnerth A. (2012). Sound-evoked network calcium transients in mouse auditory cortex in vivo. J. Physiol. 590, 899–918.

Haider B, Krause MR, Duque A, Yu Y, Touryan J, Mazer JA, and McCormick DA (2010). Synaptic and network mechanisms of sparse and reliable visual cortical activity during nonclassical receptive field stimulation. Neuron 65, 107–121.

Haider B, Hausser M, and Carandini M (2013). Inhibition dominates sensory responses in the awake cortex. Nature 493, 97–100.

Hartline HK, Wagner HG, and Ratliff F (1956). Inhibition in the eye of Limulus. J. Gen. Physiol. 39, 651–673.

Hessler NA, Shirke AM, and Malinow R. (1993). The probability of transmitter release at a mammalian central synapse. Nature 366, 569–572.

Hromadka T, Deweese MR, and Zador AM. (2008). Sparse representation of sounds in the unanesthetized auditory cortex. PLoS Biol. 6, e16.

Isaacson JS and Scanziani M (2011). How inhibition shapes cortical activity. Neuron 72, 231–243.

Issa JB, Haeffele BD, Agarwal A, Bergles DE, Young ED, and Yue DT (2014). Multiscale optical Ca2+ imaging of tonal organization in mouse auditory cortex. Neuron 83, 944–959.

Kato HK, Gillet SN, and Isaacson JS (2015). Flexible sensory representations in auditory cortex driven by behavioral relevance. Neuron 88, 1027–1039.

Li LY, Li YT, Zhou M, Tao HW, and Zhang LI (2013). Intracortical multiplication of thalamocortical signals in mouse auditory cortex. Nat. Neurosci. 16, 1179–1181.

Li LY, Ji XY, Liang F, Li YT, Xiao Z, Tao HW, and Zhang LI (2014). A feedforward inhibitory circuit mediates lateral refinement of sensory representation in upper layer 2/3 of mouse primary auditory cortex. J. Neurosci. 34, 13670–13683.

Li L-Y, Xiong XR, Ibrahim LA, Yuan W, Tao HW, and Zhang LI (2015). Differential receptive field properties of parvalbumin and somatostatin inhibitory neurons in mouse auditory cortex. Cereb. Cortex 25, 1782–1791.

Lien AD and Scanziani M (2013). Tuned thalamic excitation is amplified by visual cortical circuits. Nat. Neurosci. 16, 1315–1323.

Litwin-Kumar A, Rosenbaum R, and Doiron B (2016). Inhibitory stabilization and visual coding in cortical circuits with multiple interneuron subtypes. J. Neurophysiol. 115, 1399–1409.

Liu BH, Li YT, Ma WP, Pan CJ, Zhang LI, and Tao HW (2011). Broad inhibition sharpens orientation selectivity by expanding input dynamic range in mouse simple cells. Neuron 71, 542–554.

McGinley MJ, David SV, and McCormick DA (2015). Cortical Membrane Potential Signature of Optimal States for Sensory Signal Detection. Neuron 87, 179–192. 422 Neuron 95, 412–423, July 19, 2017

Mesik L, Ma WP, Li LY, Ibrahim LA, Huang ZJ, Zhang LI, Tao HW (2015). Functional response properties of VIP-expressing inhibitory neurons in mouse visual and auditory cortex. Front. Neural Circuits; 9:22.

Mikaelian DO, Warfield D, and Norris O (1974). Genetic progressive hearing loss in the C57-b16 mouse. Relation of behavioral responses to chochlear anatomy. Acta Otolaryngol. 77, 327–334.

Moore AK and Wehr M. (2013). Parvalbumin-expressing inhibitory interneurons in auditory cortex are well-tuned for frequency. J. Neurosci. 33, 13713–13723.

O'Connell MN, Falchier A, McGinnis T, Schroeder CE, and Lakatos P. (2011). Dual mechanism of neuronal ensemble inhibition in primary auditory cortex. Neuron 69, 805–817.

Ozeki H, Finn IM, Schaffer ES, Miller KD, and Ferster D. (2009). Inhibitory stabilization of the cortical network underlies visual surround suppression. Neuron 62, 578–592.

Pelleg-Toiba R and Wollberg Z (1989). Tuning properties of auditory cortex cells in the awake squirrel monkey. Exp. Brain Res. 74, 353–364.

Pfeffer CK, Xue M, He M, Huang ZJ, and Scanziani M (2013). Inhibition of inhibition in visual cortex: the logic of connections between molecularly distinct interneurons. Nat. Neurosci. 16, 1068–1076.

Phillips DP and Cynader MS (1985). Some neural mechanisms in the cat's auditory cortex underlying sensitivity to combined tone and wide-spectrum noise stimuli. Hear. Res. 18, 87–102.

Poo C and Isaacson JS (2009). Odor representations in olfactory cortex: ''sparse'' coding, global inhibition, and oscillations. Neuron 62, 850–861.

Priebe NJ and Ferster D (2008). Inhibition, spike threshold, and stimulus selectivity in primary visual cortex. Neuron 57, 482–497.

Reinhold K, Lien AD, and Scanziani M (2015). Distinct recurrent versus afferent dynamics in cortical visual processing. Nat. Neurosci. 18, 1789–1797.

Rolls ET and Tovee MJ (1995). Sparseness of the neuronal representation of stimuli in the primate temporal visual cortex. J. Neurophysiol. 73, 713–726.

Rubin DB, Van Hooser SD, and Miller KD (2015). The stabilized supralinear network: a unifying circuit motif underlying multi-input integration in sensory cortex. Neuron 85, 402–417.

Rudy B, Fishell G, Lee S, and Hjerling-Leffler J (2011). Three groups of interneurons account for nearly 100% of neocortical GABAergic neurons. Dev. Neurobiol. 71, 45–61.

Sadagopan S and Wang X (2010). Contribution of inhibition to stimulus selectivity in primary auditory cortex of awake primates. J. Neurosci. 30, 7314–7325.

Sato TK, Haider B, Hausser M, and Carandini M (2016). An excitatory basis for divisive normalization in visual cortex. Nat. Neurosci. 19, 568–570.

Schneider DM, Nelson A, and Mooney R. (2014). A synaptic and circuit basis for corollary discharge in the auditory cortex. Nature 513, 189–194.

Scholl B, Gao X, and Wehr M (2010). Nonoverlapping sets of synapses drive on responses and off responses in auditory cortex. Neuron 65, 412–421.

Shamma SA and Symmes D (1985). Patterns of inhibition in auditory cortical cells in awake squirrel monkeys. Hear. Res. 19, 1–13.

Steriade M, Timofeev I, and Grenier F. (2001). Natural waking and sleep states: a view from inside neocortical neurons. J. Neurophysiol. 85, 1969–1985.

Strichartz GR (1973). The inhibition of sodium currents in myelinated nerve by quaternary derivatives of lidocaine. J. Gen. Physiol. 62, 37–57.

Sutter ML, Schreiner CE, McLean M, O'Connor KN, and Loftus WC (1999). Organization of inhibitory frequency receptive fields in cat primary auditory cortex. J. Neurophysiol. 82, 2358–2371.

Sutter ML and Loftus WC (2003). Excitatory and inhibitory intensity tuning in auditory cortex: evidence for multiple inhibitory mechanisms. J. Neurophysiol. 90, 2629–2647.

Talbot MJ and Sayer RJ (1996). Intracellular QX-314 inhibits calcium currents in hippocampal CA1 pyramidal neurons. J. Neurophysiol. 76, 2120–2124.

Tan AYY and Wehr M (2009). Balanced tone-evoked synaptic excitation and inhibition in mouse auditory cortex. Neuroscience 163, 1302–1315.

Tan AYY, Brown BD, Scholl B, Mohanty D, and Priebe NJ (2011). Orientation selectivity of synaptic input to neurons in mouse and cat primary visual cortex. J. Neurosci. 31, 12339–12350.

Tremblay R, Lee S, and Rudy B. (2016). GABAergic interneurons in the neocortex: from cellular properties to circuits. Neuron 91, 260–292.

Tsodyks MV, Skaggs WE, Sejnowski TJ, and McNaughton BL (1997). Paradoxical effects of external modulation of inhibitory interneurons. J. Neurosci. 17, 4382–4388.

Wehr M and Zador AM (2003). Balanced inhibition underlies tuning and sharpens spike timing in auditory cortex. Nature 426, 442–446.

Wehr M and Zador AM (2005). Synaptic mechanisms of forward suppression in rat auditory cortex. Neuron 47, 437–445.

Willmore B and Tolhurst DJ (2001). Characterizing the sparseness of neural codes. Network 12, 255–270.

Wu GK, Arbuckle R, Liu B-H, Tao HW, and Zhang LI (2008). Lateral sharpening of cortical frequency tuning by approximately balanced inhibition. Neuron 58, 132–143.

Xu X, Roby KD, and Callaway EM (2010). Immunochemical characterization of inhibitory mouse cortical neurons: three chemically distinct classes of inhibitory cells. J. Comp. Neurol. 518, 389–404.

Zhang LI, Tan AY, Schreiner CE, and Merzenich MM (2003). Topography and synaptic shaping of direction selectivity in primary auditory cortex. Nature 424, 201–205.

Zhang S, Xu M, Kamigaki T, Hoang Do JP, Chang W-C, Jenvay S, Miyamichi K, Luo L, and Dan Y (2014). Selective attention. Long-range and local circuits for top-down modulation of visual cortex processing. Science 345, 660–665.

Zhou M, Liang F, Xiong XR, Li L, Li H, Xiao Z, Tao HW, and Zhang LI (2014). Scaling down of balanced excitation and inhibition by active behavioral states in auditory cortex. Nat. Neurosci. 17, 841–850.

CHAPTER 2

Abstract

Changes in arousal influence cortical sensory representations, but the synaptic mechanisms underlying arousal-dependent modulation of cortical processing are unclear. Here we use two-photon Ca2+ imaging in auditory cortex of awake mice to show that heightened arousal, as indexed by pupil diameter, broadens frequency-tuned activity of layer 2/3 (L2/3) pyramidal cells. Sensory representations are less sparse and the tuning of nearby cells more similar when arousal increases. Despite the reduction in selectivity, frequency discrimination by cell ensembles improves due to a decrease in shared trial-to-trial variability. *In vivo* whole-cell recordings reveal that mechanisms contributing to the effects of arousal on sensory representations include state-dependent modulation of membrane potential dynamics, spontaneous firing, and tone-evoked synaptic potentials. Surprisingly, changes in short-latency, tone-evoked excitatory input cannot explain the effects of arousal on the broadness of frequency-tuned output. However, we show that arousal strongly modulates a slow, tone-evoked suppression of recurrent excitation underlying lateral inhibition [H.K. Kato, S.K. Asinof, J.S. Isaacson, Neuron, 95, 412-423, (2017)]. This arousal-dependent “network suppression” gates the duration of tone-evoked responses and regulates the broadness of frequency tuning. Thus, arousal can shape tuning via modulation of indirect changes in recurrent network activity.

Introduction

Information processing in sensory cortex is modulated by changes in behavioral states such as those associated with arousal, attention or task engagement (McGinley et al. 2015; Harris and Thiele 2011; Zagha and McCormick 2014; Lee and Dan 2012). Indeed, moment-to-moment changes in arousal have strong effects on spontaneous and stimulus-evoked firing activity in primary visual (V1) (Vinck et al. 2015; Ayaz et al. 2013; Bennett et al. 2013; Niell and Stryker 2010; Fu et al. 2014; Polack et al. 2013; Reimer et al. 2014; Mineault et al. 2016) and auditory (A1) cortex (Schneider et al. 2014; McGinley et al. 2015b; Zhou et al. 2014). Despite the potential for arousal to regulate cortical sensory coding, the subthreshold synaptic mechanisms by which changes in brain state influence sensory representations and tuning properties are not well understood. In recordings from head-fixed mice, changes in arousal are typically assessed by measurements of pupil diameter or exploratory behavior such as locomotion, with increases in pupil diameter and bouts of running/walking indicating heightened arousal (1). Interestingly, the transition from quiet wakefulness to locomotion has different effects in visual and auditory cortex: walking/running increases stimulus-driven firing in V1 (Vinck et al. 2015; Ayaz et al. 2013; Niell and Stryker 2010; Polack et al. 2013; Saleem et al. 2013) while it is associated with a decrease in sensory-evoked firing in A1 (Schneider et al. 2014; McGinley et al. 2015b; Zhou et al. 2014). However, heightened arousal does not require movement and recent work suggests that motor feedback signals to sensory cortex modulate activity differently than arousal tracked by pupillometry during quiet wakefulness (Vinck et al. 2015; Schneider et al. 2014).

Recently, our laboratory used pupillometry and Ca2+ imaging to study how fluctuations in arousal in the absence of locomotion modulate frequency coding in A1 of head-fixed mice (Figure 2.1). We showed that increases in arousal increased the tuning broadness of the majority of cells in A1 (Figure 2.1E2). These cells' tuning curves expanded asymmetrically; they became more receptive to higher-frequency tones (Figure 2.1F). However, despite a reduction in frequency selectivity, elevated arousal improves frequency discrimination by L2/3 pyramidal cells due to a decrease in noise correlations between cell pairs with increasing signal correlations (Figure 2.1G). Here, we use *in vivo* whole-cell current- and voltage-clamp recordings from L2/3 cells to reveal how changes in membrane potential dynamics and tone-evoked synaptic input contribute to this arousal-dependent modulation of frequency representations.

Figure 2.1 Summary of pupillometry/calcium imaging experiments. A. Experiment schematic. An IR camera records pupil diameter during imaging of GCaMP6-expressing neurons while tones are presented through an electrostatic speaker. Velocity is recorded using a low-resistance treadmill. **B.** Pupil diameter over the course of one imaging experiment **C.** Summary of pupil diameters over 8 experiments when mice are stationary (black) or walking/running (pink) shows that locomotion bouts were rare and only occurred during periods of high arousal. **D.** A representative cell showing enhancement of tone-evoked responses as pupil diameter increases. Bold traces, averaged responses. Grey traces, individual trials. **E1.** Arousal increases amplitude (filled circles) and reliability (open circles) (Friedman's ANOVA, both $p<0.001$). **E2.** Arousal increases the percentage of tones evoking a significant response (filled circles) and reduces lifetime sparseness (1-Sp, open circles) (Friedman's ANOVA, both $p<0.001$). **F.** Arousal broadens frequency tuning curves. Left, average response magnitude during low, moderate, and high (blue/green/red) arousal aligned to low arousal BF (Two-way ANOVA *p* arousal, *p* frequency, and *p* interaction all <0.001). Right, Low and high arousal curves scaled. Middle, cumulative probability plots show no shift in BF (1-35% [Constricted] vs. 66-100% [Dilated] max. diameter, Kolmogorov-Smirnov test, $p=0.94$). **G1.** Arousal differentially modulates signal correlations and noise correlations. **G2.** For all cell pairs in which signal correlations increase (n=3086), noise correlations decrease (Two-way ANOVA, *p* arousal, *p* correlations, *p* interactions all <0.001). **G3.** In the remaining pairs (n=1852) the opposite relationship can be observed (Two-way ANOVA, *p* arousal, *p* interactions <0.001, *p* correlations=0.066). **G4.** K nearest neighbor's classifier analysis reveals that arousal-dependent increases in decoding accuracy are due to changes in noise correlations; the classifier performed better with an unshuffled dataset (i.e. with intact noise correlations). Two-way ANOVA *p* arousal and *p* dataset both <0.001, *p* interaction=0.127. Open circles, classifier performance on data shuffled to remove noise correlations. Filled circles, classifier performance on unshuffled data. Dotted line, chance-level performance.

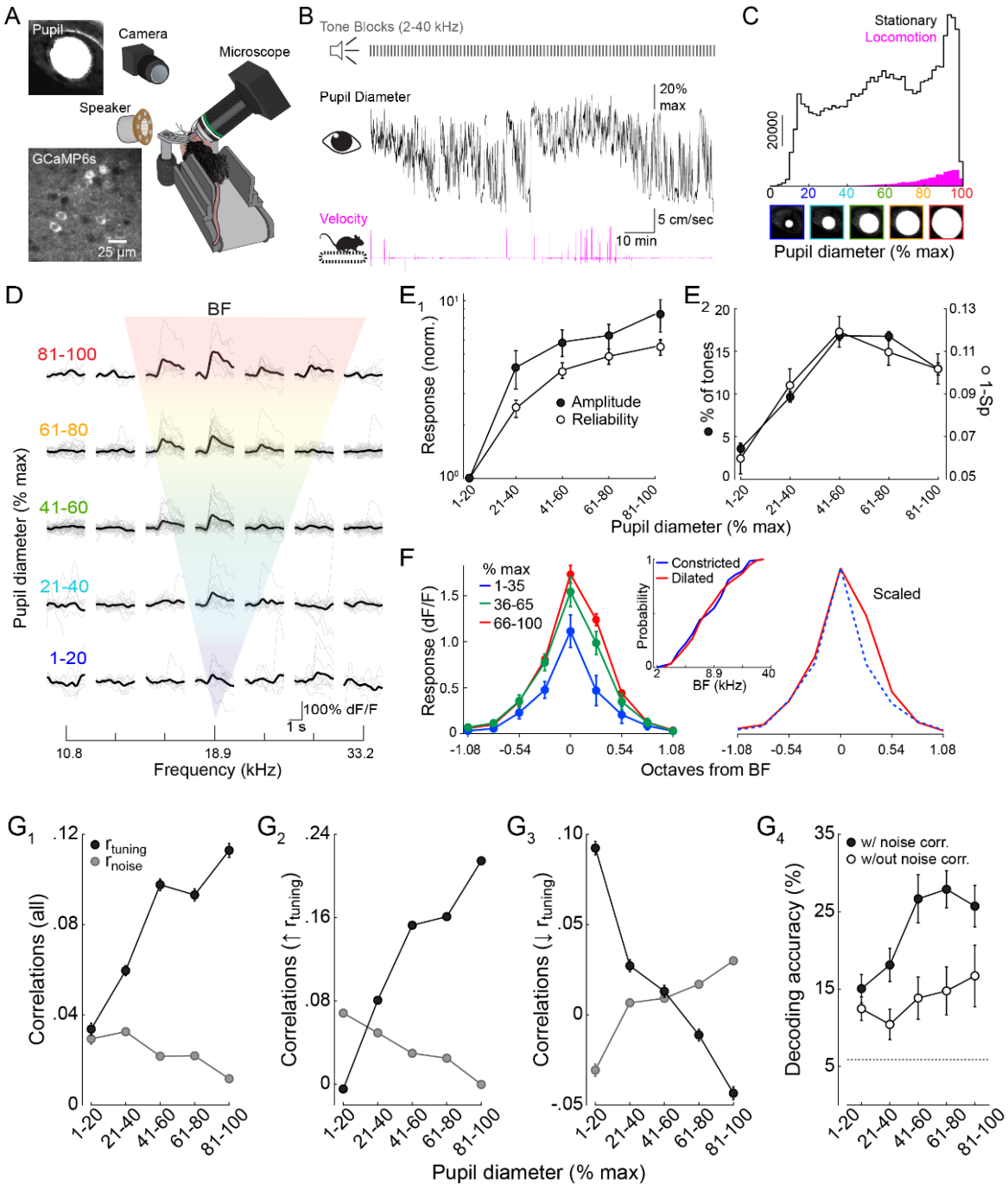
A
Pupil
Camera
Microscope
Speaker
GCaMP6s
25 µm
B
Tone Blocks (2-40 kHz)
Pupil Diameter
20% max
Velocity
5 cm/sec
10 min
C
Stationary
Locomotion
20000
0 20 40 60 80 100
Pupil diameter (% max)
D
BF
81-100
61-80
41-60
21-40
1-20
Pupil diameter (% max)
100% dF/F
1 s
10.8 18.9 33.2
Frequency (kHz)
E1
Response (norm.)
Amplitude
Reliability
1-20 21-40 41-60 61-80 81-100
Pupil diameter (% max)
E2
% of tones
1-Sp
F
% max
1-35
36-65
66-100
Response (dF/F)
Constricted
Dilated
Probability
BF (kHz)
Scaled
-1.08 -0.54 0 0.54 1.08
Octaves from BF
G1
Correlations (all)
r tuning
r noise
G2
Correlations (↑ r tuning)
G3
Correlations (↓ r tuning)
G4
Decoding accuracy (%)
w/ noise corr.
w/out noise corr.
Pupil diameter (% max)

Results

We used whole-cell recordings to measure how arousal impacts subthreshold activity in L2/3 cells. Studies in many cortical areas indicate that spontaneous membrane potential (Vm) dynamics are influenced by brain state (reviewed in McGinley et al. 2015a). Indeed, during low to moderate arousal, current clamp recordings revealed large-amplitude, low frequency (2-10 Hz) Vm fluctuations that were attenuated at high levels of arousal (Figure 2.2A). Both Vm standard deviation and low-frequency oscillations (2–10 Hz power) diminished during high arousal (n=10, Friedman's ANOVA, p =0.025 and 0.020, respectively, Figure 2.2C), consistent with previous studies tracking locomotion or pupil diameter in V1 and A1 (Bennett et al. 2013; Niell and Stryker 2010; Polack et al. 2013; Reimer et al. 2014; McGinley et al. 2015b). Similar to deep layer neurons in A1 (McGinley et al. 2015b), mean Vm was slightly more hyperpolarized during moderate arousal (n=26, Friedman's ANOVA, p=0.019, Figure 2.2B). Despite the similarity in mean Vm during the lowest and highest levels of arousal, the rate of spontaneous spiking steadily declined as arousal increased (n=18, 7 whole-cell and 11 cell-attached recordings, Friedman's ANOVA, p =0.005, 14/18 cells had a significant negative relationship between pupil diameter and spiking, Figure 2.2D,E). How do these changes in cortical state affect the firing rate of non-pyramidal cells? We used 2-photon targeted cell-attached recordings alongside pupillometry to record spontaneous spiking from three defined interneuron subtypes: the parvalbumin-positive (PV) cells, the somatostatin-positive (SOM) cells and the vasoactive intestinal polypeptide-positive (VIP) cells (Figure 2.3). None of the cells in the first two groups had significant positive linear relationships between arousal and spontaneous spike rate and the majority of

cells in both groups (4/4 PV cells and 6/10 SOM cells) had significant negative relationships. In contrast, 4/8 VIP cells had a negative relationship with pupil diameter and 2/8 had a positive relationship. Together, these findings are consistent with the idea that low arousal is associated with high Vm variability and slow, synchronized cortical activity while high arousal enforces low variability, suppression of slow rhythms and fewer spontaneous spikes across the cortical network (McGinley et al. 2015a; Vinck et al. 2015; Bennett et al. 2013; Zhou et al. 2014).

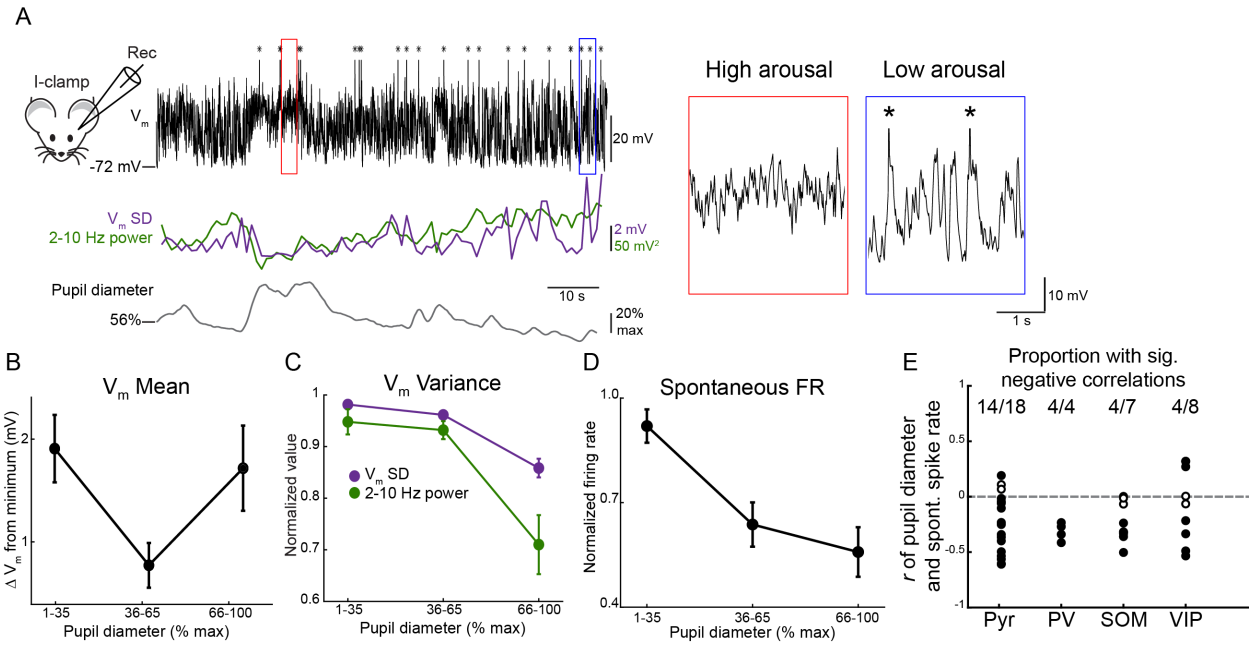

Figure 2.2 Elevated arousal reduces membrane potential variability and spontaneous firing A. Left, current-clamp recording of membrane potential in a representative L2/3 cell. Asterisks mark truncated action potentials. Underneath the voltage trace, membrane potential standard deviation (purple) and 2-10 Hz power (green) are plotted in 1 s bins. Bottom, pupil diameter. Right, expansion of boxed areas. **B.** Summary showing that mean membrane potential is most hyperpolarized at intermediate levels of arousal (n=30 cells). **C.** As arousal increases, 2-10 Hz power and membrane potential standard deviation decrease. **D.** Summary showing that spontaneous firing rate decreases with increasing arousal. **E.** Most pyramidal cells, PV cells, SOM cells and VIP cells have a negative relationship with pupil diameter. "Pyr" column is the same data as in D. Filled circles, cells with significant Pearson's correlation (p<0.05) between pupil diameter and spike rate.

In agreement with recent work characterizing lateral inhibition in A1 (Kato et al. 2017), tones (100- 200 ms) at “preferred” frequencies evoked short-latency excitatory postsynaptic potentials (EPSPs) while distal (“non-preferred”) frequencies evoked a slow hyperpolarization (Figure 2.3A). Interestingly, the time course of responses to preferred tones was arousal-dependent. Averaging responses during low arousal revealed that the short latency EPSP was curtailed by membrane hyperpolarization (Figure 2.3A). During higher arousal, although the early amplitude of the EPSP slightly increased, the EPSP duration was markedly prolonged. For responses at non-preferred frequencies, the tone-evoked hyperpolarization was strongly suppressed as arousal increased (Figure 2.3A). Given the small change in the early EPSP, the most parsimonious explanation for the increased duration of preferred responses is the suppression of the overlapping slow hyperpolarization.

We quantified arousal-dependent changes in tone-evoked responses across cells by aligning responses to each cells’ BF (Figure 2.3B). On average, increases in arousal were associated with modest increases in EPSP peak amplitude (n = 15, two-way ANOVA, p frequency<0.001, p arousal=0.033, p interaction=0.994, Figure 2.3B). However, arousal had a strong effect on the response integral and duration of tone-evoked EPSPs. During low arousal, tone-evoked hyperpolarization was most prominent during BF tones (frequencies with the strongest early EPSP) and those of higher frequencies. As arousal increased, suppression of the slow hyperpolarization shifted the integrated responses from net hyperpolarization to net depolarization (two-way ANOVA, p frequency=0.458, p arousal<0.001, p interaction=0.943, Fig, 2.3B) and EPSP duration was prolonged (two-way ANOVA, p frequency=0.303, p arousal<0.001,

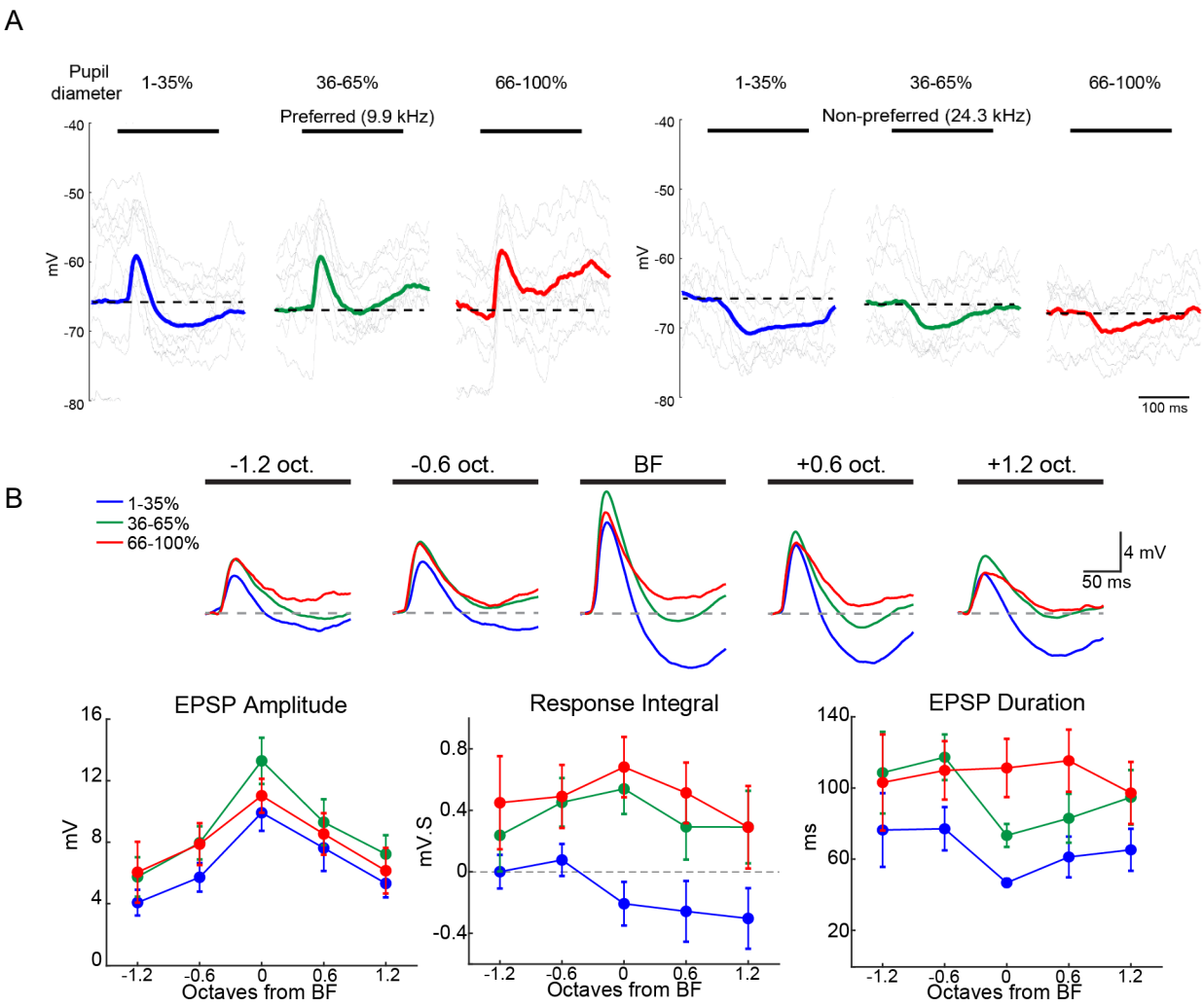

Figure 2.3 Elevated arousal increases response magnitude by reducing lateral inhibition. A. Responses to a preferred (left) and non-preferred (right) tone (black bar) during different arousal levels in a representative cell. Gray traces, subset of single trials. Bold traces, mean responses. Dashed line, baseline Vm. **B.** Top, average responses to tones aligned to best frequency of each cell during low (blue) moderate (green) and high (red) arousal (n=15 cells). Dashed line, baseline Vm. Bottom left, arousal causes a modest increase in peak amplitude. Bottom middle, responses shift from net hyperpolarization to net depolarization at frequencies >=BF with increases in arousal. Bottom right, arousal-dependent suppression of lateral inhibition increases EPSP duration.

p interaction=0.806, Figure 2.3B). Interestingly, the differences in response integral and EPSP duration between low and high arousal were largest for frequencies ≥BF (Figure 2.3B). Together, these results indicate that arousal can regulate response strength by reducing a form of lateral inhibition that limits the duration of tone-evoked synaptic excitation.

What accounts for the arousal-dependent changes in tone-evoked synaptic potentials? To address this question, we used voltage-clamp to isolate excitatory postsynaptic currents (EPSCs) in L2/3 cells (Vhold = -70 mV, near the reversal potential for inhibition set by our internal solution). Under resting conditions, cells received high-frequency barrages of spontaneous EPSCs (Figure 2.6). On individual trials, preferred tones evoked transient EPSCs locked to tone onset (ON response). During low arousal, transient ON responses were immediately followed by a sustained suppression of spontaneous EPSCs. When trials were averaged, this resulted in a slow outward current (relative to baseline). We have recently shown (Kato et al. 2017) that this reflects a reduction in ongoing recurrent activity, “network suppression (NS)”, underlying an unconventional form of lateral inhibition that shapes frequency tuning. Indeed, during low arousal, NS was strongest at non-preferred frequencies (Figure 2.6). Thus, the slow tone-evoked hyperpolarization in current clamp recordings is due to a suppression of recurrent excitation rather than direct synaptic inhibition (Kato et al. 2017). Intriguingly, while early ON responses were only slightly modulated, NS was strongly attenuated when arousal increased (Figure 2.6). This loss of NS led to an increase in duration of ON responses (Figure 2.6). These results suggest that NS limits the strength of tone-evoked excitation in an arousal-dependent manner.

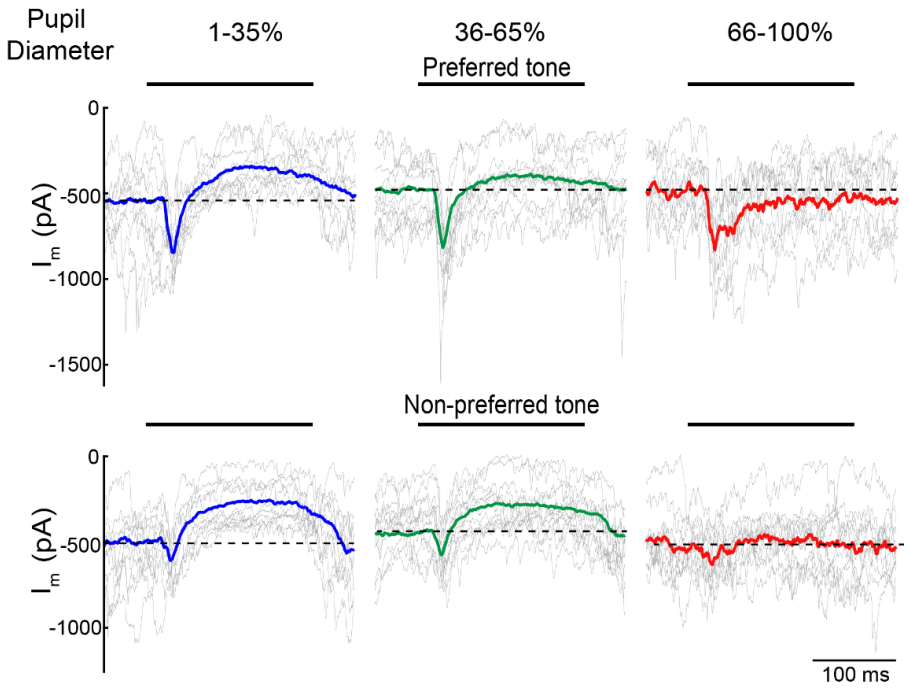

Figure 2.4 Arousal modulates network suppression. EPSCs from one cell in response to a preferred (top) and a non-preferred (bottom) tone at different levels of arousal. Grey traces, subset of single trials. Bold traces, average. Dashed lines, baseline holding current.

One explanation for the arousal-dependent attenuation of NS is that elevated arousal itself suppresses spontaneous excitation. In other words, during high arousal there might be less synaptic input to suppress. We thus examined the relationship between arousal and spontaneous activity. Consistent with membrane voltage recordings, barrages of large amplitude EPSCs during low arousal became desynchronized when arousal increased (Figure 2.6). Although this led to a marked change in current variability (Friedman's ANOVA, $p<0.001$), total current (mean Im) remained constant (Friedman's ANOVA, $p=0.223$, n = 14 cells, Figure 2.6). Thus, while excitatory input was more variable on a moment-to-moment basis during low arousal, the net amount of ongoing synaptic excitation remained the same as arousal increased. This indicates that arousal-dependent changes in NS cannot be due to changes in the available amount of recurrent excitation.

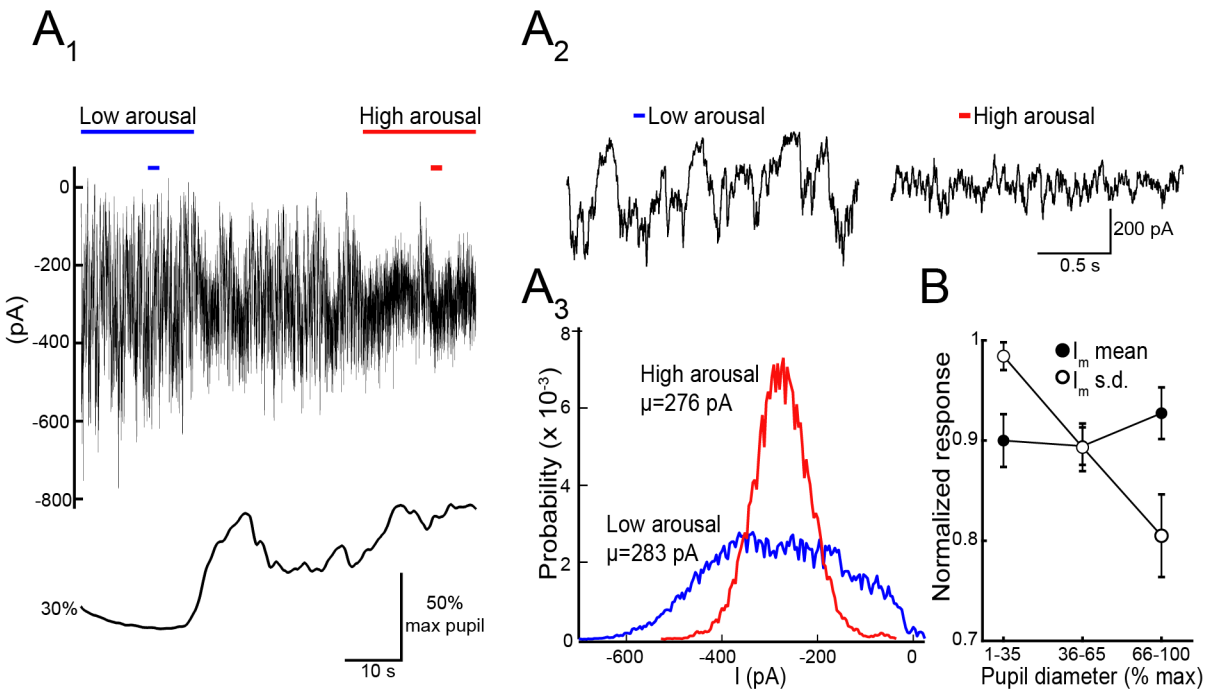

Figure 2.5 The loss of network suppression is not due to diminished spontaneous excitation. A1. Current (holding potential=-70 mV) and pupil diameter from one cell show a decrease in current variability at high levels of arousal **A2.** Expansion of periods marked by small bars in A1. **A3.** All-points histogram (20 s) of current from high and low arousal epochs in A1. **B.** Increases in arousal decrease current variability, while mean holding current remains unchanged (n=14).

Previously, we showed that mouse A1 behaves as an inhibition-stabilized network (ISN) and hypothesized that this property might be critical for NS lateral inhibition. Could the cortex be switching between "ISN-like" and "non-ISN-like" states as arousal fluctuates? ISNs are among a series of "balanced" models of circuit function in which recurrent excitation is so strong that local inhibition is required to stabilize the firing rates of pyramidal cells. One theoretical prediction of ISN-like behavior in a circuit is that suppression of local inhibitory cells would produce a paradoxical increase in their

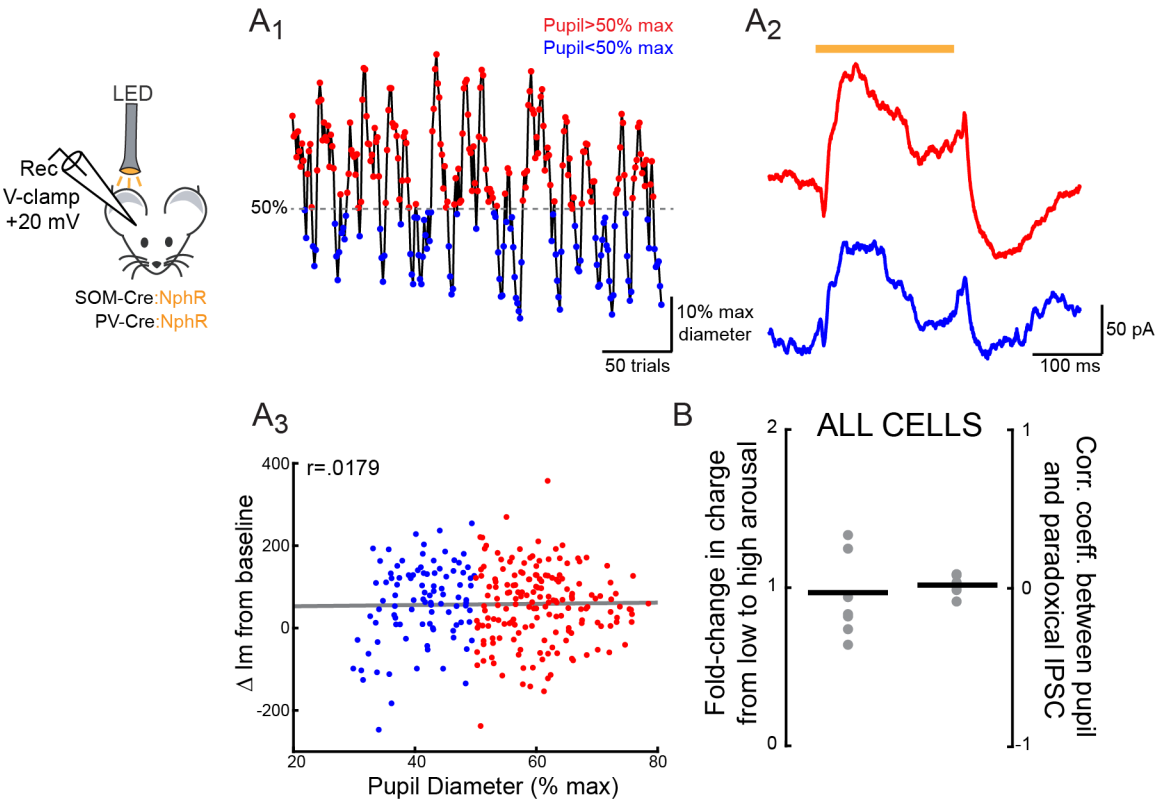

Figure 2.6 The cortex behaves as an inhibition-stabilized network at all levels of arousal A. Optogenetic suppression of PV or SOM cells with halorhodopsin (NphR) produces a paradoxical increase in inhibition. **A1,** Pupil trace from one experiment in a mouse in which PV cells express NphR. Circles represent each inactivation trial. They are colored red or blue depending on whether the pupil diameter was greater than or less than 50% of its maximum. **A2,** mean change in holding current across all high arousal or low arousal trials shown in A1. **A3,** Strength of the paradoxical IPSC in each trial, measured as the mean change in Im during inactivation. When plotted as a function of pupil diameter, it is apparent that it is not influenced by changes in arousal. **B.** No change in paradoxical inhibition across all trials for each recorded cell (n=5 PV cells and 2 SOM cells, pooled). Left, fold-change in inhibitory charge from low to high arousal. Right, correlation between pupil diameter and mean IPSC (as in A3) for each cell.

firing rate and an increase in synaptic inhibition into local pyramidal cells. We recorded IPSCs onto L2/3 pyramidal cells and tested whether the optogenetic suppression of either PV cells (n=5) or SOM cells (n=2) evoked a paradoxical increase in inhibition while measuring changes in arousal with pupillometry (Figure 2.6A). Inactivation of

either interneuron population produced a paradoxical IPSC, but it was equally strong at all levels of arousal (Figure 2.6A,B). The charge of this response did not differ between responses recorded at pupil diameters below 50% and responses recorded above 50% of maximum pupil diameter (Student's *t*-test, p=0.7859), and none of the recorded cells demonstrated significant linear relationships between pupil diameter and changes in holding current during each trial (all Pearson's Correlation p values >0.182; Student's *t*-test between all Pearson's r values and zero p=0.3905) (Figure 2.6B).

Given that inhibitory interneurons are highly interconnected with recurrent excitatory circuits, changes in NS should also impact tone-evoked synaptic inhibition (Kato et al. 2017). We thus compared the effect of arousal on tone-evoked EPSCs (Vhold = -70 mV) and inhibitory postsynaptic currents (IPSCs, Vhold = +20 mV, near the reversal potential for excitation) in the same cells (n = 12). Tone-evoked NS of IPSCs mirrored suppression of EPSCs (Figure 2.7A1). Moreover, arousal-dependent changes in the strength of tone-evoked excitation and inhibition (total charge below and above baseline, respectively) scaled such that the relative balance of excitation/inhibition remained constant (1.38- and 1.40-fold change from low to high arousal for IPSQs and EPSQs, respectively, p=0.010 for IPSQ low vs. high and p= 0.048 for EPSQ low arousal vs. high arousal, Figure 2.7A2).

How do these large arousal-dependent changes in network suppression modulate the tuning of tone-evoked excitation? Overall, short-latency ON responses were largest during moderate arousal (n = 16 cells, Figure 2.7B2, paired t test p<0.003 for low arousal vs. moderate arousal and for moderate arousal vs. high arousal). However, changes in arousal did not have an obvious impact on ON response tuning

(two-way ANOVA, p frequency<0.001, p arousal=0.236, p interaction=0.585, Figure 2.7B1). In contrast, increases in arousal led to a stronger, monotonic attenuation of tone-evoked network suppression (Figure 2.7C1, two-way ANOVA, p frequency, p arousal<0.002, p interaction=0.539, Figure 2.7C2, paired t-test all p <0.001). Furthermore, the arousal-dependent change in NS appeared tuned to frequencies ≥ BF (Figure 2.7C1). This reflects the fact that NS itself is biased to high frequencies (Kato et al. 2017). Together, these results indicate that while arousal weakly modulates short-latency excitation, it has a strong impact on tone-evoked responses via regulation of an indirect form of inhibition that gates recurrent excitation.

Figure 2.7 Arousal-dependent changes in network suppression underlie the broadening of EPSC tuning. A. Arousal modulates EPSCs and IPSCs similarly. **A1**. Averaged tone-evoked EPSCs and IPSCs from the same cell during different levels of arousal. Horizontal dashed lines, baseline holding current. Vertical dashed lines, measurement windows of ON and NS response magnitudes. **A2**. Absolute charge above/below baseline for IPSCs/EPSCs during different arousal levels (n=35 tone responses at each arousal level from 12 cells). **B1**. Normalized ON responses aligned to BF (n=16 cells). **B2**. Summary of all significant ON responses recorded at each arousal level shows that ON response magnitude increased from low to moderate arousal, then decreased from moderate to high arousal (n=32 frequencies from 16 cells). **C1**. Normalized NS responses aligned to BF shows that NS is biased to high frequencies and decreases with increasing arousal (n=16). **C2**. Summary of significant NS responses recorded at each level of arousal shows that NS decreases monotonically (n=27 frequencies from 11 cells). Error bars, SEM.

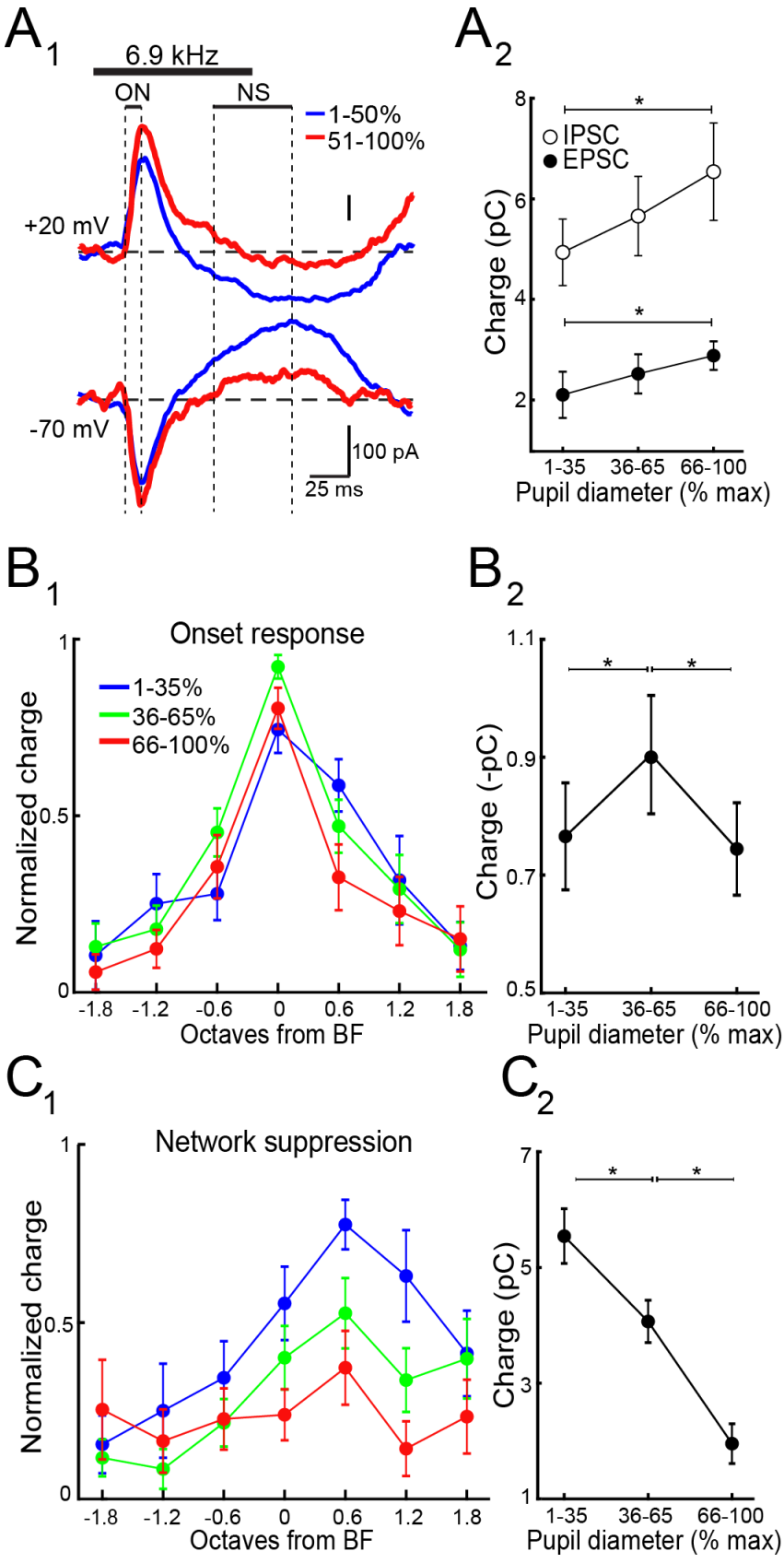
A1
6.9 kHz
ON
NS
1-50%
51-100%
+20 mV
-70 mV
100 pA
25 ms
A2
IPSC
EPSC
Charge (pC)
Pupil diameter (% max)
1-35
36-65
66-100
B1
Onset response
1-35%
36-65%
66-100%
Normalized charge
Octaves from BF
B2
Charge (-pC)
Pupil diameter (% max)
C1
Network suppression
Normalized charge
Octaves from BF
C2
Charge (pC)
Pupil diameter (% max)

Discussion

Previous work in our lab used pupillometry and Ca2+ imaging in stationary mice to investigate arousal-related changes in frequency-tuned activity in A1. Imaging activity evoked by pure tones in L2/3 pyramidal cells revealed that arousal-dependent increases in response amplitude and reliability decreased the sparseness of cortical tone representations. Consistent with these changes, signal correlations increased with arousal indicating greater overlap in the frequency tuning curves of cells across the cortical population. Despite this increase in tuning similarity, elevated arousal improved frequency discrimination by cell ensembles due to a reduction in noise correlations (shared trial-to-trial variability).

Using whole-cell current-clamp and voltage-clamp recordings in awake mice, we investigated the synaptic mechanisms underlying the changes described above. Similar to previous studies (McGinley et al. 2015a; Bennett et al. 2013; Reimer et al. 2014; McGinley et al. 2015b), increases in arousal caused a shift in spontaneous synaptic activity: slow (2-10 Hz) bursts of excitatory input gave way to steady, desynchronized input. Slow oscillations in spontaneous activity can be correlated between nearby cells as well as across wide areas of sensory cortex (Arroyo et al. 2018). Therefore, we think it likely that the arousal-dependent shift in membrane dynamics is largely responsible for the reduction in noise correlations underlying improved frequency discrimination.

Increases in arousal were associated with a reduction in frequency of spontaneous action potentials, raising the possibility that the changes in sensory representations we observed simply reflect an enhanced signal-to-noise-ratio (SNR). Indeed, the arousal-dependent increase in response strength and reliability as well as

the reduction in sparseness could be due to an improved SNR. However, increases in arousal also broadened frequency tuning curves of individual cells due to a stronger enhancement of frequencies >BF. Thus, while changes in SNR are likely to contribute to modulation of cortical tone representations, SNR alone cannot explain the effects of arousal on frequency tuning.

We used current and voltage clamp recordings to examine how arousal-dependent changes in tone-evoked subthreshold activity could modulate tuning properties. Interestingly, conventional short-latency tone-evoked synaptic excitation was affected by arousal in a nonmonotonic fashion. Transitions from low to moderate arousal led to a modest increase in the strength of short latency evoked EPSCs, however, response strength subsequently declined during high arousal. Activity evoked by complex sounds in deep layers of A1 is similarly found to be maximal during moderate arousal (McGinley et al. 2015b). Nonetheless, the small arousal-related increases in conventional, short-latency synaptic input seem insufficient to account for the strong changes in activity observed with Ca2+ imaging.

We show here and in recent work in awake mice (Kato et al. 2017) that non-preferred tones can evoke a hyperpolarizing response due to a slow suppression of ongoing, recurrent synaptic excitation. This “network suppression” relies on cortical somatostatin-expressing interneurons and provides an unconventional form of lateral inhibition (Kato et al. 2017). Recent work in V1 indicates that surround suppression also reflects a reduction in total network input due to somatostatin interneurons (Adesnik 2017). Here we show that NS is strongest during low arousal and becomes progressively weaker as arousal increases. Furthermore, the arousal-dependent loss of

NS at preferred frequencies leads to an increase in duration of tone-evoked responses. Intriguingly, NS occurs preferentially for tones above the BF (Kato et al. 2017). Although the reasons for this asymmetry are yet to be established, the net effect of the strong reduction in NS by arousal is a preferential change in synaptic responses to high frequency tones. This asymmetry in NS is likely to account for why increases in arousal broaden frequency tuned L2/3 cell output with a high frequency bias.

Materials and Methods

Animal care and surgical preparation

Animal care: Mice were housed with a 12:12 hour reversed light cycle. Experiments were performed during the dark period. All procedures were in accordance with protocols approved by the UCSD Institutional Animal Care and Use Committee and guidelines of the National Institute of Health.

Surgical preparation: Mice were anesthetized with isoflurane and received dexamethasone (2 mg/kg, i.m.). A custom head-bar was glued to the skull, muscle overlying right auditory cortex was removed, and intrinsic signal imaging was used to functionally map the location of A1. Mice received baytril (10 mg/kg) and buprenorphine (0.1 mg/kg) before returning to their home cages.

Preparation for electrophysiology: Mice were habituated to sitting quietly while head-fixed for 2-3 days (15 minutes to 2 hrs/day). Once the mice were successfully habituated (i.e. had a wide range of pupil diameters during their final final habituation

session), they were anaesthetized with isoflurane and the skull above A1 was thinned using a drill. During thinning, the skull was flushed with cold artificial cerebrospinal fluid (aCSF, (in mM) 142 NaCl, 5 KCl, 10 Glucose, 10 HEPES, 3.1 CaCl2, 1.3 MgCl2, pH 7.4, 310 mOsm). After thinning, mice received dexamethasone (2 mg/kg) and recovered in their home cage for >2 hours. Immediately prior to recording, a well filled with aCSF was constructed around the recording site, a small (<0.3 mm) craniotomy was made in the thinned skull, and the dura removed.

Preparation for two-photon imaging: Mice were anesthetized with isoflurane and received dexamethasone (2 mg/kg, i.m.). A custom head bar was glued to the skull, muscle overlying the right auditory cortex was removed, and a craniotomy (~2 × 3 mm) was performed over the auditory cortex, leaving the dura intact. A glass window was placed over the craniotomy and secured with dental acrylic. Mice received baytril (10 mg/kg) and buprenorphine (0.1 mg/kg) before returning to their home cages. Mice were habituated to sitting quietly while head fixed for 2–7 d (2 h/day) before imaging.

Pupillometry

The eye contralateral to A1 was monitored via a camera (BFLY-U3-05S2M-CS, Point Grey). An IR LED was used to visualize the pupil in the presence of weak ambient illumination (473 nm). Pupil measurements and velocity were acquired using open-source software (Bonsai, http:/bonsai-rx.org). Pupil diameter values were smoothed using a moving average filter (1 s). Pure tones were delivered via calibrated free-field speaker (ES1, TDT) directed to the ear contralateral to A1. Tones were generated by

software (BControl; http://brodylab.org) running on MATLAB (MathWorks) communicating with a real-time system (RTLinux).

Whole-cell recording

Recordings were made using the blind technique (Margrie et al. 2002). Current-clamp recordings used pipettes filled with internal solution containing (in mM) 130 Kgluconate, 5 NaCl, 10 HEPES, 12 Na-phosphocreatine, 0.2 EGTA, 3 Mg-ATP and 0.2 Na-GTP (pH 7.2, 305 mOsm). Voltage-clamp recordings used pipettes filled with (in mM) 130 Cs-gluconate, 10 HEPES, 5 TEA-Cl, 12 Na-phosphocreatine, 0.2 EGTA, 3 Mg-ATP, and 0.2 Na-GTP (pH 7.2, 310 mOsm). Series resistance (Rs<50 MOhms) was continuously monitored for stability. Recording depth (226±11.3 μm from pia, n=31) was determined from the micromanipulator z-axis readout (MP285, Sutter Inst.). Recordings were made with a Multiclamp 700A (Molecular Devices), digitized at 5-20 kHz, and acquired using AxoGraph X. Potentials were not corrected for liquid junction potential (~15 mV). Responses were sorted by pupil diameter during the tone (1-35%, 36-65%, and 66-100%), averaged (≥5 trials) for each frequency and baselined to tone onset. Cells were rejected if no onset response was >30 pA or >2 mV (voltage and current clamp, respectively). For current clamp recordings, integral and peak amplitude were measured 10-200 ms post-tone onset. EPSP duration was measured at 25% of peak. BF was the frequency with the largest EPSP onset slope. In voltage-clamp, ON response was measured as charge in a window 20-30 ms post-tone onset. NS was calculated as charge below baseline 75-125 ms post-tone onset. Excitatory Im was measured relative to the most positive current value during each recording. Excitatory

(Inhibitory) charge above baseline was calculated as the charge 10-100 ms post-tone onset which was below (above) baseline holding current. EPSC BF was determined from the peak amplitude of the response within 50 ms of tone onset. Cell responsiveness was determined with a Wilcoxon signed-rank test (alpha=0.01).

Two-photon targeted recordings

A ~2 mm circular craniotomy was performed over right A1 and surrounding cortex and a semicircular coverslip with half of that area was adhered to the cortical surface, covering A1. Pipettes filled with aCSF containing Alexa-488 were lowered into A1 though the uncovered part of the craniotomy under the guidance of a commercial two-photon microscope (BScope, ThorLabs). Alexa-488 and tdTomato were excited at 950 nm (Mai Tai, Newport). tdTomato-expressing cells were recorded juxtacellularly with a MultiClamp 700B (Molecular Devices) in voltage-clamp configuration, digitized at 20 kHz (ITC-18, Instrutech), and acquired using Axograph X (Axograph). Traces were band-pass filtered (50-4000 Hz) to remove drifting baseline and high-frequency noise. Capacitive currents associated with recorded cells were many-fold stronger than the background noise (which was <=25 pA), and were detected using an amplitude threshold. Pupil diameters were recorded concurrently using an IR camera trained on the mouse's eye, which was back-filled with scattered laser light.

Interneuron inactivation

Interneuron inactivation experiments were performed on SOM-IRES-Cre and PV-IRES-Cre mice (age >P60) which were injected with the virus AAV9-FLEX-NphR3.0-

EYFP prior to P2. Physiological recordings were performed as described above. A 590 nm LED (ThorLabs) was used to shine amber light over the craniotomy in 200 ms-long pulses.

In Vivo Two-Photon Ca^{2+} Imaging

Imaging was performed within 2 to 3 weeks of window implantation. Imaging fields were within A1 determined from intrinsic signal imaging. GCaMP6s was excited at 950 nm (Mai Tai, Newport), and images (512 × 512 pixels covering ~500 × 500 μm) were acquired at 28.4 Hz with a 16× objective (Nikon) using a commercial microscope (B-scope, Thorlabs) and ScanImage4. Images were acquired 120–250 μm below the dura, and lateral motion was corrected using a phase correlation algorithm (https://github.com/cortex-lab/Suite2P).

Imaging Analysis

Responses were classified as significant if $P < 0.005$ (Wilcoxon rank sum test) for >85% of trial-pooled timepoints over any continuous 0.5 s window during the 1 s tone, compared to a trial-pooled 1 s period preceding the tone. Cells were responsive if responses to, at least, 2 tones in, at least, 2 of 5 arousal levels (bin size 20% from 0 to 100% pupil max) were significant. Response strength was measured as the dF/F integral of the mean response of each cell during each arousal state, normalized to low arousal (1–20% pupil max). Reliability was measured as the mean pairwise trial-by-trial Pearson's correlation coefficient of responses during each arousal state.

Total correlations (sum of signal and noise correlations) were quantified using a trial-by-trial response vector (dF/F integral during the tone**)** for each arousal level for each cell. To calculate r_{signal}, the temporal order of each cell's responses to repeated presentations of each tone were shuffled, abolishing noise correlations while maintaining trial-by-trial stimulus identity. Total and signal correlations were obtained by calculating Pearson's correlation coefficients for the unshuffled and shuffled response vectors, respectively, of cell pairs from the same experiment. A noise correlation value for each cell pair from each experiment was obtained by subtracting their signal correlation value from their total correlation value. To determine if arousal modulates r_{noise} in a r_{signal}-related manner, mean noise correlations were calculated separately for cell pairs with signal correlations that increased (slope > 0) or decreased (slope < 0) with arousal.

For the nonlinear classifier, a population response matrix was created from the trial-by-trial responses for all cells of each experiment. The response matrices for a subset of randomly selected trials (75% of total) were used to train a K-nearest neighbors' classifier (k = 10 trials; standardized Euclidean distance metric) before testing the performance of the classifier on the remaining 25% of trials (100 iterations).

Chapter 2 contains material previously published in: Lin PA, Asinof SK, Edwards NJ, Isaacson JS (2019). Arousal regulates frequency tuning in primary auditory cortex. *PNAS*; 116(50):25304-25310. The dissertation author was a co-author of this paper.

References

Adesnik H (2017). Synaptic Mechanisms of Feature Coding in the Visual Cortex of Awake Mice. Neuron; 95(5):1147-1159.

Arroyo S, Bennett C, Hestrin S (2018). Correlation of Synaptic Inputs in the Visual Cortex of Awake, Behaving Mice. Neuron; 99(6):1289-1301.

Ayaz A, Saleem AB, Schölvinck ML, Carandini M (2013). Locomotion controls spatial integration in mouse visual cortex. Curr Biol.; 23(10):890-4.

Bennett C, Arroyo S, Hestrin S (2013). Subthreshold mechanisms underlying state-dependent modulation of visual responses. Neuron; 80(2):350-7.

Fu Y, Tucciarone JM, Espinosa JS, Sheng N, Darcy DP, Nicoll RA, Huang ZJ, Stryker MP (2014). A cortical circuit for gain control by behavioral state. Cell;156(6):1139-1152.

Harris KD, Thiele A (2011). Cortical state and attention. Nat Rev Neurosci. 2011 Aug 10;12(9):509-23.

Kato HK, Asinof SK, Isaacson JS (2017). Network-Level Control of Frequency Tuning in Auditory Cortex. Neuron;95(2):412-423.

Lee S-H and Dan Y (2012). Neuromodulation of brain states. Neuron; 76(1):209-22.

Margrie TW, Brecht M, Sakmann B (2002). In vivo, low-resistance, whole-cell recordings from neurons in the anaesthetized and awake mammalian brain. Pflugers Arch.;444(4):491-8.

McGinley MJ, Vinck M, Reimer J, Batista-Brito R, Zagha E, Cadwell CR, Tolias AS, Cardin JA, McCormick DA (2015). Waking State: Rapid Variations Modulate Neural and Behavioral Responses. Neuron; 87(6):1143-1161.

McGinley MJ, David SV, McCormick DA (2015). Cortical Membrane Potential Signature of Optimal States for Sensory Signal Detection. Neuron; 87(1):179-92.

Mineault PJ, Tring E, Trachtenberg JT, Ringach DL (2016). Enhanced Spatial Resolution During Locomotion and Heightened Attention in Mouse Primary Visual Cortex. J Neurosci.; 36(24):6382-92.

Niell CM, Stryker MP (2010). Modulation of visual responses by behavioral state in mouse visual cortex. Neuron; 65(4):472-9.

Polack PO, Friedman J, Golshani P (2013). Cellular mechanisms of brain state-dependent gain modulation in visual cortex. Nat Neurosci.; 16(9):1331-9.

Reimer J, Froudarakis E, Cadwell CR, Yatsenko D, Denfield GH, Tolias AS (2014). Pupil fluctuations track fast switching of cortical states during quiet wakefulness. Neuron; 84(2):355-62.

Saleem AB, Ayaz A, Jeffery KJ, Harris KD, Carandini M (2013). Integration of visual motion and locomotion in mouse visual cortex. Nat Neurosci.; 16(12):1864-9.

Schneider DM, Nelson A, Mooney R (2014). A synaptic and circuit basis for corollary discharge in the auditory cortex. Nature; 513(7517):189-94.

Vinck M, Batista-Brito R, Knoblich U, Cardin JA (2015). Arousal and locomotion make distinct contributions to cortical activity patterns and visual encoding. Neuron; 86(3):740-54.

Zagha E, McCormick DA (2014). Neural control of brain state. Curr Opin Neurobiol.; 29:178-86.

Zhou M, Liang F, Xiong XR, Li L, Li H, Xiao Z, Tao HW, Zhang LI (2014). Scaling down of balanced excitation and inhibition by active behavioral states in auditory cortex. Nat Neurosci.; 17(6):841-50.

CHAPTER 3

Introduction

All primary sensory cortices in the mammalian brain are bilateral structures with two instances partitioned between the two hemispheres, reciprocally connected to one another by excitatory projections. Each cortex is largely responsible for processing sensory inputs originating in the contralateral hemifield. Callosal projections between cortices permit each hemisphere to receive information about the ipsilateral hemifield. In the visual system, where primary sensory cortices are only a few synapses from the peripheral sensory organ, these callosal inputs are thought to be critical for processes which require the reconciliation of input from both hemifields such as binocular fusion and depth calculations (Hubel and Weisel 1962; Hubel and Weisel 1967; Choudhury et al. 1965; Payne et al. 1984; Gardner and Cynader 1987; Scholl et al. 2013).

In contrast callosal projections in A1 are neither the initial nor the secondary locus for hemifield integration. Indeed, neurons in cat inferior colliculus are binaurally tuned (Kuwada et al. 1997; Benevento and Coleman 1970). A1 is separated from its corresponding peripheral sensory organ, the cochlea, by many synaptically connected relays, each of which are themselves bilaterally symmetric structures which are reciprocally connected via cross-hemispheric projections (Brown and Santos-Sacchi 2013). Hemifield integration in the ascending auditory system is necessary for computing sound location by comparing small differences in the intensity and timing of the noises between ears (Brown and Santos-Sacchi 2013; Middlebrooks 2015). While projections between auditory cortices might perform a similar function, it is unlikely that they are better suited than their counterparts in the ascending auditory system. These

inter-aural computations require exquisite spike precision (Brand et al. 2002) which might not be feasible with the jitter of cortical auditory responses and the long conduction delays associated with transcallosal projections between two structures on opposite sides of the brain.

While it may not serve the same purpose as cross-hemispheric projections in the ascending auditory system, evidence for the importance of this callosal pathway comes from human studies. Some patients with tinnitus or stuttering have abnormally-sized corpora callosa (Diesch et al. 2012; Choo et al. 2012). Patients who have experienced surgical removal of the callosum, callosal agenesis, or removal of A1 from one hemisphere have all impaired performance on sound lateralization tasks (Hausmann et al. 2005). In older subjects, callosal tract size has been shown to correlate with performance on a dichotic listening task (Gootjes et al. 2006).

Anatomical studies in rats and cats have shown that callosal axons projecting between auditory cortices mostly originate from excitatory layer 3 and 5 pyramidal cells, have areal specificity (i.e. A1 projects to A1, A2 projects to A2, etc.) and are coarsely homotypic (Code and Winer 1985; Ruttgers et al. 1990). Recent observations in mice also suggested that a subset of callosal fibers actually originate from inhibitory parvalbumin-positive neurons (Zurita et al. 2018).

Much less is known about the functional properties of this callosal projection, and there is some debate about whether the net effects of callosal inputs are excitatory or inhibitory (Bloom and Hynd 2005). Even a purely excitatory projection might produce net feedforward inhibition if it had stronger contacts onto interneurons than pyramidal cells contralaterally. One recent investigation used *ex vivo* recordings to determine that,

because of their synaptic connectivity, callosal inputs had net excitatory and net inhibitory inputs onto two different kinds of projection neurons in layer V of mouse A1 (Rock and Apicella 2015).

Are the effects of contralateral inputs heterogenous *in vivo*? Do they produce net facilitation or suppression of neural activity? A handful of studies have examined the effects of activating or inactivating callosal projections in anesthetized cats and ferrets. In the ferret, electrical stimulation of the callosum produced both a facilitation in spiking activity in some cells and a long-lasting suppression (>100 ms in duration) in others; a third population exhibited both effects (Kitzes and Doherty 1994). In the anesthetized cat, electrical stimulation of one cortex or the corpus callosum produced short-latency EPSPs (sometimes followed by IPSPs) in cells recorded on the contralateral side (Mitani and Shimokouchi 1985). Another set of recent studies used cooling loops to unilaterally inactivate auditory fields in anesthetized cats (Carrasco and Lomber 2013; Carrasco et al. 2015). In this work, inactivation of A1 sharply reduced sound-evoked spiking activity suggesting that callosal projections have a mostly excitatory influence.

In order to further understand the functional import of these callosal projections in the awake mouse brain, our lab adopted an optogenetic inactivation approach. We expressed the light-sensitive cation channel channelrhodopsin-2 (ChR2) in inhibitory neurons in left A1, then recorded from individual neurons in right A1 using the blind patch technique (Boyden et al. 2005; Margrie et al. 2002). We measured the effects of contralateral inactivation on membrane potential and synaptic currents and discovered that the resulting changes were not stereotyped. Contralateral inactivation did not diminish membrane potential standard deviation in the same manner as a sound

stimulus, and the high variability of this manipulation meant that the mean effects of inactivation required many trials (>50) to become apparent. Individual cells responded to contralateral inactivation through hyperpolarization, depolarization, or a mixture of the two. Some of these differences depended on the population of inhibitory neurons in which ChR2 was expressed. Finally, we measured the changes in excitatory and inhibitory synaptic inputs evoked by contralateral inactivation. While inhibition always declined in response to inactivation, excitation decreased in some cells and increased in others.

Results

Using the blind patch technique in awake head-fixed mice, we measured membrane potential (Vm) in neurons (n=33) throughout right A1 while intermittently inactivating left A1. Inactivation was performed via high-frequency (80 Hz) stimulation of ChR2 expressed virally in inhibitory interneurons in left A1 (see methods). We performed experiments using two different cre lines in order to confine expression of ChR2 to inhibitory interneurons: PV-cre (in which the opsin is expressed in parvalbumin-positive interneurons, which provide strong perisomatic inhibition to pyramidal cells) and Gad2-IRES-cre (in which all GABA-synthesizing cells in the contralateral cortex would express the opsin, including PV cells) (Hippenmeyer et al. 2005; Taniguchi et al. 2011). We analyzed the impact of inactivation by calculating a mean trace across all recorded cells aligned to stimulus onset. This mean trace (Figure 1b) suggested that inactivation produced an initial hyperpolarization followed by a slow, long-latency depolarization.

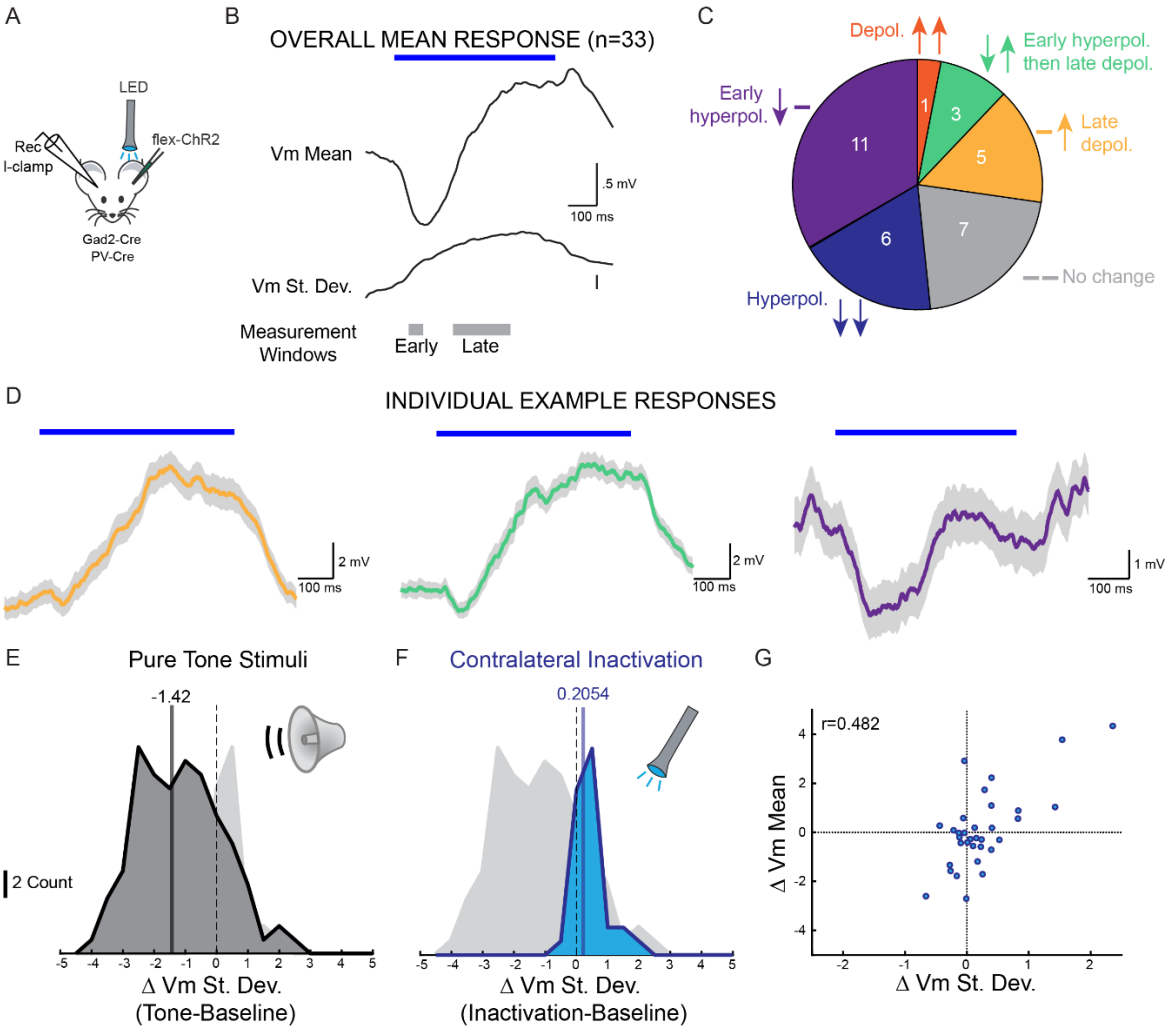

Figure 3.1. Contralateral inactivation in the awake mouse brain. **A.** experimental schematic. **B.** Top, average of mean traces from responses to contralateral inactivation in 33 neurons. Middle, average of Vm standard deviation traces from the same cells. Bottom, measurement windows for C. **C.** Classification of response types according to when they deviated from baseline (see windows in B). **D.** Individual examples of responses to inactivation. Mean traces are colored according to C. **E.** Distribution of tone-evoked changes in trial-by-trial Vm standard deviation relative to baseline (n=15 previously recorded cells). Data from F is plotted in grey. **F.** Distribution of contralateral inactivation-evoked changes in trial-by-trial variability (n=33 cells, this dataset). Data from E is plotted in grey. For E and F, bold lines represent median values of the distribution. **G.** Scatterplot of change in Vm mean vs. change in Vm standard deviation for each cell in this dataset.

Since each inactivating pulse train was identical both between trials within each recorded cell and across cells within each animal in which a recording was performed

(and, absent major differences in expression between animals, the effects of inactivation should be functionally similar from animal to animal) we hypothesized that we would find consistent responses from trial to trial, from cell to cell, and from mouse to mouse. Instead we observed considerable response variability at each of these levels of analysis (Figure 3.1).

Within the same experiment, we recorded from individual cells which had distinct mean responses to inactivation (Figure 3.1C,D). We developed a classification system for sorting these different responses based on whether those changes in membrane potential were significantly different from baseline ($p<0.05$, Wilcoxon Sign-Rank test) during two time periods (Figure 3.1B, bottom): shortly (50-100 ms) after LED onset and at the latter part of the pulse train (200-400 ms after onset). Of the nine possible results this procedure could produce (increase/decrease/no change at each of those two time points), we observed cells with six types of Vm responses (Figure 3.1C): no significant change, early hyperpolarization, sustained hyperpolarization, early hyperpolarization followed by a slow depolarization, long-latency depolarization, and a short-latency depolarization which persisted until the end of the inactivation. Examples from several of these categories are depicted in Figure 3.1D. Recordings from a non-opsin expressing mouse in which the pulse train was presented over the craniotomy (in right A1) or bilaterally in front of both eyes failed to evoke any change in Vm (data not shown).

It has been demonstrated that cells in the neocortex of many species respond to relevant sensory inputs with decreases in trial-to-trial Vm variability, even in the absence of a change in mean Vm (Churchland et al. 2010). Using current-clamp

recordings from 15 tone-sensitive neurons previously described in Chapter 2, we confirmed that pure tone stimuli diminished trial-to-trial Vm standard deviation relative to baseline (Figure 3.1E, Wilcoxon Sign-Rank Test relative to baseline period $p<0.0001$). In contrast, contralateral inactivation actually increased Vm standard deviation (Figure 3.1B, 3.1F, Wilcoxon Sign-Rank Test $p=0.023$). Across all experiments, there was a significant relationship between each cell's mean change in Vm and its mean change in standard deviation (Figure 3.1G, $r=0.482$ $p=0.0045$). While the magnitude of this correlation was partially driven by a population of cells which responded to inactivation with large long-latency depolarizations, the majority of cells which hyperpolarized during inactivation also exhibited larger trial-to-trial variance during contralateral inactivation (Figure 3.1G).

Are there differences between each of the mice in our experiments which might explain some of the cell-to-cell variance in response properties? When we sorted these data according to the cre line in which each experiment was performed and then recomputed mean traces, we noticed a clear pattern: activation of contralateral PV-positive interneurons hyperpolarized the recorded cell, while activation of all inhibitory interneuron types (using the Gad2-IRES-cre line) produced a short-latency hyperpolarization followed by a strong depolarization on average (Figure 3.2B,C). The majority of cells recorded in Gad2-IRES-cre mice were net-depolarized by inactivation while the majority of cells recorded in PV-cre mice were hyperpolarized by inactivation (Figure 3.2C). Curiously, similar proportions of cells from both genotypes exhibited a mean increase in Vm standard deviation (11/18 cells from PV mice and 9/15 cells from Gad mice). We performed histology in order to determine whether differences in ChR2

expression might underlie the distinction between our cre lines. In Gad2-IRES-cre mice, EYFP expression was saturating and spanned the entire rostral-caudal axis of A1. In contrast, EYFP expression in PV-cre mice was patchy, possibly due to incomplete expression or to virally-induced cell death. Typical examples of the observed expression patterns are shown in Figure 3.2D.

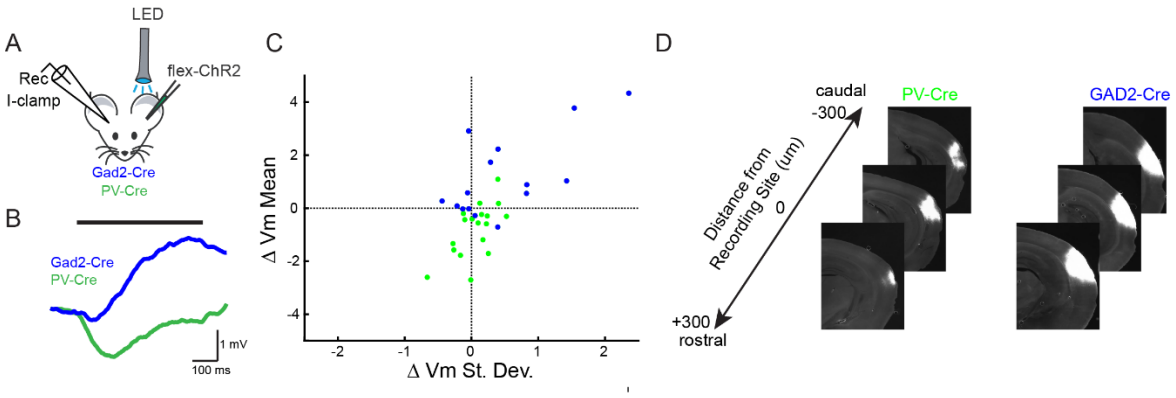

Figure 3.2 Expression strategies dictate the effects of contralateral inactivation. **A.** experimental schematic. **B.** average of all mean Vm responses from neurons recorded in Gad2-cre (n=15, blue) and neurons recorded in PV-Cre (n=18, green) mice. **C.** Scatterplot from 1G, recolored to reflect mouse genotype. **D.** Example images of left A1 from representative PV-Cre and Gad2-Cre mice. ChR2-EYFP is well expressed in Gad2-cre mice, but not in PV-Cre mice.

We elected to examine our recordings from Gad2-cre mice in more detail since opsin expression was very consistent from mouse to mouse. These recordings contained representatives of five of the six response categories described above; the one response type which was only observed in PV-cre mice was sustained hyperpolarization (Figure 3.3B). While there was diversity in response types, the responses tended to follow the kinetics suggested by the mean inactivation traces (Figures 3.1B, 3.2B: significant hyperpolarization only occurred shortly after the pulse train began, and (with the exception of only one cell) significant depolarization always occurred more than 100 ms after the onset of the pulse train (Figure 3.3C).

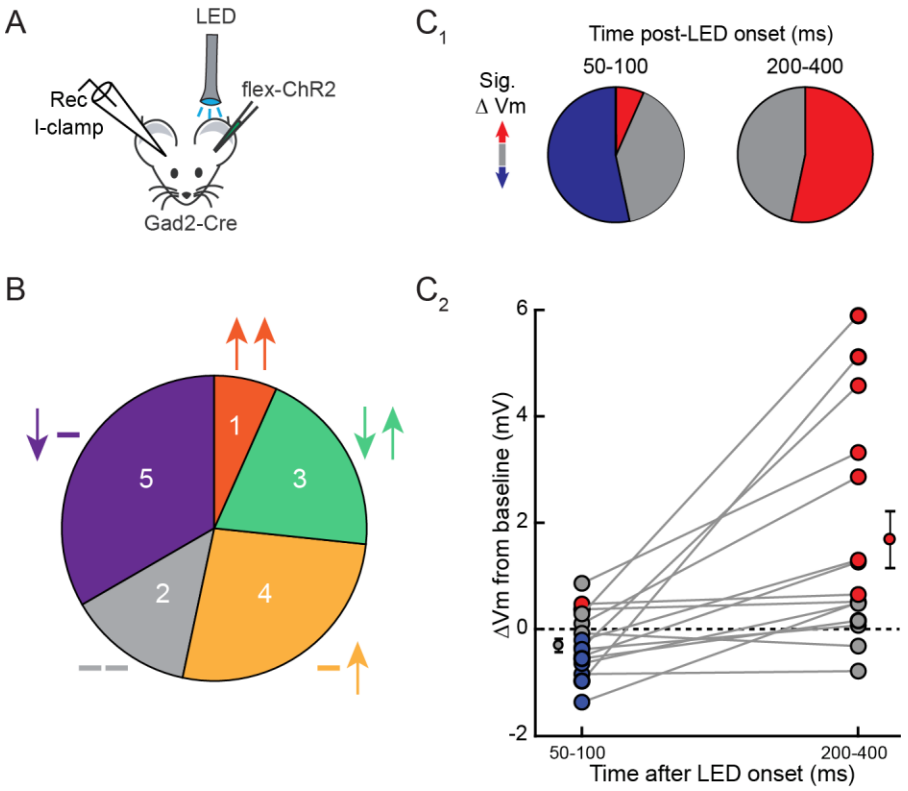

Figure 3.3 Contralateral inactivation produces a biphasic response in Gad2-cre mice. A. Experimental schematic **B.** Proportions of inactivation responses recorded in Gad2-cre mice. **C.** Contralateral inactivation in Gad2-cre mice produces two distinct responses, with partial overlap. C1 left, 50-100 ms after LED onset, the majority of cells hyperpolarize significantly. Right, the majority of cells depolarize relative to baseline 200-400 ms after LED onset. C2, mean change in Vm during both windows for all recorded cells. Data points are filled blue or red if they significantly deviate from baseline (p<0.05, Wilcoxon Signed-Rank test). Overall averages (mean ± SEM) are plotted on the outside.

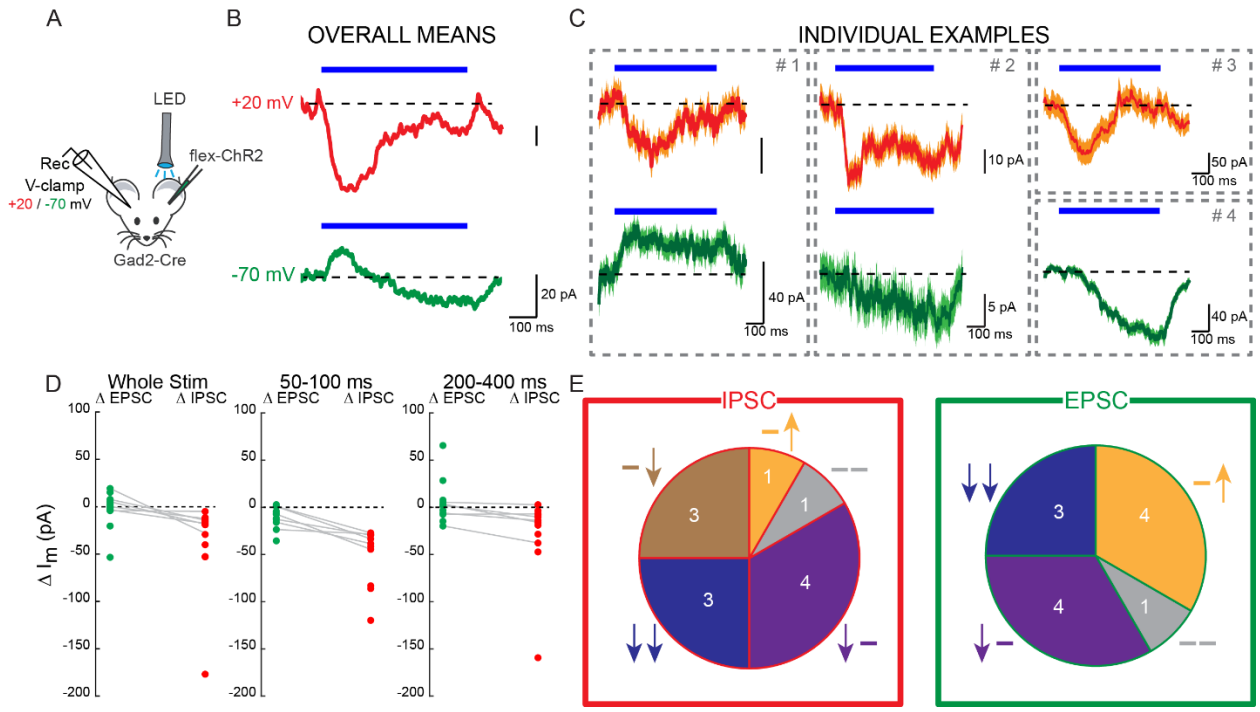

Figure 3.4 Effects of contralateral inactivation on synaptic excitation and inhibition. A. Experimental schematic. Voltage clamp recordings were performed at +20 mV to isolate IPSCs and -70 mV to isolate EPSCs. **B.** Top, overall averages of n=12 recordings of IPSCs in response to contralateral inactivation. Bottom, overall averages of n=12 recordings of EPSCs in response to contralateral inactivation. Both EPSCs and IPSCs were recorded for n=6 cells. **C.** Individual examples of excitatory and inhibitory currents during contralateral inactivation. In some recordings, EPSC and IPSC kinetics are well-matched (see Example #1), while in others they differ greatly (see Example #2). **D.** Change in holding current during (left) the entire LED pulse train (middle) 50-100 ms after onset and (right) 200-400 ms after onset. Delta EPSC sign has been reversed, so positive values reflect an increase in inward currents. Cells with matching measurements are connected by a grey line. **E.** Proportions of response types for IPSCs (left) and EPSCs (right) according to the criteria outlined in 3.1C.

How do excitatory and inhibitory synaptic currents generate these Vm responses? We performed voltage clamp recordings to measure synaptic excitation and inhibition into cells in layers 2 and 3 in Gad2-IRES-cre mice expressing ChR2 in left A1. Excitatory current responses had kinetics which resembled the inactivation-induced changes in Vm described above (Figure 3.4B,C). In 7/12 recordings, EPSCs were reduced 50-100 ms after onset and in a non-overlapping group (3/12 recordings), EPSCs increased significantly 200-400 ms after onset (Figure 3.4E). Surprisingly, inactivation did not always produce parallel modulation of excitatory and inhibitory inputs. For the majority (10/12) of the recordings, inhibitory currents diminished during contralateral inactivation either early or late after LED onset (Figure 3.4E). In 3 of the 6 cases in which EPSCs and IPSCs were recorded in the same cell, average EPSCs during the LED exceeded baseline while average IPSCs dropped below baseline (Figure 3.4C example #2, 4D see grey lines).

Discussion

Here, we used an optogenetic inactivation strategy to measure the functional contributions of callosal projections to Vm in neurons within right A1. We uncovered a surprising amount of variability in how each cell responded to the inactivation both across trials and between recordings, even those in performed on the same day in the same mouse.

Some of this variability could be explained by the cre line used in the experiment, which influenced how many cells in the contralateral cortex expressed ChR2 and presumably impacted the spatial extent of the inactivation. It is unclear why injection of

the same virus (at an identical titer and with similar post-injection expression times) would cause either sparse expression and cell death or excellent expression with no apparent cell death in mice from two different cre lines. We caution other researchers to replicate their optogenetic manipulations using multiple cre lines and viral serotypes in case these methodological variables might influence their experimental outcomes.

When we focused our analysis on the 15 current-clamp recordings which were performed in Gad2-IRES-cre animals (and which had the best and most uniform expression), we discovered that the recorded cells still exhibited many different kinds of responses. These mean responses could largely be decomposed into two partially-overlapping groups representing two patterns of activity: a short-latency hyperpolarization and a longer-latency depolarization.

Rapid hyperpolarization in response to the pulse train could have been caused either by decreased input from excitatory callosal projections or by the activation of contralaterally-projecting inhibitory neurons (Zurita et al. 2018). However in our voltage-clamp recordings we only observed decreases in synaptic input within the first 100 ms of the inactivation suggesting that this hyperpolarization is not caused by the activation of callosal inhibitory projections.

Despite the high mouse-to-mouse variability in ChR2 expression, almost all of the cells recorded in PV-cre mice either hyperpolarized in response to inactivation (12/18 cells) or were unaffected (5/18 cells). Since the hyperpolarization was caused by a decrease in callosal excitatory input, we hypothesize that the affected cells received projections from a segment of the contralateral cortex which was inactivated and the

unaffected cells only received projections from contralateral regions where activity was not optogenetically reduced.

What caused the slow depolarization hundreds of milliseconds after inactivation began? We mostly observed this response in Gad2-cre mice, which had robust ChR2 expression throughout contralateral A1. We hypothesize that this results from the simultaneous removal of excitatory callosal input across a large range of the tonotopic axis, diminishing local inhibition and leading to a large but variable burst of excitatory activity.

Why does contralateral inactivation decrease net inhibition into L2/3 cells in right A1? Parvalbumin-positive interneurons in layer 5 receive strong excitation from callosal projections (Rock and Apicella 2015; Slater and Isaacson, unpublished data), suggesting that their firing rate might be controlled by input from the other cortex. Consistent with this, extracellular recordings show that fast-spiking cells in deeper layers show a sharp reduction in action potential firing during contralateral inactivation, while fast-spiking units in superficial layers appear to spike significantly more 250-500 ms after the pulse train onset (Slater and Isaacson, unpublished data). The inhibitory inputs I recorded in the voltage clamp recordings described in this chapter are presumably a sum of the outputs of L2/3 and deeper-layer interneurons. The fact that I never observed a net increase in inhibition in the latter half of the pulse train might suggest that, in A1, L2/3 pyramidal cells receive strong inhibitory inputs from cells in deeper layers (relative to V1 or S1, see Katzel et al. 2011).

These data solidify the suggestion that A1-A1 callosal inputs are primarily excitatory and homotypic. Despite this homogeneity, inactivation of this projection

produces heterogenous effects in target cells. This effect variability likely arises from differences in synaptic connectivity from the inactivated contralateral area onto the recorded cells and nearby interneurons.

Materials and Methods

Animal care

Mice were housed with a 12:12 hour reversed light cycle. Experiments were performed during the dark period. All procedures were in accordance with protocols approved by the UCSD Institutional Animal Care and Use Committee and guidelines of the National Institute of Health. All mice were either Gad2-IRES-cre (Taniguchi et al. 2011) or PV-cre (Hippenmeyer et al. 2005)

Surgical preparation

Mice were anesthetized with isoflurane and received dexamethasone (2 mg/kg, i.m.). Intrinsic signal imaging was used to functionally map the location of A1 in the left hemisphere. A series of three craniotomies were performed over left A1, and virus (AAV9::pCMV:FLEX-ChR2-EYFP) was injected at two depths (250 and 500 um deep, 50 nL per injection). Craniotomies were covered over and the skin above the skull was sutured. Mice received baytril (10 mg/kg) and buprenorphine (0.1 mg/kg) before returning to their home cages.

3-4 weeks later, a custom head-bar was glued to the skull, muscle overlying right auditory cortex was removed, and intrinsic signal imaging was used to functionally map

the location of right A1. Left A1 was covered with cyanoacrylate to improve light transmission through the skull.

1-3 days later, the mice were anaesthetized with isoflurane and the skull above A1 was thinned using a drill. During thinning, the skull was flushed with cold artificial cerebrospinal fluid (aCSF, (in mM) 142 NaCl, 5 KCl, 10 Glucose, 10 HEPES, 3.1 CaCl2, 1.3 MgCl2, pH 7.4, 310 mOsm). After thinning, mice received dexamethasone (2 mg/kg) and recovered in their home cage for at least 1 hour. Immediately prior to recording, a well filled with aCSF was constructed around the recording site, a small (<0.3 mm) craniotomy was made in the thinned skull, and the dura removed.

For a subset of the recordings (n=4), red retrobeads were injected into the craniotomy after recording had finished (2 injections, 100 nl each, 500 and 250 um deep). In all of these cases, we were able to confirm the homotypic alignment of the recording site and contralateral ChR2 expression.

Whole-cell recording

Recordings were made using the blind technique (Margrie et al. 2002). Voltage-clamp recordings used pipettes filled with (in mM) 130 Cs-gluconate, 10 HEPES, 5 TEA-Cl, 12 Na-phosphocreatine, 0.2 EGTA, 3 Mg-ATP, and 0.2 Na-GTP (pH 7.2, 310 mOsm). Series resistance was continuously monitored for stability. Current-clamp recordings used pipettes filled with internal solution containing (in mM) 130 K-gluconate, 5 NaCl, 10 HEPES, 12 Na-phosphocreatine, 0.2 EGTA, 3 Mg-ATP and 0.2 Na-GTP (pH 7.2, 305 mOsm). A subset of current-clamp recordings (n=3) were conducted instead with the Cs-gluconate internal solution described above. Recording depth was

determined from the micromanipulator z-axis readout (MP285, Sutter Instruments). Recordings were made with a Multiclamp 700A (Molecular Devices), digitized at 5-10 kHz, and acquired using AxoGraph X. Potentials were not corrected for liquid junction potential (~15 mV).

During recordings, an LED (ThorLabs) was used to produce 480 nm light delivered in 80 Hz pulse trains (440-560 ms in duration) over left A1. Dark cloth and a silicone elastomer mixed with iron oxide were used to limit light transmission from the tip of the fiber.

Data analysis

Only neurons in which >50 inactivation trials were recorded were used for analysis. Mean Im and Vm were computed (1) from 50-100 ms and (2) from 200-400 ms after LED onset and contrasted with baseline values (computed in the 10 ms before LED onset). For each cell, Vm standard deviation across all trials was computed for each point during the pulse train then averaged across time.

Histology

Mice euthanized with a high dose of isoflurane and then transcardially perfused with ice-cold phosphate-buffered saline (PBS) then PBS containing 4% paraformaldehyde (PFA). Brains were removed and post-fixed in the PFA solution. After 24 hours, brains were transferred to a PBS solution with 30% sucrose until they sank. Sectioning (100 um sections) was performed on a freezing microtome. After

sections were mounted, EYFP fluorescence in A1 was examined using a Keyence fluorescence microscope.

Chapter 3 contains material which is being prepared for submission for publication. The dissertation author will be a coauthor on this paper with Drs. Bernard Slater and Jeffry Isaacson.

References

Benevento LA, Coleman PD. Responses of single cells in cat inferior colliculus to binaural click stimuli: combinations of intensity levels, time differences and intensity differences. Brain Res.; 17(3):387-405.

Bloom JS, Hynd GW (2005). The role of the corpus callosum in interhemispheric transfer of information: excitation or inhibition? Neuropsychol Rev.; 15(2):59-71.

Boyden ES, Zhang F, Bamberg E, Nagel G, Deisseroth K (2005). Millisecond-timescale, genetically targeted optical control of neural activity. Nat Neurosci.; 8(9):1263-8.

Brand A, Behrend O, Marquardt T, McAlpine D, Grothe B (2002). Precise inhibition is essential for microsecond interaural time difference coding. Nature; 417(6888):543-7.

Brown MC, Santos-Sacchi J (2013). 'Audition', in Squire LR, Berg D, Bloom FE, duLac S, Ghosh A, Spitzer NC *Fundamental Neuroscience, 4th edition*. Waltham, MA: Academic Press, pp.553-576.

Carrasco A, Lomber SG (2013). Influence of inter-field communication on neuronal response synchrony across auditory cortex.Hear Res.; 304:57-69.

Carrasco A, Kok MA, Lomber SG (2015). Effects of core auditory cortex deactivation on neuronal response to simple and complex acoustic signals in the contralateral anterior auditory field. Cereb Cortex.; 25(1):84-96.

Choo AL, Kraft SJ, Olivero W, Ambrose NG, Sharma H, Chang SE, Loucks TM (2011). Corpus callosum differences associated with persistent stuttering in adults. J Commun Disord.; 44(4):470-7.

Choudhury BP, Whitteridge D, Wilson ME (1965). The function of the callosal connections of the visual cortex. Q J Exp Physiol Cogn Med Sci.;50:214-9.

Churchland MM, Yu BM, Cunningham JP, Sugrue LP, Cohen MR, Corrado GS, Newsome WT, Clark AM, Hosseini P, Scott BB, Bradley DC, Smith MA, Kohn A, Movshon JA, Armstrong KM, Moore T, Chang SW, Snyder LH, Lisberger SG, Priebe NJ, Finn IM, Ferster D, Ryu SI, Santhanam G, Sahani M, Shenoy KV (2010). Stimulus onset quenches neural variability: a widespread cortical phenomenon. Nat Neurosci.;13(3):369-78.

Code RA, Winer JA (1985). Commissural neurons in layer III of cat primary auditory cortex (AI): pyramidal and non-pyramidal cell input. J Comp Neurol.; 242(4):485-510.

Diesch E, Schummer V, Kramer M, Rupp A (2012). Structural changes of the corpus callosum in tinnitus. Front Syst Neurosci.;6:17.

Gardner JC, Cynader MS (1987). Mechanisms for binocular depth sensitivity along the vertical meridian of the visual field.Brain Res.; 413(1):60-74.

Gootjes L, Bouma A, Van Strien JW, Van Schijndel R, Barkhof F, Scheltens P (2006). Corpus callosum size correlates with asymmetric performance on a dichotic listening task in healthy aging but not in Alzheimer's disease. Neuropsychologia; 44(2):208-17.

Hausmann M, Corballis MC, Fabri M, Paggi A, Lewald J (2005). Sound lateralization in subjects with callosotomy, callosal agenesis, or hemispherectomy. Brain Res Cogn Brain Res.;25(2):537-46.

Hippenmeyer S, Vrieseling E, Sigrist M, Portmann T, Laengle C, Ladle DR, Arber S (2005). A developmental switch in the response of DRG neurons to ETS transcription factor signaling. PLoS Biol. 2005 May;3(5):e159.

Hubel DH, Wiesel TN (1962). Receptive fields, binocular interaction and functional architecture in the cat's visual cortex. J Physiol.; 160:106-54.

Hubel DH, Wiesel TN (1967). Cortical and callosal connections concerned with the vertical meridian of visual fields in the cat. J Neurophysiol.; 30(6):1561-73.

Kätzel D, Zemelman BV, Buetfering C, Wölfel M, Miesenböck G (2011). The columnar and laminar organization of inhibitory connections to neocortical excitatory cells. Nat Neurosci; 14(1):100-7.

Kitzes LM, Doherty D (1994). Influence of callosal activity on units in the auditory cortex of ferret (Mustela putorius). J Neurophysiol.; 71(5):1740-51.

Kuwada S, Batra R, Yin TC, Oliver DL, Haberly LB, Stanford TR (1997). Intracellular recordings in response to monaural and binaural stimulation of neurons in the inferior colliculus of the cat. J Neurosci.;17(19):7565-81.

Margrie TW, Brecht M, Sakmann B (2002). In vivo, low-resistance, whole-cell recordings from neurons in the anaesthetized and awake mammalian brain. Pflugers Arch. 444, 491–498.

Middlebrooks JC (2015). Sound localization. Handb Clin Neurol ;129:99-116.

Mitani A, Shimokouchi M (1985). Neuronal connections in the primary auditory cortex: an electrophysiological study in the cat. J Comp Neurol.; 235(4):417-29.

Payne BR, Pearson HE, Berman N (1984). Role of corpus callosum in functional organization of cat striate cortex. J Neurophysiol.; 52(3):570-94.

Rock C, Apicella AJ (2015). Callosal projections drive neuronal-specific responses in the mouse auditory cortex. J Neurosci.; 35(17):6703-13.

Scholl B, Burge J, Priebe NJ (2013). Binocular integration and disparity selectivity in mouse primary visual cortex. J Neurophysiol.; 109(12):3013-24.

Schnupp JW, Carr CE (2009). On hearing with more than one ear: lessons from evolution. Nat Neurosci.; 12(6):692-7.

Taniguchi H, He M, Wu P, Kim S, Paik R, Sugino K, Kvitsiani D, Fu Y, Lu J, Lin Y, Miyoshi G, Shima Y, Fishell G, Nelson SB, Huang ZJ. A resource of Cre driver lines for genetic targeting of GABAergic neurons in cerebral cortex. Neuron; 71(6):995-1013.

Zurita H, Feyen PLC, Apicella AJ (2018). Layer 5 Callosal Parvalbumin-Expressing Neurons: A Distinct Functional Group of GABAergic Neurons. Front Cell Neurosci.;12:53.